N. d'ordre : 42143

Université Lille1 & University of Florida

Thèse en Co-tutelle

pour obtenir le grade de :

Docteur de l'Université Lille1
PhD of University of Florida

dans les spécialités

« Micro et Nanotechnologies, Acoustique et Télécommunications & Chemical engineering »

par

Ilyesse Bihi

Removal of microparticles from a surface due to interfacial and shear forces in two-phase flows

soutenue le 30 Septembre 2016 devant le jury composé de :

M.	Christophe Josserand	Université Pierre et Marie Curie	(Président)
Mme	Anke Lindner	Université Paris Diderot	(Rapporteur)
M.	Anuj Chauhan	University of Florida	(Rapporteur)
M.	Ranganatha Narayanan	University of Florida	(Examinateur)
M.	Thomas Ettor Angelini	University of Florida	(Examinateur)
Mme	Pascale Aussillous	Aix-Marseille Université	(Examinateur)
M.	Michael Baudoin	Université Lille1	(Invité)
Mme	Christine Faille	PIHM - INRA	(Invitée)
M.	Farzam Zoueshtiagh	Université Lille1	(Directeur de Thèse)
M.	Jason E Butler	University of Florida	(Directeur de Thèse)

Institut d'Electronique Microélectronique et Nanotechnologie
U.F.R de Mathématique
Université Lille1
59655 Villeneuve d'Ascq France

REMOVAL OF MICROPARTICLES FROM A SURFACE DUE TO INTERFACIAL AND SHEAR FORCES IN TWO-PHASE FLOWS

By

ILYESSE BIHI

A DISSERTATION PRESENTED TO THE GRADUATE SCHOOL
OF THE UNIVERSITY OF FLORIDA IN PARTIAL FULFILLMENT
OF THE REQUIREMENTS FOR THE DEGREE OF
DOCTOR OF PHILOSOPHY

UNIVERSITY OF FLORIDA

2016

To my parents

ACKNOWLEDGMENTS

My utmost gratitude goes to my PhD advisors, Prof. Farzam Zoueshtiagh and Prof. Jason E. Butler for giving me the opportunity to join their laboratories. They trusted me and for this I am in great debt to them. They stand among the most influential people in my life. I would like to thank them for their expertise, guidance, and most of all, for their patience.

I would like to express my deepest gratitude to my co-advisors; Dr. Michael Baudoin who taught me that the most important is to ask the good questions; bad questions are either more difficult to answer or worthless. Dr. Christine Faille for providing me the opportunity to work in her biological laboratory, without any restrictions. She allowed me to use her experimental setup and try new ideas. I cannot thank her enough for her support, guidance and especially for her patience with me while I was leaning the basics of biology.

My sincere gratitude goes to my French and American committee members: Dr. Ranga Narayanan, Dr. Anuj Chauhan, Dr. Thomas E.Angelini, Dr. Christophe Josserand, Dr. Anke Lindner and Dr. Pascale Aussillous. Their valuable suggestions and reviews improved this work tremendously.

Beyond my directors and my committe members, I first and foremost would like to thank all who teach. I am here because of an outstanding line of teachers, and the opportunities they have provided me. In particular, I want to mention Prof. Alain merlen, he was an inspiring professors.

I am very grateful to the very nice people I met in Gainesville. In particular, Phong was very helpful and as a pioneer in defending his PhD, he smoothed the path for me in terms of the administrative procedures in the UF. I am also grateful to Mert, Aycan, Tuba, Saif, Ryan and Gargie who made my stay in the US enjoyable and memorable. I further want to thank the UF French club, talking French with them made me feel at home. The UF NSF-PIRE program (0968313) supported generously my research performed in Gainesville, I owe more than a thank to this institution.

I am thankful to Stefano, Carmelo, Théo and Fabio, “Barrois Team”. I will miss the many life and research discussions spent with them. Each day was an opportunity to learn and share new things. To AIMAN team, it has been a pleasure to spend time with all of you.

My deepest gratitude goes to my parents and my two lovely sisters for their infinite support throughout everything, ‘I love you’. Lastly, I would like to thank my sweetheart, for your love and patience. You were always there to give me the positive energy I needed to overcome my uncertainties.

TABLE OF CONTENTS

LIST OF TABLES

LIST OF FIGURES

Abstract of Dissertation Presented to the Graduate School
of the University of Florida in Partial Fulfillment of the
Requirements for the Degree of Doctor of Philosophy

REMOVAL OF MICROPARTICLES FROM A SURFACE DUE TO INTERFACIAL AND SHEAR FORCES IN TWO-PHASE FLOWS

By

Ilyesse Bihi

December 2016

Chair: Jason E Butler
Major: Chemical Engineering

Food contamination due to pathogens and spoilage bacteria on surfaces of industrial equipment is a major issue that has not yet found a proper solution. Indeed, despite the set-up of cleaning and disinfection procedures, some bacteria (microparticles) are still commonly found on the surfaces of food processing lines. Traditionally, industrial cleaning procedures involve viscous stresses in a single-phase flow to remove spores from a surface. The present study investigates the use of two-phase flows for improving cleaning procedures. Such system has the advantage of involving interfacial forces that can aid in the removal of microparticles as long as certain wetting conditions are met. This would imply the detachment and collection of the microparticles by the fluid-fluid interface. This collection will in turn affect the dynamics of the interface if its surface is insufficient to accommodate all particles. With respect to viscous stresses in removing particles, a numerical code is developed to study the dynamics of ellipsoids near a solid surface in a shearing flow. The shape of the microparticles in the simulations is set to mimic the spores morphology. Finally, the study examines the effect of the initial environment on the ease of spores removal. In particular, the study investigates the drying conditions that spores undergo in an industrial environment before the cleaning procedures start.

CHAPTER 1
INTRODUCTION

Cleaning a surface is an unpleasant, difficult, and often expensive daily drudgery. Although detaching microparticles from surfaces is a necessary step in many processes, strong attachment of bacteria (e.g. Escherichia coli, Listeria, Bacillus cereus spores, and more) to the walls of the production lines is a particularly critical issue in the food industry, entailing both economic and health consequences. These micro-organisms have the capacity to attach to a large range of equipment surfaces (glass, metals, polymers, ...) and may cause food safety issues in contemporary society [1, 2]. Indeed, they have been heavily linked to food poisoning where, for instance, they accounted for around 40% in France between 1996 and 1998 [3]. Furthermore, recently the French Institute for Public Health Surveillance unveiled that 62% of food infections in collective catering would be induced by contamination of equipment surfaces [4].

Most of the researches associated to the industrial cleaning procedures investigate the capability of viscous stresses in a single-phase flows to remove spores[1] [5, 6]. Furthermore, most existing methods for effectively cleaning food-processing equipment can be lengthy in time, utilize chemicals, and expend a large amount of energy, as in the case of steam treatment. These processes can be optimized by better understanding the mechanisms behind spores attachments to walls and also by investigating the field of multiphase flows which present interesting characteristics that could facilitate spores removal.

The benefit in use of multiphase flows, and particularly two-phase flows that will be investigated here, stand in their ability to increase the shear stresses near walls and eventually add interfacial stresses that may contribute in spores/particles detachment. Indeed, depending on the wetting properties of the particle, it is possible to choose adequate fluids, so that the minimum energy state is reached when the particle is located at the interface between

[1] Resistant form of bacteria in survival conditions

the two-fluids. Thus, when droplets or bubbles come into contact with a particle/spore, it will induce capillary forces which can contribute to its detachment from the substrate. A preliminary work had been conducted in the first months of this thesis to investigate the removal of microparticles by a two-phase flow. Appendix A describes this preliminary work where an air bubble is injected inside a water-filled capillary tube inside which microparticles are deposited. The aim of the experiment was to highlight the effect of a bubble on the removal of particles. The results showed that the latter are better detached and collected from the wall by a single bubble than by a one phase flow at the same flow rate. Both capillary and hydrodynamic forces were pointed as contributors in the removal process, whereas, the nature of the adhesion forces is a combination of van der Waals and electrostatic forces, hydrogen bonding, steric interactions, capillary forces, etc. [7]. For instance, if one assumes that the adhesion is primarily caused by van der Waals forces, for a spherical particle the adhesion force $F_A = AR_p/6H^2$, where A is the Hamaker constant, R_p the particle radius and H the distance of closest separation between the particle and substrate. Note that H is small compared to R ($H \ll R$). However, in reality van der Waals force does not act alone and all the other forces are added to give the final adhesion force.

Now consider the case of particles attached to the inner walls of a capillary tube. A driving force is required to remove these particles from the wall. In the case of a two-phase flow, two possibilities can be distinguished (see Fig 1-1): (A) the air-water interface intersects the particle or (B) the air-water interface passes over it. In the first case, the detachment is aided directly by the capillary force while in the second case, it is due to hydrodynamic forces.

Capillary forces: When a moving interface[2] intersects a microparticle (case (A)), strong capillary forces act on it in the direction of the moving interface [9–11]. Note that this phenomenon occurs in nature, where water droplets rolling off of a Lotus leaf removes

[2] Henceforth in this document, interface refers to the air-water interface

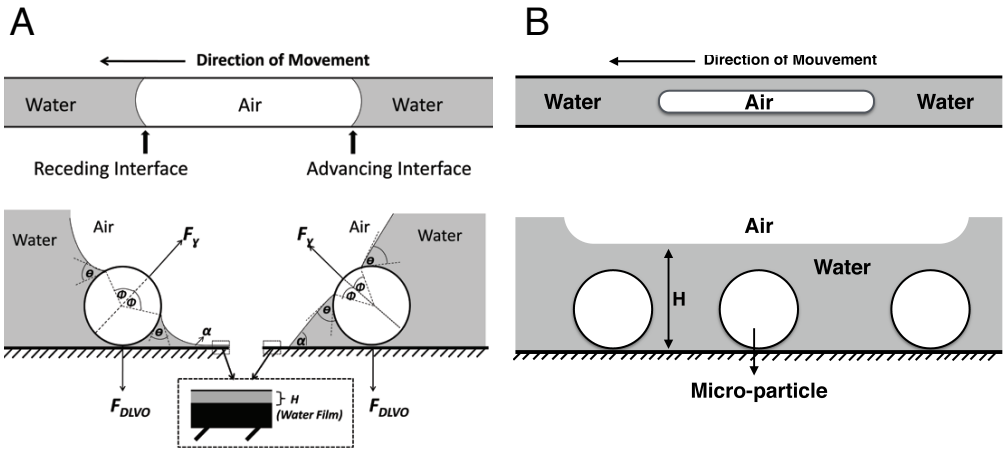

Figure 1-1. Two-phase flow: motion of a bubble through a tube in the presence of microparticles. **(A)** At very low flow rates, the surface tension force acts directly on a particle [8]. **(B)** At high flow rates, the bubble elongates at the center of the tube and the particles do not intersect the air-water interface. Thus, the forces acting to remove the particles are purely hydrodynamic.

dust particles from the surface. This self-cleaning process, due to the hydrophobicity of the lotus leaves, is called the "Lotus Effect" [12, 13]. Now consider the case of a particle located on the wall and in contact with the liquid interface. Forces acting on it are capillary, DLVO[3] , hydrodynamic, and buoyancy forces. For small microparticles (radius$< 500\mu m$), the buoyancy forces are negligible compared to the interfacial forces [14–17]. In all our study the particle size vary between $0.5\mu m$ and $40\mu m$, consequently, the interfacial forces are dominant. Additionally, for very low flow rates, the hydrodynamic forces around the particle can be neglected. The component of the interfacial force, F_γ, that acts normal to the interface can then be expressed as [8]

$$F_\gamma = 2\pi R_p \gamma \sin\Phi \sin(\theta - \Phi),$$

[3] DLVO forces: named after Derjaguin, Landau, Verwey and Overbeek. Force combining the effects of Van Der Waal's attraction and the electrostatic repulsion. Used here to indicate the force between the wall and the particle

where R_p is the radius of the particle, γ is the surface tension, Φ is the filling angle, and θ is the contact angle of the air-water interface with the particle. The adhesion forces, also called DLVO forces, depend on the balance between attractive Van der Waal's forces and repulsive electrostatic double layer forces. Some mechanistic studies showed that the interfacial force can exceed the adhesion forces with the surface [8, 18–20] leading to the detachment of the particles.

Hydrodynamic forces: In the second case (B), the air-water interface passes over the particles and does not intersect it. Therefore, the capillary force does not play a direct role on the removal of particles. Nevertheless, two potential advantages of a two-phase flow system over the single phase system can be identified. Firstly, the presence of the bubble increases the shear rate and thus, the hydrodynamic forces on the particle (note that the overall volumetric flow rate is held constant when comparing the two-phase and single phase systems). Secondly, the motion of the bubble creates flow recirculations at the leading and trailing edges. These flow patterns may also assist with lifting the particle away from the wall.

Back to the industrial environment, spores, which are usually present in aqueous solutions, may come into contact with air and undergo a drying process. Although numerous studies focused on individual effects to understand the spore adhesion on a substrate, the evolution of the adhesion forces in a drying process has not been reported yet. Such a study is nevertheless fundamental since it can allow the determination of the optimal conditions for cleaning procedures.

In this thesis, we aim to answer several fundamental questions that may arise in removal and transport process of particles from a surface. While the ultimate goal is the optimization of cleaning procedures in food-related industries, the present study make use of drastic simplifications such as the use of solid particles instead of microorganisms in the first two chapters, in order to develop a theory that can explain the experimental results. The study can then be presented as primarily steps that will pave the way of our ultimate goal.

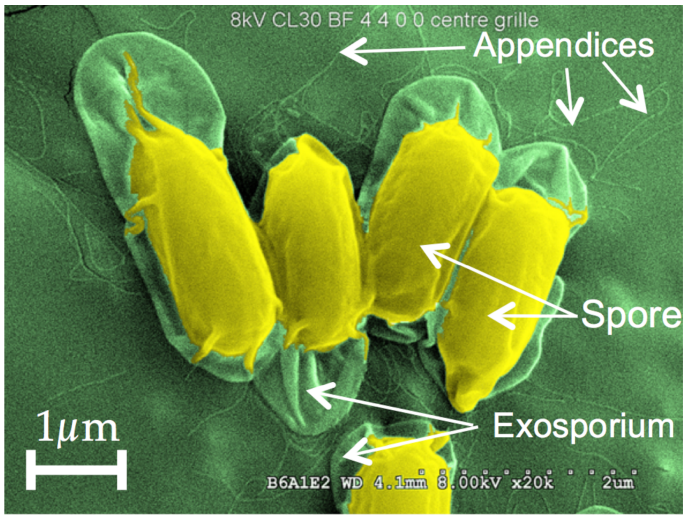

Figure 1-2. SEM (Scanning Electron Microscopy) picture of Bacillus cereus 98/4 highlighting its complex shape

The first Chapter focuses on an interface between two Newtonian fluids, where the flow is restricted to low Reynolds and capillary numbers. Also, note that the micro-organisms encountered in the food industry, such as bacteria or spores, may be extremely complex in shape and dynamics (Fig. 1-2). They are living organisms having a variety of forms and morphologies, able to reproduce and replicate quickly. Therefore, in order to separate the biological issues from the physical ones, the present work mainly focuses on solid micro-particles. The detachment of the particles from surfaces by a passing fluid-fluid interface is experimentally studied. Furthermore, in the case of particle collection by the interface, the dynamics and the stability of the latter is investigated.

The second chapter investigates numerically the trajectory of suspended particles near a wall whose ellipsoid shapes mimic spores that are commonly found in food production lines. The study aims to unveil the under which circumstances of particle's lift from a solid surface after its detachment. For this reason, we will calculate the evolution of a microparticle near the wall for a simple shearing flow. We will use the boundary integral method; this nifty method solves a Stokes flow solely by reference to what happens at the flow boundaries,

hence requiring discretization only of the surface of the particle, rather than the entire flow domain.

Finally, Chapter 4 investigates the detachment of micro-particles and spores subjected to different initial attachment conditions. Indeed, in the food industry the spores can regularly be subjected to drying conditions, and the initial environment seems to be a key factor in attachment forces. Therefore, experiments were carried out to remove different types of spores from surfaces by changing the drying conditions. The results are compared to those obtained with microspheres with the aim to dissociate the biological effects from the physical effects.

The diagram of figure. 1-3 attempts to place the different parts of the present study in the environment that spores can encounter in a simplified food production lines.

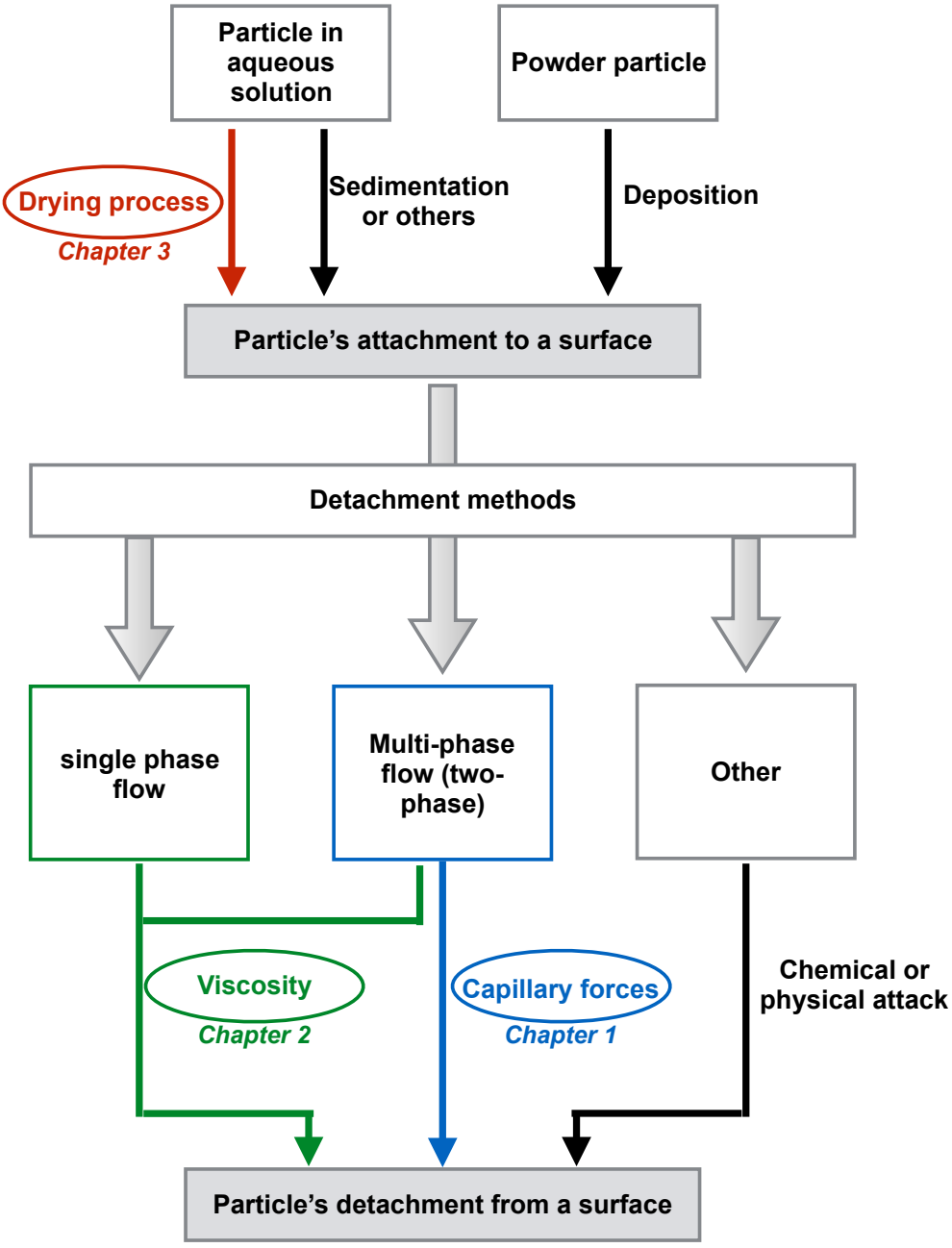

Figure 1-3. Simplified diagram of the microparticles' attachment and detachment. Depending on the initial particle's environment, the attachment processes to the surface are different. Different methods can be used to remove the particles from the wall. The colors show the aspects that will be treated in this thesis. The first chapter in blue, green for the second chapter and red for the third chapter.

CHAPTER 2
REMOVAL OF MICROPARTICLES BY LIQUID INTERFACES LEAD TO INSTABILITIES.

2.1 Prior Work

In this chapter[1] the dynamics of a fluid-fluid interface with particles is investigated. This study follows the work of Zoueshtiagh *et al.*[11] who studied the particle collection in the confined geometry (1D) of a capillary tube. The present work extends their study for the case of a 2D Hele-Shaw configuration.

The dynamics of a liquid interface pushing air where particles are covering the walls is studied. Zoueshtiagh *et al.* showed in their study that the particle collection is a results of the minimization of the total energy, E, of the system. The latter is the sum of the gas-liquid (GL), gas-wall (GW), liquid-wall (LW), gas-particle (GP) and liquid-particle (LP) energy:

$$E = \gamma_{GL}A_{GL} + \gamma_{GW}A_{GW} + \gamma_{LW}A_{LW} + \gamma_{GP}A_{GP} + \gamma_{LP}A_{LP} \tag{2–1}$$

where γ is the surface tension, and A the area corresponding to the interface. According to wall and particle wetting properties, three main regimes could be distinguished in the capillary tube: (i) for perfectly wettable particles, the motion of the meniscus was weakly affected with the particles going directly into the liquid phase. (ii) For partially wettable particles with wettable walls, the particles were collected in a monolayer pack at the liquid interface. This eventually would lead to the formation of armored bubbles (see Fig. 2-1). Finally (iii) for partially wettable particles with hydrophobic walls the particles were accumulated along the contact line and could result in the formation of armored air pockets on the wall (see Fig. 2-2).

[1] Reprinted with permission from I.Bihi, M. Baudoin, J.E. Butler, C. Faille, and F. Zoueshtiagh, Inverse Saffman-Taylor Experiments with Particles Lead to Capillarity Driven Fingering Instabilities, Phys. Rev. Lett. **117**, 034501 (Jul 2016)

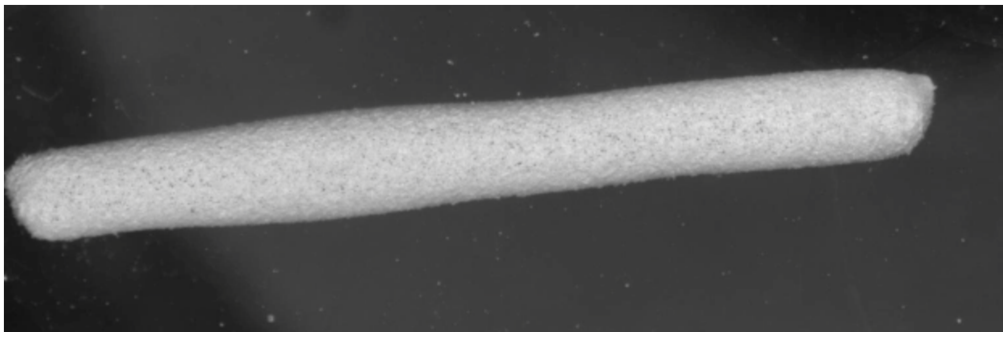

Figure 2-1. Cylindrical armored bubble covered with a monolayer of polyamide particle surrounded by water. The bubble was created as described by Zoueshtiagh *et al* [11]

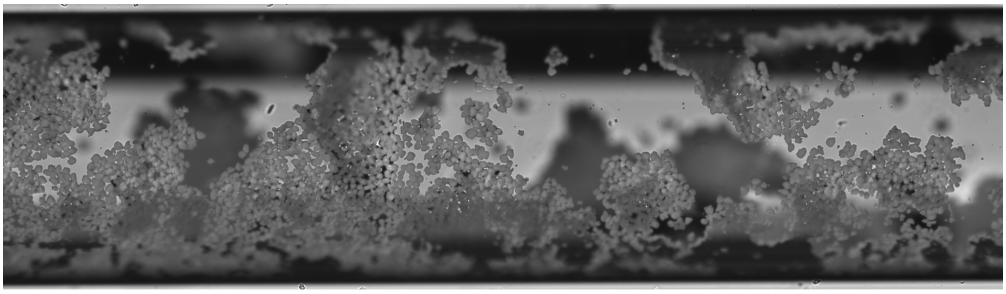

Figure 2-2. Snapshot showing the airpocket in a capillary tube obtained by Zoueshtiagh *et al* [11].

In the present study, in order to remove the microparticles from the wall and collect them at the interface only the conditions of regime (ii) were experimented. In particular the dynamics and the stability of the interface were investigated. The stability of a liquid interface is of particular interest since the efficiency of a cleaning procedure which involves interfacial forces would depend on the ability of the interface to collect and transport the dirt. It is known that when a less viscous fluid displaces a more viscous fluid in a Hele-Shaw cell, fingering patterns at the interface between the fluids, commonly known as Saffman-Taylor instability, arise (see Fig. 2-3). On the opposite, the displacement of less by a more viscous fluid is generally admitted as stable and is investigated here in the presence of particles. The emergence of eventual fingering is sought as it would directly affect any cleaning efficiency.

Figure 2-3. Fingering pattern of a fluid displacing an another of higher viscosity ($\eta_{in}/\eta_{out} = 3.10 \times 10^{-2}$).[22].

2.2 Background

The Saffman-Taylor instability [23–25] is a classical, interfacial instability that occurs when a low viscosity fluid displaces one of higher viscosity in a Hele-Shaw cell [26]. The instability generates a fingering phenomenon at the moving interface that leads to complex tree patterns. Aside from the beauty of the structures, the attention devoted to this instability can be attributed to its widespread relevance in applications such as flows in porous media [27–29], flame propagation [30, 31], and growth of bacterial colonies [32]. The instability results from the decrease of the flow resistance as the fluid of lower viscosity replaces the more viscous fluid; the inverse situation, wherein a highly viscous fluid is pushed into a cell filled with a weakly viscous fluid, is stable. Despite the large number of investigations of interfacial instabilities, the displacement of air by a viscous fluid in the presence of particles has not been reported in the literature. Nevertheless, this case is of importance in cleaning processes when bacteria, spores, dust or particles are present on surfaces.

Here, we demonstrate the formation of fingering patterns emerging from the injection of a liquid into a cell filled with air in the presence of microparticles on the walls. This corresponds to the reverse situation compared to the common Saffman-Taylor instability. This instability relies on the integration of partially wettable particles to the meniscus driven by the minimization of interfacial energy. A reverse Saffman-Taylor instability in the presence of surfactants has been previously reported in the literature by Chan *et al.* [33] and then by Fernandez *et al.* [34], but, in contrast to these studies, the fingers observed in our studies with particles are not limited in depth.

Air-water interfaces can induce strong capillary forces able to remove microparticles initially deposited on a wall surface. In nature, this phenomenon happens frequently when a raindrop falls on a lotus leaf. Due to the hydrophobicity of the surface and gravity, the water drop rolls off of the slanted leaf while also removing dust particles. This self-cleaning process is referred to as the "Lotus-Effect" [12, 13, 35] and is of primary interest to a wide variety of industrial processes including tube [8, 11] or microelectronic silicon wafer cleaning [18], separation of minerals in the mining industry [36], particle flotation [9], or even stabilization of bubbly liquids, foams and emulsions [37–41]. Once the microparticles are removed from the surfaces, they are adsorbed and transported by the air-water interface. We show here how the presence of these particles can dramatically affect the stability of an interface.

2.3 Experiments

2.3.1 Radial Hele-Shaw Cell

This "particle-driven" fingering instability is first studied in a radial Hele-Shaw cell (see Fig.2-4) which is constructed of two circular glass plates of radius 50 mm. They are centered and placed on top of each other at a separation distance of H, that was varied between 0.1 and 1 mm. The plates were cleaned prior to each experiment with isopropanol alcohol, distilled water and acetone. Then, Rilsan (Polyamide 11) particles with an average radius of 15 μm were sprinkled onto both glass surfaces to give a concentration C, as measured from microscopy images of the particle-covered plates. This concentration C corresponds

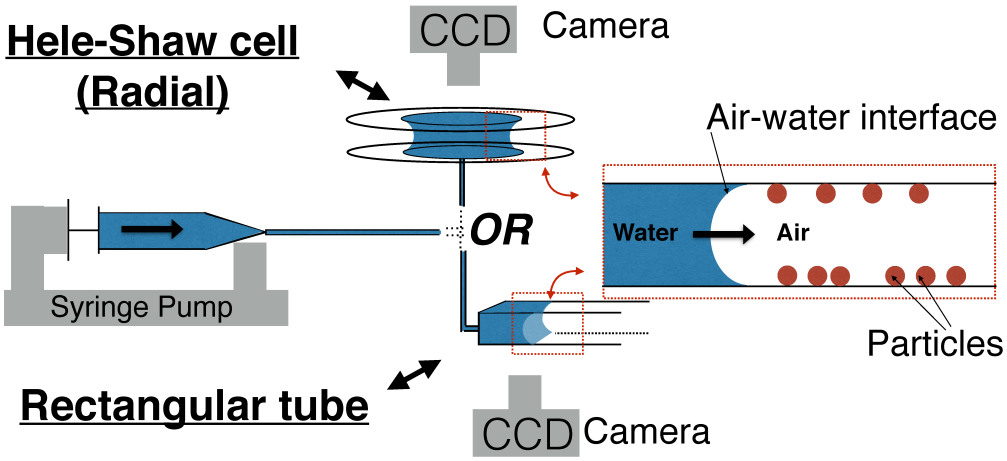

Figure 2-4. Schematic of the experimental setup: water is injected into air using a syringe pump either between two parallel plates (radial Hele-Shaw cell) or inside a rectangular tube. Microparticles were deposited on the surfaces prior to water injection.

to the ratio of the surface covered by the particles to the total surface. The uniformity of C was evaluated and is reported with each result. The particles have a density of 1.03 g/cm^3 and are hydrophilic ($S_p < 0, \theta_p = 71° \pm 3°$, with S_p the spreading parameter and θ_p the static contact angle between the particles and deionized water [11]). Water is injected into this cell through a hole drilled at the center of the bottom plate at constant flow rates Q (2, 20, 200 or 2000 mL/h) and the evolution of the liquid-air interface was recorded with a CCD camera. For the experiments described above, the capillary number, Reynolds number, and Bond number are defined, respectively, as $Ca = \mu_l U/\gamma_{GL}$, $Re = \rho_l UH/\mu_l$ and $Bo = \rho_l gH^2/\gamma_{GL}$, where ρ_l, μ_l and γ_{GL} are the density, viscosity and surface tension of the DI water. Gravitational acceleration is g and the values of Bo range from approximately 10^{-3} to 10^{-1} depending on the plate separation. Both Ca and Re depend upon the velocity of the interface $U = Q/(2\pi rH)$, which is a function of the radius r. At the inlet where $r = 2$ mm, the maximum values are $Ca \approx 10^{-3}$ and $Re \approx 10^2$ and, at the outlet ($r = 40$ mm), the minimum values are $Ca \approx 10^{-6}$ and $Re \approx 10^{-4}$.

As fluid is injected between the plates, the air-water interface starts to expand radially. Microparticles encountered by the moving interface are captured and progressively cover the

meniscus. When a critical radius r_c is reached, destabilization of the interface occurs and the formation of fingering patterns begins [see Fig. 2-5]. To better understand this phenomenon, the critical radius was measured for different particle concentrations C, gap widths H and flow rates (quantified by the capillary number Ca at the critical radius r_c); the data are shown in Fig. 2-6.

In the present case, the interface instability seems to occur once the meniscus is entirely covered with particles. To verify this hypothesis, we estimated theoretically the critical radius at which this happens from a simple balance of the surface occupied by the particles once they are collected by the meniscus and the space available on the meniscus as it expands radially (see APPENDIX B for the detailed calculation). For wall contact angles α_E lying between 0 and $\pi/2$, the critical radius is predicted to be between

$$\underbrace{\frac{r_c}{H} = \frac{\phi\pi + \sqrt{\phi^2\pi^2 - 8C\phi}}{4C}}_{\text{for } \alpha_E=0} \quad \text{and} \quad \underbrace{\frac{r_c}{H} = \frac{\phi}{C}}_{\text{for } \alpha_E=\pi/2}.$$

The measured value of the contact angle at the wall is $10° \pm 4°$ in the absence of the particles, but contaminants introduced with the particles may alter this value. In this formula, ϕ is the specific surface area of the particles on the interface, that is to say the fraction of the surface that the particles occupy on the meniscus due to their shape and arrangement, in close packing configuration, once the meniscus is entirely covered with particles. There is no reason for the particles to be organized in a specific way; thus, ϕ is equated with random packing of spheres on a flat surface: $\phi \simeq 0.8$ [42, 43]. This value may slightly fluctuate depending on the exact shape and organization of the particles. Since we cannot visualize the particles' organization on the meniscus, the critical radius is estimated for values of the specific surface area lying between 0.7 and 0.8. Figure 2-6 shows that the calculation of r_c closely matches the experimental results at low capillary numbers ($Ca < 10^{-4}$), when interfacial phenomena largely dominate the dynamical phenomena, supporting the hypothesis. Indeed, it is well known [9–11] that hydrophilic particles are naturally collected by a liquid-air interface to minimize the interfacial energy. However, once the expanding interface becomes entirely

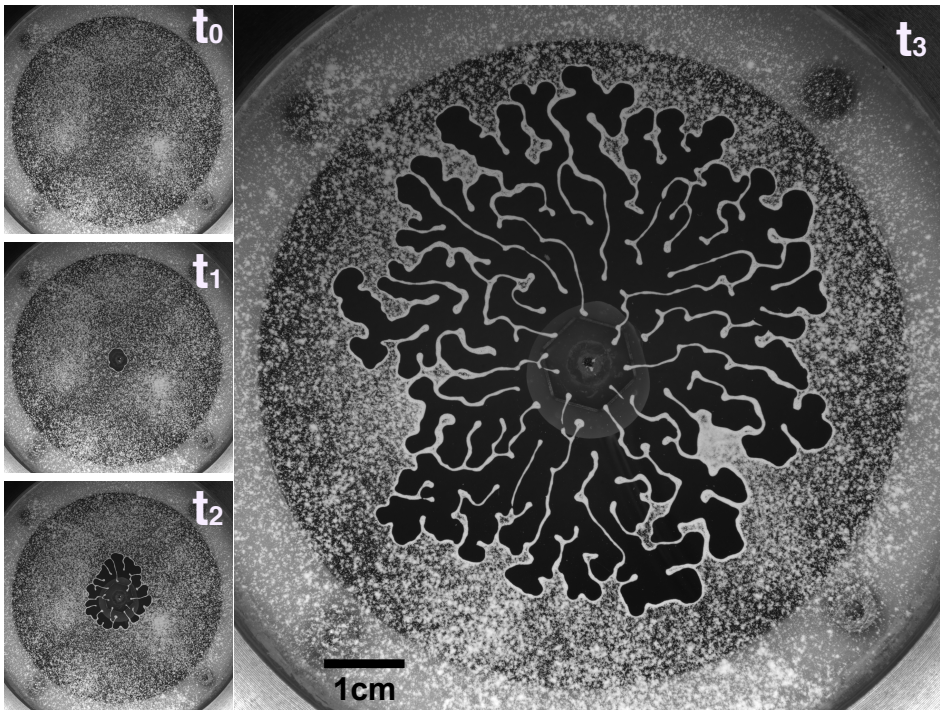

A

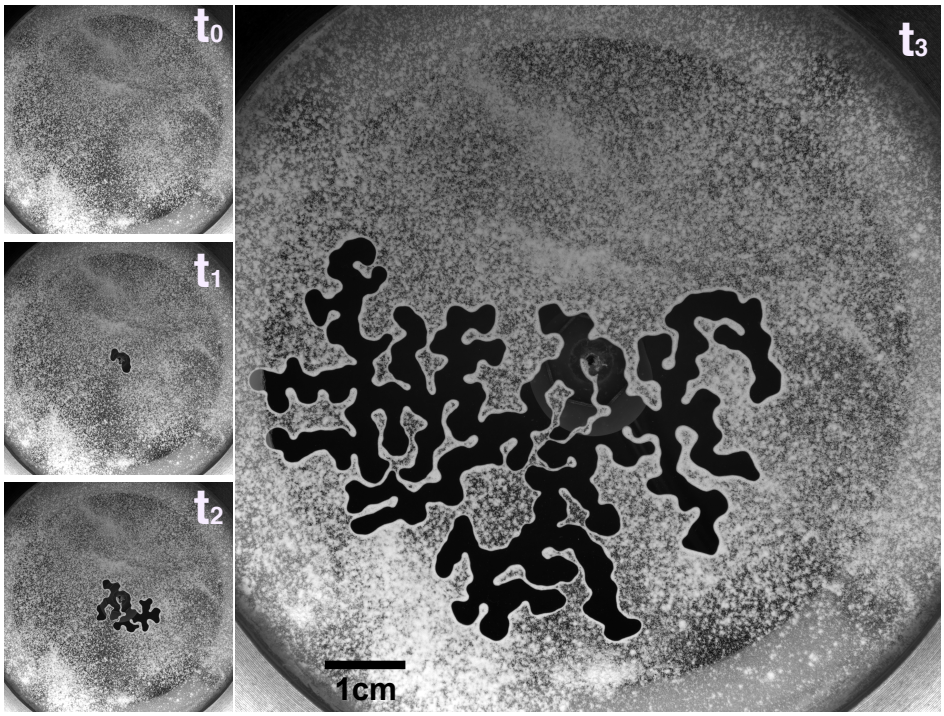

B

Figure 2-5. Images showing a time sequence of the interfacial instability in a radial Hele-Shaw cell. **(A)** Plate spacing of 150 μm, $C = 0.78$, flow rate $Q = 200\ mL/h$ ($Ca \approx 10^{-4}$). **(B)** Plate spacing of 150 μm, $C = 0.69$, flow rate $Q = 20\ mL/h$ ($Ca \approx 10^{-5}$). $[t_0, t_1, t_2, t_3 = 0, 1, 5, 30s]$.

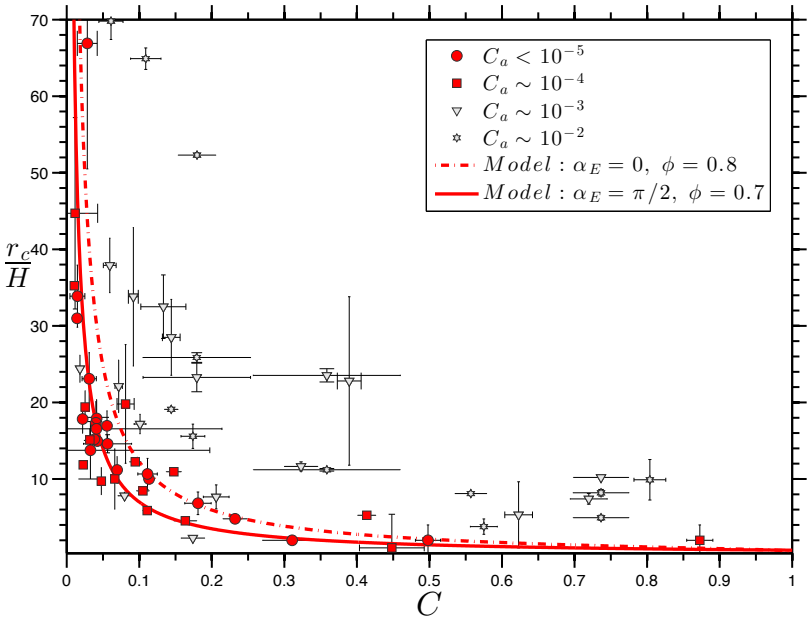

A

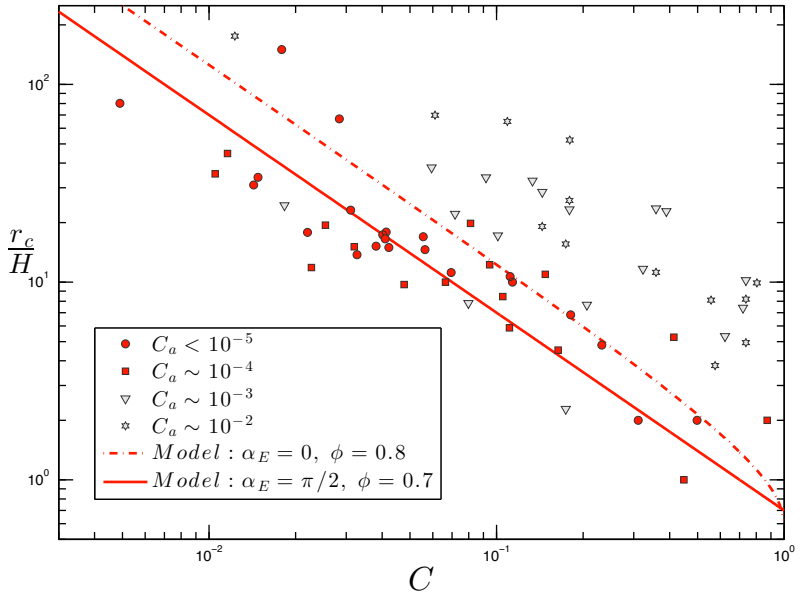

B

Figure 2-6. The critical radius at which the instabilities start in the radial Hele-Shaw cell. The horizontal error bars represent the concentration standard deviation with a confidence level of 96%. The vertical error bars represent the minimum and the maximum of the critical radius.

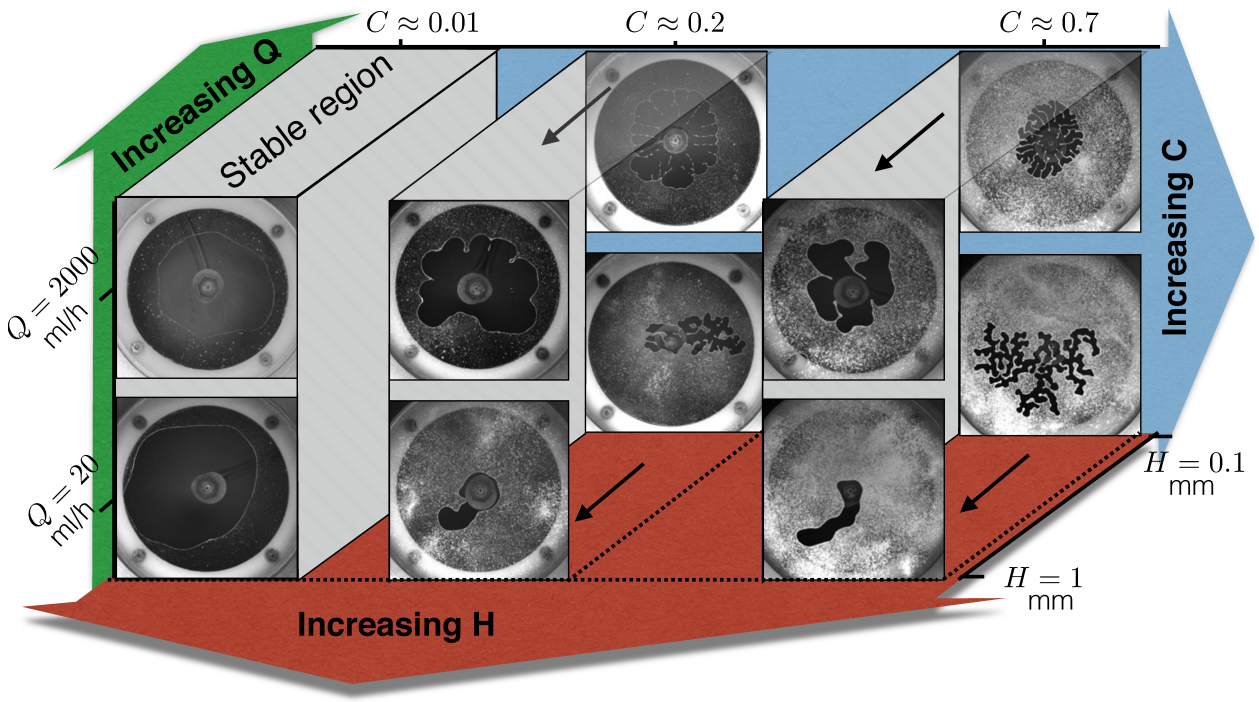

Figure 2-7. Diagram of the different instability patterns as a function of the concentration of the particles C, the flow rate Q and the gap between the plates H.

covered by particles, integrating additional particles into the interface is not possible while also maintaining a purely radial growth. Instead, either the liquid-air interface will start expanding in a different way to incorporate new particles or the particles will remain in the gas or enter the liquid phase. The former case is always observed in the present experiments.

For concentrations $C \leq 0.8$, the integration of particles is achieved through the development of a fingering pattern that increases the interface to volume ratio as compared to the radial configuration. At very high particle concentrations ($C \geq 0.85$), the integration of particles is generally achieved through the deposition of a liquid film ahead of the meniscus (see Figure 2-8). This liquid film creation was first observed by [11] in a cylindrical tube and gave rise to so called armored bubbles. For high capillary numbers, departure from our prediction is indicative of the role played by the fluid flow in the formation of the fingering patterns. Indeed, our model assumes that the evolution of the fingers is a quasi static process solely driven by interfacial phenomena, which is no longer valid at higher capillary numbers.

We further investigated the structure of the patterns (finger widths and numbers, symmetry) as a function of the experimental parameters C, H and Q (see Fig. 2-7). The width and number of fingers mainly depend on the plate separation distance H and the particle concentration C, while the symmetry of the patterns is mainly determined by the flow rate Q. At low capillary number, some labyrinth patterns similar to those produced by the drainage of a granular-fluid system in two dimensional confinement [27] are formed. Indeed, the finger growth is solely driven by the particle collection. As long as the particles are uniformly distributed, no preferential direction of finger growth is observed. At higher capillary number, the finger growth is essentially radial, similar to the viscous fingers produced by Saffman-Taylor instabilities, due to the increasing importance of radial viscous flow stresses.

2.3.2 Rectangular Tube

The patterns formed in this radial Hele-Shaw configuration are relatively complex (see Fig. 2-7). There is an interplay between the number of fingers and their width and the fingers' progress intermittently and at varying rates. To simplify this problem, we investigated the relation between the finger width L_D produced by this instability as a function of the particle concentration in a simpler geometry (rectangular borosilicate capillary tube of height $H = 0.40$ mm and width $W = 10H$), where the finger width is expected to be relatively constant. The inner walls were first degreased by sonication while suspended in acetone, then isopropanol, and finally in dichloromethane for five minutes each. Next, the tubes were dried under nitrogen flow and submerged in a freshly prepared piranha solution (sulfuric acid H_2SO_4 + hydrogen peroxide H_20_2) at 100°C for one hour. The channels were rinsed thoroughly with deionized water and dried in an oven at 120°C for one hour. Then, the inner walls were covered by Rilsan (Polyamide11) particles by gently blowing them into the channel with an air jet. Water was injected through the tube at a constant flow rate $Q = 0.1$ mL/h, corresponding to a capillary number $Ca = \mu_l Q/(\gamma_{GL} W H) = 2.38 \times 10^{-7}$, while recording the dynamics of the moving meniscus as described previously.

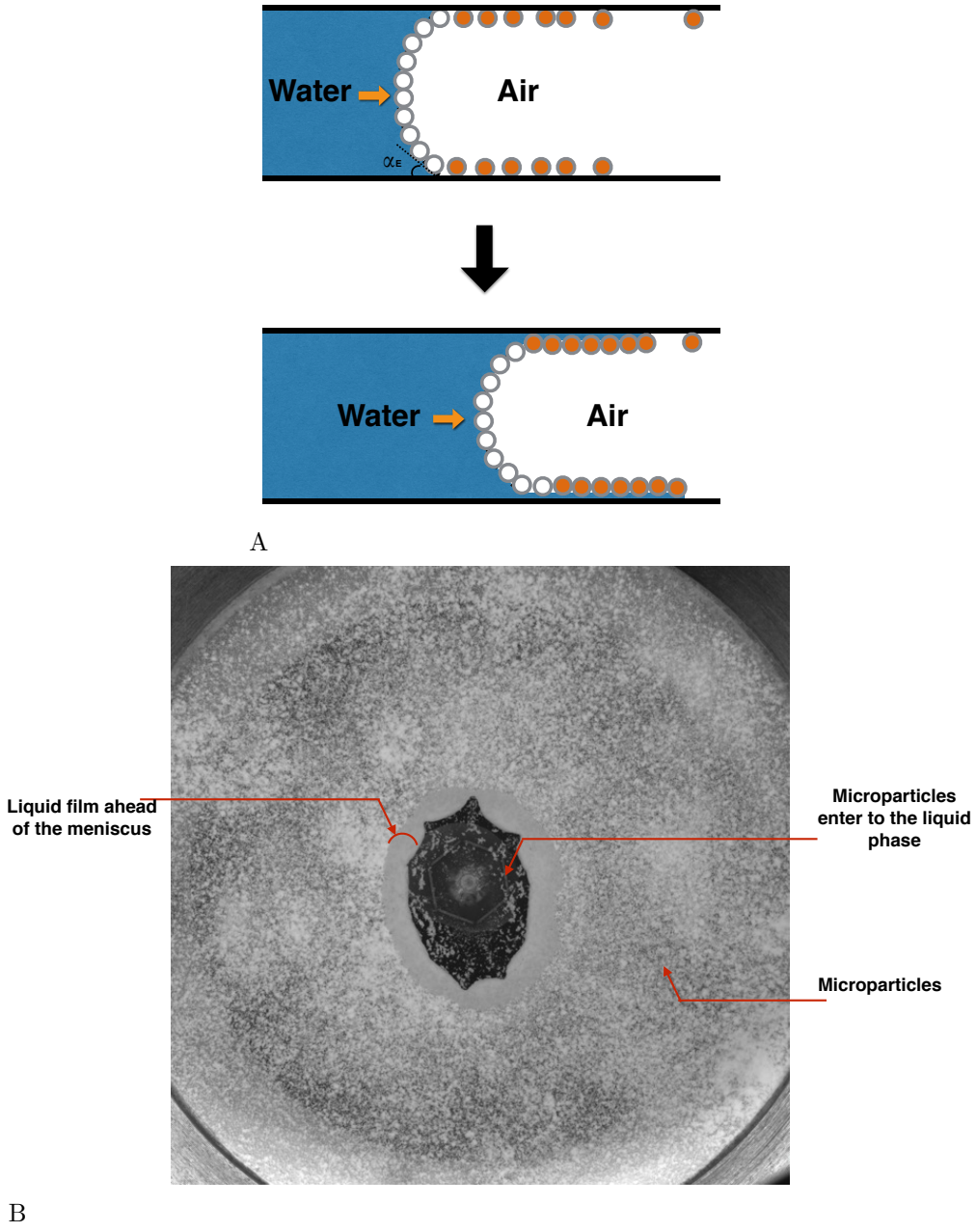

Figure 2-8. Creation of a liquid film ahead of the meniscus. **A** Sketch of liquid film creation. **B** Image of a liquid film.

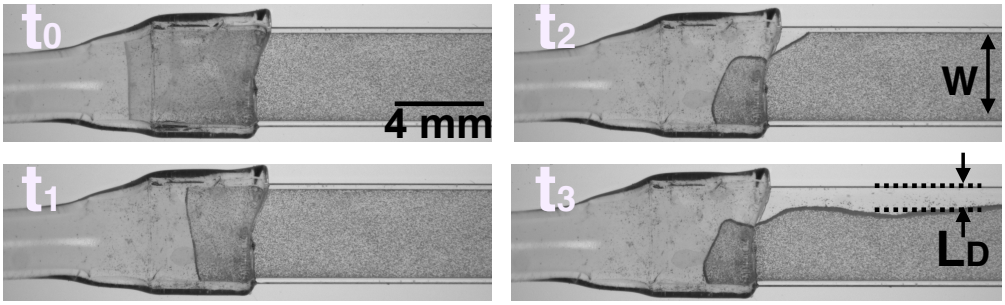

Figure 2-9. A time sequence of images showing the interface instability in a rectangular capillary tube with a particle concentration of $C = 0.3$ and capillary number $Ca = 2.38 \times 10^{-7}$. The air appears dark gray and the water is light gray.

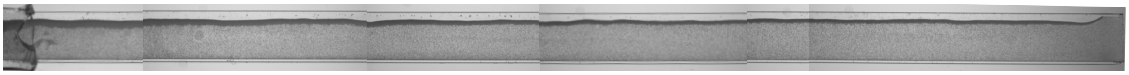

Figure 2-10. A finger creation in a rectangular tube. The air appears dark gray and the water is light gray.

As water is injected into the tube, particles initially are collected by the meniscus at the relatively short times of t_o and t_1 as seen in Fig. 2-9. For longer times t_2 and t_3, an instability occurs and leads to the formation of a liquid finger as also observed in the radial Hele-Shaw geometry. Unlike the latter geometry however, the fingers of water in the rectangular channel retain a uniform width L_D at each concentration C. The measurements of L_D, as given in Fig. 2-11, indicate an inverse relationship with the concentration C. It is interesting to note that when the finger width L_D exceeds the width W ($L_D/H \geqslant 10$), the meniscus touches the opposite wall and semi-armored bubbles, attached to the walls, are formed periodically as seen in Fig. 2-12

As before, we suppose that the interface becomes unstable once covered by the particles and that the subsequent formation of fingers is driven by interfacial energy considerations. A theoretical liquid finger width, which corresponds to the limit size allowing all particles encountered by the meniscus to be captured, can be derived (see APPENDIX B): $L_D = \phi\pi H/4C - H/2$ for a liquid-air-wall contact angle of $\alpha_E = 0$ and $L_D = \phi H/2C - H/2$ for a liquid-air-wall contact angle of $\alpha_E = \pi/2$. Comparisons of the measurements with the predictions for L_D are shown in Fig. 2-11 as a function of the particle concentration C for

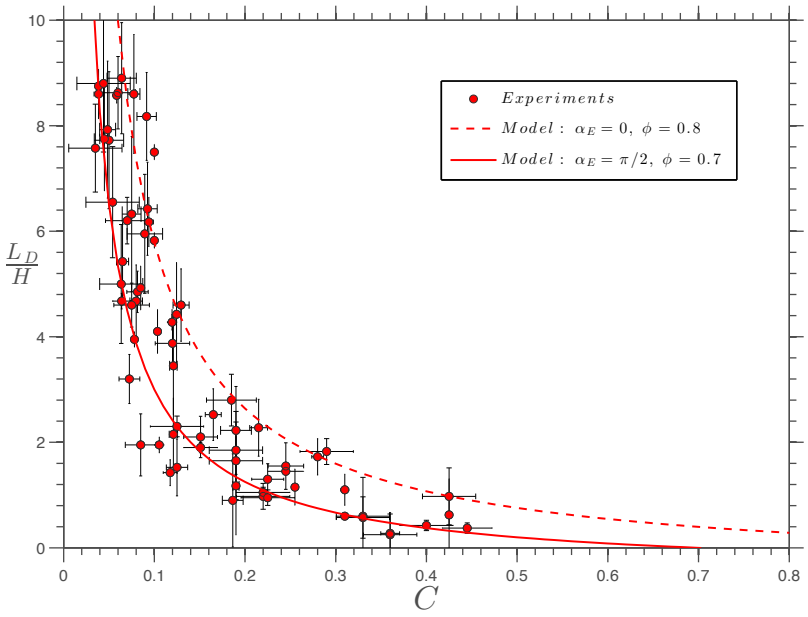

A

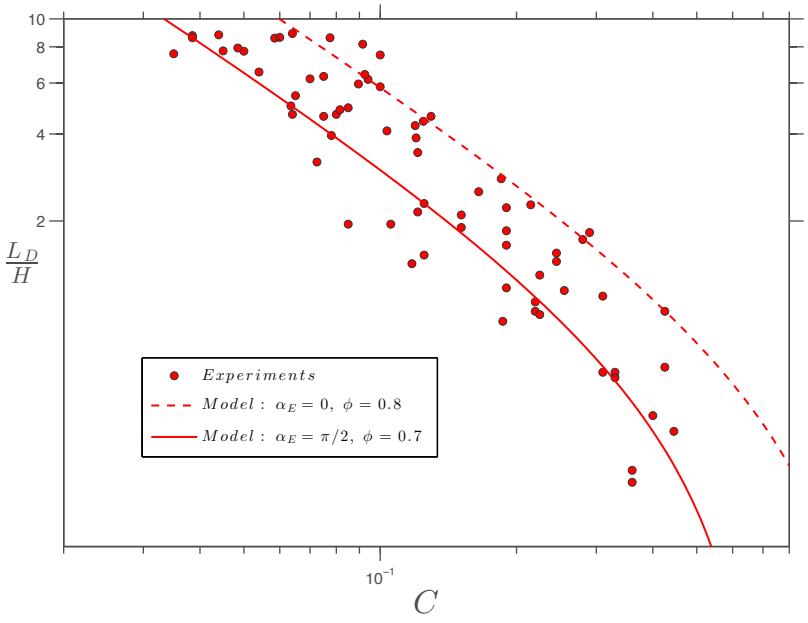

B

Figure 2-11. Measured and predicted finger width as a function of the concentration of the particles in the rectangular tube. The horizontal error bars represent the standard deviation for the concentration with a confidence level of 96%. The vertical error bars represent the minimum and the maximum of the finger width.

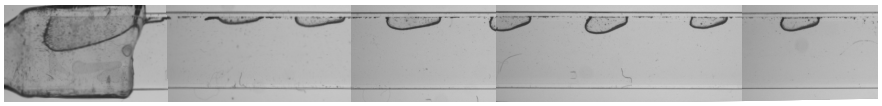

Figure 2-12. Semi-armored bubbles form when the finger width exceeds the width of the channel: $L_D/W > 1$.

different model parameters α_E and ϕ, as these two parameters likely vary depending on the cleanliness of the surface and the distribution of the particles on the meniscus. The model captures the qualitative trends of the experimental data and the data are accurately bounded by the predictions of the limiting case of $\alpha_E = 0$ with $\phi = 0.8$, providing support for the idea that the finger width is simply fixed by an interfacial energy minimization process at low capillary numbers.

2.4 Summary

To conclude, we have demonstrated that the presence of partially wettable particles on the walls can dramatically affect the dynamics of a liquid that is injected into a Hele-Shaw cell filled with air. Generally, a fingering pattern forms, even though the displacement of air with a viscous fluid is typically stable, unlike the classical Saffman-Taylor instability. The destabilization of the interface occurs due to interfacial energy minimization, which requires that all particles intersected by the meniscus are collected. As a consequence, the critical radius at which the instability occurs and the width of the fingers can be calculated by simply balancing the space available on the meniscus with the area needed to accommodate additional particles encountered by the liquid-air interface during its motion.

CHAPTER 3
MOTION OF A FREELY SUSPENDED SPHEROIDAL PARTICLE NEAR A WALL

3.1 Background

The near-wall motion of particles suspended in viscous fluid has important biological and engineering applications. The increasing interest in this problem can be linked to the diverse natural and industrial applications where particulate flows are encountered [44]. Examples include micro-vascular fluid mechanics (e.g. dynamics of a red blood cells in a vein) and suspension rheology as it pertains to the design and testing of suspension products, such as personal care items (e.g. cosmetics, toothpaste) and construction materials like paint and wall-boards. Efficient control of the flow of particles is critical to natural resource development, both in mining and petroleum exploration, and, in the food industry, the removal and transport of bacteria in the tubes of production lines is a problem of importance for public health, which is the focus of this dissertation.

In this chapter, the flow dynamics of rigid spheroids in the presence of a bounding wall are computed as a first step in the solution of more complex problems such as the removal of particles from surfaces using interfacial phenomena. The conditions of interest include both prolate (ellipsoidal) and oblate (platelet) spheroids[1] suspended at low concentrations in viscous, non-inertial flows. Compared to the flow of spherical particles under these same conditions, spheroids exhibit a much larger range of motions. For example, spherical particles do not migrate across streamlines when suspended in a flowing fluid unless they are acted upon by an external force, even if near a bounding wall. If far from any bounding walls, spheroids also remain on their original streamlines, but the orientation of a spheroid can couple to the flows to give instantaneous motions that are transverse to bounding walls as shown in Fig. 3-1. Yang and Leal [45] identified such a motion in 1984 for rods of high aspect

[1] In all cases, the spheroids under study are axisymmetric. Those shapes with one axis longer than the other two are prolate and those with one axis shorter than the other two are oblate; particles with three equivalent axes are referred to distinctly as spheres.

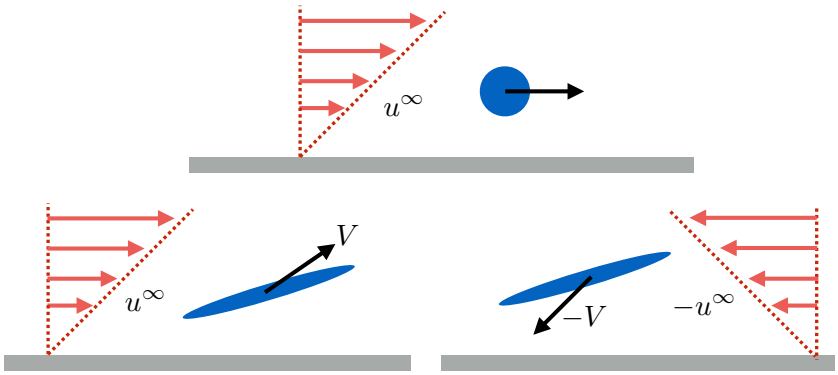

Figure 3-1. The motion of spheroids in a shear flow near to a bounding wall. In the limit of zero Reynolds number, a sphere in a shearing flow near a bounding wall (top) will not migrate across streamlines. However, a rod under similar conditions can migrate across streamlines with a velocity that depends upon its instantaneous orientation. The motion is reversible, as shown, and no motion transverse to the streamlines exists if the particles are far from the bounding wall, regardless of whether the particle is spherical, oblate, or prolate.

ratio; later, Hsu and Ganatos [46] showed that an oblate, as well as prolate, spheroids can move transverse to the wall with a velocity that depends upon the orientations.

Likewise, consider the differences in the qualitative motion of particles of different shape that are sedimenting between vertical bounding walls as illustrated in Fig. 3-2. A spherical particle translates only in the direction of gravity, though the presence of the walls slows the sedimentation velocity and also causes the sphere to rotate with a rate that depends on its lateral position. Just as with the sphere, the presence of the walls rotate the spheroid, but a non-zero component of velocity perpendicular to gravity exists for the spheroids depending upon their instantaneous alignment. Consequently, a spheroid drifts between the bounding walls as it sediments through a viscous fluid [47].

Many efforts [46, 48, 49] to calculate the detailed motion of spheroids near boundaries have done so for a limited number and range of aspect ratios, and the majority of results have restricted the particle motion to lie in the flow-gradient plane. As one exception to the range of aspect ratios, Gavze and Shapiro [50] simulated prolate particles with aspect ratios up to ten and found that the walls alter the mobility and transverse velocities most strongly for aspect ratios of approximately two. The shearing flow of an ellipsoid in a Newtonian

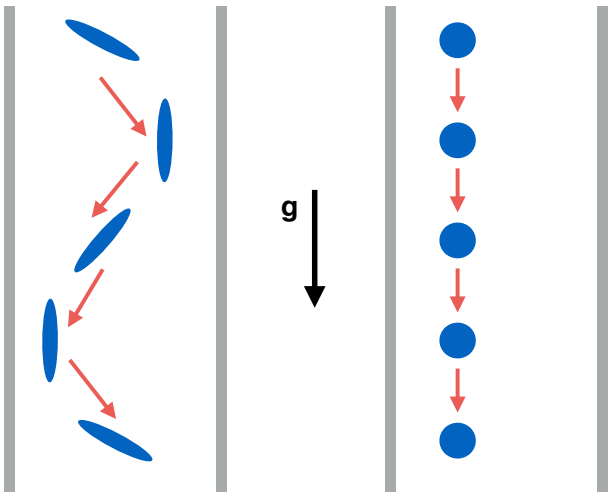

Figure 3-2. Sedimentation of a particle between bounding walls. Interactions between the walls and the sedimenting particle cause the particles to rotate, unlike the case in an unbounded fluid. For the rod, the rotation couples with the drift motion to generate the side-to-side motion shown on the left. For the spherical particle, the rotation is not coupled with the center-of-mass motion and the particle falls straight through the channel.

fluid should be reversible, as illustrated in Fig. 3-1, in the absence of external forces, torques and inertia (of both the particle and fluid). In this regard, many of the simulations exhibit convergence issues. As one example, Ingber and Mondy [48] were unable to resolve the reversible motion and, as a result, predicted a net migration of an ellipsoid away from a bounding wall.

Many studies of shearing flows of spheroids have relaxed the force-free and non-inertial restrictions. With either inertial corrections [51] or the addition of Brownian fluctuations [52–54], an ellipsoid will migrate away from the bounding walls. For shearing flows where the minimum separation distance between the particle and wall vanishes [55, 56], resolving the lubrication interactions between the translating spheroid and the bounding wall becomes increasingly expensive. Hence a repulsive force is added to prevent the overlap of the particle with the bounding wall. The resulting motion, described as a "pole-vault" because of its similarity to the track-and-field event, is irreversible due to the force and gives a slightly depleted concentration of particles near the walls. Such depletion layers have been observed experimentally [57].

Though a seemingly simple problem, owing to the linearity of the governing Stokes equations, the accurate and full range of motions of spheroids near bounding walls remains unresolved. Here, the dynamics are calculated for the shearing motions of a spheroid in the vicinity of an infinite planar wall in the limit of zero Reynolds number and in the absence of Brownian motion or other forces. The results provide a more complete picture of the dynamics over a wider range of aspect ratios, spanning oblate as well as prolate spheroids. Also, the results are compared to an improved theory for the limiting values of the aspect ratio.

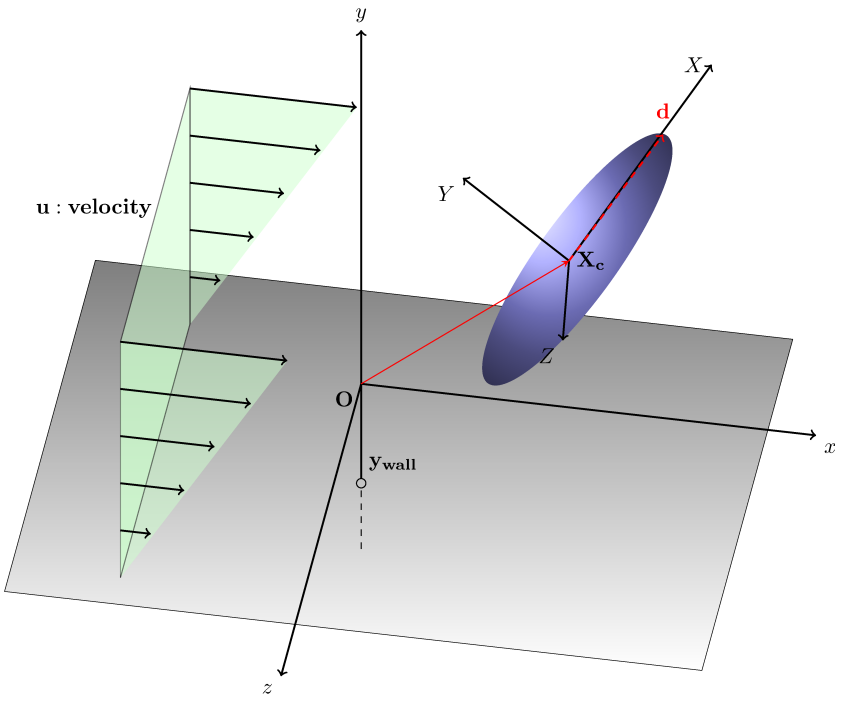

Figure 3-3. Sketch of an ellipsoidal particle in a shear flow near a planar boundary. The direction of flow is x, the direction transverse to the wall (y) corresponds to the gradient direction of the shearing flow, and z points in the vorticity direction. The vector $\boldsymbol{X}_c$ indicates the center-of-mass of the particle relative to the global coordinate system $\boldsymbol{x}$ and $\boldsymbol{X} = (X, Y, Z)$ is a coordinate system with origin at $\boldsymbol{X}_c$, but which is aligned with the global coordinate system as shown. The orientation of the ellipsoid is given by $\mathbf{d}$.

3.2 Simulation Methods

The motion of a rigid spheroid near an infinite plane wall is calculated using a boundary element method. As illustrated in Fig. 3-3, the motion is due to an imposed shear flow. In

all cases studied here the particles are large enough for colloidal forces to be negligible, so there is no need to consider Brownian motion. Additionally, no external forces are imposed on the particle.

The particle is suspended in a viscous, Newtonian fluid and the rate of shear is assumed to be small, so that inertial forces on the particle and the fluid are negligible. Consequently, the velocity field $\mathbf{u}(\mathbf{x})$ of the fluid is governed by the Stokes equations

$$\begin{aligned} \mu\nabla^2\mathbf{u} - \nabla P = 0 \\ \nabla \cdot \mathbf{u} = 0, \end{aligned} \tag{3–1}$$

where μ is the viscosity of the fluid, P is the pressure, and $\mathbf{x} = (x, y, z)$ is the coordinate system. In this limit of the Navier-Stokes equations, the non-linear term $\rho(\mathbf{u} \cdot \nabla)\mathbf{u}$ vanishes. Likewise, the unsteady term $\partial\mathbf{u}/\partial t$ can be neglected since momentum is assumed to diffuse instantaneously over all length-scales.

To complete the description of the problem, no-slip conditions are applied on the solid boundaries. This includes the solid bounding wall located on the plane defined by $y = y_{wall}$ where $\mathbf{u}$ is zero. The fluid motion matches the rigid-body motion of the particle on the surface,

$$\mathbf{u} = \mathbf{V} + \mathbf{\Omega} \wedge (\mathbf{y} - \mathbf{X}_c)\,, \tag{3–2}$$

where $\mathbf{V} = \partial\mathbf{X}_c/\partial t$ is the center-of-mass velocity of the particle, $\mathbf{\Omega}$ is its angular velocity, and $\mathbf{y}$ is any position $\mathbf{x}$ that corresponds to the boundary of the spheroid. For positions far from the particle and bounding wall, the fluid velocity is not affected by the particle and the flow field is simply that of the imposed flow.

Options for solving Eq. 3–1 and the accompanying boundary conditions include finite difference, finite element, and finite volume methods. In these solution procedures, approximations to the partial differential equation are solved over individual elements, or spatial divisions, that define a mesh, or grid, over the fluid domain. To incorporate boundaries and enforce the conditions on these boundaries, a variety of approaches are used. Traditional techniques

utilize either a structured or unstructured grid that conforms to the boundaries between the fluid and the solid wall and particles [58]. For those elements that coincide with the boundaries, numerical schemes are implemented in order to enforce the boundary conditions. Other methods of incorporating the boundary conditions are available, including the immersed boundary [59] and level-set [60] methods, where the grid does not have to conform to the boundary. Overall, the method of approximating the Stokes equations, together with the choice of meshing method, have various trade-offs and which is best for any one problem is often unclear.

Since the goal here is to solve the motion of a particle suspended in a fluid governed by Stokes equations, rather than the more general Navier-Stokes equations, the necessity of gridding the domain can be avoided by using the boundary element method. In this approach, only the surfaces between the solid and fluid needs to be defined and, hence, the three dimensional problem of meshing the entire fluid domain is reduced to meshing the surface between the fluid and solid. This reduction of the dimensionality of the mesh is achieved by converting the partial differential equation into an integral equation using the Lorentz reciprocal theorem (Green's third identity as applied to the Stokes equations). An informative paper on the history and mathematical theory behind this method is presented by Cheng and Cheng [61] and appendix C provides an overview of the boundary integral equations, including its origins and derivations. Also, introductions to the practical application of the boundary element method can be found in many books [62–67].

Here, the boundary element method is used to solve for the motion of a spheroid near to a planar wall. The details of the formulation and the numerical solution are given in the following sections.

3.3 Problem Formulation

Applying the Lorentz reciprocal theorem to Stokes equation (Eq. 3–1) and making use of the divergence theorem to convert the volume integral over the fluid to a surface integral over the boundaries yields the boundary integral formulation of Stokes equation (see [68] or

[69] for details of the derivation):

$$\mathbf{u}\left(\mathbf{x}\right) = -\frac{1}{8\pi\mu}\iint\limits_{D}\mathbf{f}(\mathbf{y})\cdot\mathbf{G}(\mathbf{x},\mathbf{y})dS(\mathbf{y}) + \frac{1}{8\pi}\iint\limits_{D}\mathbf{u}(\mathbf{y})\cdot\mathbf{T}(\mathbf{x},\mathbf{y})\cdot\mathbf{n}dS(\mathbf{y}). \tag{3–3}$$

This equation relates the the velocity at any point $\mathbf{x}$ in the fluid to integrals over the boundaries D of the fluid which correspond to the positions $\mathbf{y}$. In the case studied here, the boundaries include the surface of the particle and potentially a planar wall that bounds the flow. To compute the velocity $\mathbf{u}(\mathbf{x})$ requires performing the integrals over the Green's function $\mathbf{G}(\mathbf{x},\mathbf{y})$ and its associated stress field (gradient) $\mathbf{T}(\mathbf{x},\mathbf{y}) = \nabla\mathbf{G}(\mathbf{x},\mathbf{y})$. These fundamental solutions of the Stokes equation are weighted by the values of $\mathbf{u}(\mathbf{y})$, the fluid velocity on the boundary, and $\mathbf{f}(\mathbf{y}) = \sigma\cdot\mathbf{n}$, the normal component of the stress tensor σ, where the normal vector $\mathbf{n}$ points from the boundary into the fluid.

Using Eq. 3–3 to solve for the motion of spheroids requires defining the appropriate Green's functions and then solving for the boundary values $\mathbf{u}(\mathbf{y})$ and $\mathbf{f}(\mathbf{y})$. Additionally, the integral equation is usually first simplified by eliminating either the single-layer (the first integral in Eq. 3–3) or the double-layer (second integral) potential. Each of these steps is described below.

Multiple Green's functions are available in the literature [68] for a variety of geometries. The Green's function for unbounded flows, where the velocity field matches the flow imposed at infinity, is used in some calculations performed here. In this case the Green's function is derived by solving the Stokes equations with a point force to give

$$\mathbf{G}(\mathbf{x},\mathbf{y}) = \frac{\mathbf{I}}{|(\mathbf{x}-\mathbf{y})|} + \frac{(\mathbf{x}-\mathbf{y})(\mathbf{x}-\mathbf{y})}{|(\mathbf{x}-\mathbf{y})|^3} \tag{3–4}$$

and the associated equation for the stress field is

$$\mathbf{T}(\mathbf{x},\mathbf{y}) = -6\frac{(\mathbf{x}-\mathbf{y})(\mathbf{x}-\mathbf{y})(\mathbf{x}-\mathbf{y})}{|(\mathbf{x}-\mathbf{y})|^5}, \tag{3–5}$$

where $|(\mathbf{x}-\mathbf{y})|$ is the separation distance between the points $\mathbf{x}$ and $\mathbf{y}$ and $\mathbf{I}$ is the identity matrix. These Green's functions are used here for simulations of the motion of spheroids far

from bounding walls in order to verify the simulation method. For simulations of spheroids in the vicinity of a bounding wall, two choices are available regarding the solution using the boundary integral method. The inferior choice is to use the free-space Green's function given above, to discretize the bounding wall in addition to the particle surface, and to then solve for the boundary values of $\mathbf{u}(\mathbf{y})$ and $\mathbf{f}(\mathbf{y})$ on the wall as well as on the particle.

The better choice is to use the Green's function that accounts for the no-slip boundary condition on the bounding walls in order to avoid the necessity of solving for the unknown values of $\mathbf{f}(\mathbf{y})$ on the wall. This significant simplification is achieved by using the Green's functions developed by Blake [70] for infinite plane walls. In this case,

$$\begin{aligned}\mathbf{T} =&\mathbf{T}^{ST}(\mathbf{x}-\mathbf{y}) - \mathbf{T}^{ST}(\mathbf{x}-\mathbf{y}+2x_2\mathbf{e}_2)\\ &+2x_2^2\mathbf{T}^{D}(\mathbf{x}-\mathbf{y}+2x_2\mathbf{e}_2) - 2x_2^2\mathbf{T}^{SD}(\mathbf{x}-\mathbf{y}+2x_2\mathbf{e}_2)\end{aligned} \tag{3–6}$$

where

$$\mathbf{T}^{ST}(\mathbf{x}-\mathbf{y}) = -6\frac{(\mathbf{x}-\mathbf{y})(\mathbf{x}-\mathbf{y})(\mathbf{x}-\mathbf{y})}{|\mathbf{x}-\mathbf{y}|^5}, \tag{3–7}$$

$$\begin{aligned}\mathbf{T}^{D}(\mathbf{x},\mathbf{y}) =&6s_T\left(-\frac{\nabla(\mathbf{x}-\mathbf{y})(\mathbf{x}-\mathbf{y})}{|(x_l-y_l)|^3}\right.\\ &\left.+5\frac{(\mathbf{x}-\mathbf{y})(\mathbf{x}-\mathbf{y})(\mathbf{x}-\mathbf{y})}{|\mathbf{x}-\mathbf{y}|^7}\right),\end{aligned} \tag{3–8}$$

$$\begin{aligned}\mathbf{T}^{SD}(\mathbf{x},\mathbf{y}) =&[(\mathbf{x}-\mathbf{y})\cdot\mathbf{e}_1]\,\mathbf{T}^{D}(\mathbf{x},\mathbf{y})\\ &+6s_T\left(\frac{\mathbf{I}(\mathbf{x}-\mathbf{y})[(\mathbf{x}-\mathbf{y})\cdot\mathbf{e}_1]-(\mathbf{x}-\mathbf{y})\mathbf{e}_1(\mathbf{x}-\mathbf{y})}{|\mathbf{x}-\mathbf{y}|^5}\right),\end{aligned} \tag{3–9}$$

and s_T (as it appears in Eqs. 3–8 and 3–9) equals minus one if $j = 1$, and is positive one otherwise. Unlike the Green's functions for flow in the absence of boundaries, the case here in Eq. 3–6 requires a clear identification of the source point ($\mathbf{x}$) and the evaluation point ($\mathbf{y}$). Note that x_2 is the distance of the source point relative to the wall position, $\mathbf{e_2}$ is the unit vector that points in the direction orthogonal to the bounding wall, and the second term of $\mathbf{T}^{ST}$ in Eq. 3–6 accounts for the disturbance velocity due to the image source. The normal component of the velocity disappears on the planar wall owing to the cancellation of the

contributions of the source and its image; the tangential velocity is set to zero by the terms $\mathbf{T}^D$ and $\mathbf{T}^{SD}$.

Eliminating either the single-layer or the double-layer potential is one way to simplify the boundary integral equation (Eq. 3–3). The resulting equation after simplification is called an *indirect* or *generalized boundary integral representation* [68]. One possibility is to eliminate the double-layer potential to give the single-layer formulation for Stokes flow,

$$\mathbf{u}\left(\mathbf{x}\right) = -\frac{1}{8\pi\mu}\iint_D \mathbf{q}(\mathbf{y})\cdot\mathbf{G}(\mathbf{x},\mathbf{y})dS(\mathbf{y}),$$

where $\mathbf{q}$ is the so-called density of the distribution which is generally not equivalent to $\mathbf{f}$. This formulation is widely used to compute flows that are both internal and external to the domain D. This formulation is a Fredholm equation of the first kind, which can lead to unstable numerical schemes upon discretization. Despite this issue, this form of the boundary integral equation has been used successfully in many calculations [71]. The second possibility is to eliminate the single-layer potential from the general boundary integral equation (Eq. 3–3). This formulation, unlike the single-layer formulation, is well-conditioned and can be used to calculate any internal flow. However, it is incapable of representing an arbitrary external flow, as demonstrated by an Eigenvalue analysis [68]. Some particular external flows can be represented by the double-layer formulation, such as force-free and torque-free problems (where the force and torque vanish over D). For more general external flows, calculations can be performed using the double-layer potential by using a compound representation. The idea is to regularize the formulation by proper modifications to suit the requirements of different external flows, such as sedimentation of particles [72], clusters of spheres [73], and more [68, 69, 74, 75]. Following an analogous strategy for problems of exterior potential flow by Pozrikidis [49], we use the compound double-layer representation for external flow,

$$\mathbf{u}(\mathbf{x}) = \boldsymbol{\mathcal{V}}(\mathbf{x}) + \iint_D \mathbf{q}(\mathbf{y})\cdot\mathbf{T}(\mathbf{x},\mathbf{y})\cdot\mathbf{n}dS(\mathbf{y}), \tag{3–10}$$

where the strength density $\mathbf{q}$ is the unknown and $\boldsymbol{\mathcal{V}}$ is a sufficiently general supplementary flow that is required to be regular in the exterior of D. Here $\mathcal{V}$ is chosen to be $\mathbf{u}^{\infty}$ the velocity field in the absence of the particle.

The general motion of any rigid particle consists of a translation with a velocity $\mathbf{V}$ and a rotation with an angular velocity $\boldsymbol{\Omega}$. Therefore, the velocity of a rigid particle is written as $\mathbf{u} = \mathbf{V} + \boldsymbol{\Omega} \otimes (\mathbf{y} - \mathbf{X_c})$, where $\mathbf{X_c}$ is the particle centroid and $\mathbf{y}$ is any position on the particle surface. Solving this mobility problem reduces to finding $\mathbf{V}$ and $\boldsymbol{\Omega}$, but first the unknown density $\mathbf{q}$ must be calculated. To do so, the field point $\mathbf{x}$ in Eq. 3–10 is moved to the particle surface D. It can be shown that the double-layer potential undergoes a jump discontinuity when $\mathbf{x}$ crosses the surface D and that the limiting value differs as $\mathbf{x}$ approaches the surface from the inside or the outside. Given that the flow is external to the particle surface, evaluating the integral gives

$$\lim_{x \to D} \Big\{ \iint_D \mathbf{q}(\mathbf{y}) \cdot \mathbf{T}(\mathbf{x}, \mathbf{y}) \cdot \mathbf{n} dS(\mathbf{t}) \Big\} = 4\pi \mathbf{q}(\mathbf{x}) + \iint_D^{PV} \mathbf{q}(\mathbf{y}) \cdot \mathbf{T}(\mathbf{x}, \mathbf{y}) \cdot \mathbf{n} dS(\mathbf{y}),$$

where the designation (PV) indicates the principal value of the improper surface integral for the case when $\mathbf{x}$ lies on the surface. Using the latter relation, Eq. 3–10) can be simplified to

$$\mathbf{u}(\mathbf{x}) = \mathbf{u}^{\infty}(\mathbf{x}) + 4\pi \mathbf{q}(\mathbf{x}) + \iint_D^{PV} \mathbf{q}(\mathbf{y}) \cdot \mathbf{T}(\mathbf{x}, \mathbf{y}) \cdot \mathbf{n} dS(\mathbf{y}).$$

Rearranging makes it clear that integral equation is of the second kind,

$$\mathbf{q}(\mathbf{x}) = -\frac{1}{4\pi} \iint_D^{PV} \mathbf{q}(\mathbf{y}) \cdot \mathbf{T}(\mathbf{x}, \mathbf{y}) \cdot \mathbf{n} dS(\mathbf{y}) + \frac{1}{4\pi} \Big[\mathbf{u}(\mathbf{x}) - \mathbf{u}^{\infty}(\mathbf{x}) \Big].$$

Substituting the boundary condition $\mathbf{u} = \mathbf{V} + \boldsymbol{\Omega} \wedge (\mathbf{x} - \mathbf{X}_c)$ gives

$$\mathbf{q}(\mathbf{x}) = -\frac{1}{4\pi} \iint_D^{PV} \mathbf{q}(\mathbf{y}) \cdot \mathbf{T}(\mathbf{x}, \mathbf{y}) \cdot \mathbf{n} dS(\mathbf{y}) + \frac{1}{4\pi} \Big[\mathbf{V} + \boldsymbol{\Omega} \wedge (\mathbf{x} - \mathbf{X}_c) - \mathbf{u}^{\infty}(\mathbf{x}) \Big]. \qquad (3\text{–}11)$$

Finally, to complete the boundary integral formulation, the translational and rotational velocities of the particle in the mobility problem are related to the strength density $\mathbf{q}$ by

$$\mathbf{V} = -\frac{4\pi}{S} \iint_D \mathbf{q}\, dS \tag{3–12}$$

and

$$\mathbf{\Omega} = -\frac{3}{2}\left(\frac{4\pi}{S}\right)^2 \iint_D (\mathbf{y} - \mathbf{X}_c) \wedge \mathbf{q}\, dS, \tag{3–13}$$

where S is the surface are of the particle. So using the integral equation (Eq. 3–11), we can compute the strength density $\mathbf{q}$ from which we can find the translational and angular velocities of the particle. In order to compute the integral equation, the singular principal-value (PV) integral can be computed using the integral identity

$$\iint_D^{PV} \mathbf{q}(\mathbf{y}) \cdot \mathbf{T}(\mathbf{x}, \mathbf{y}) \cdot \mathbf{n} dS(\mathbf{y}) = \iint_D (\mathbf{q}(\mathbf{y}) - \mathbf{q}(\mathbf{x})) \cdot \mathbf{T}(\mathbf{x}, \mathbf{y}) \cdot \mathbf{n} dS(\mathbf{y}) - 4\pi \mathbf{q}(\mathbf{x}).$$

3.4 Numerical Method

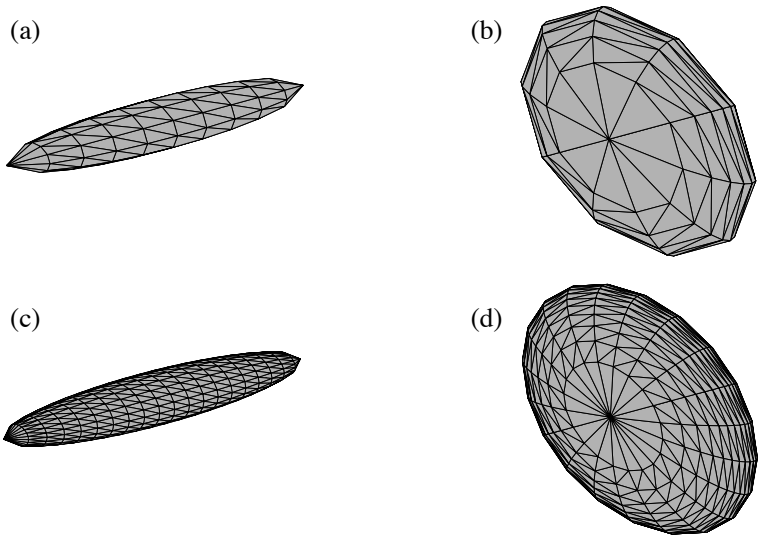

Figure 3-4. Example meshes for the spheroid surfaces, including a discretization of 92 nodes and 180 elements for (a) a prolate spheroid with aspect ratio $e = 5$ and for (b) an oblate spheroid with aspect ratio $e = 0.2$. A mesh composed of 382 nodes and 760 elements is also shown for the (c) prolate ($e = 5$) and (d) oblate ($e = 0.2$) spheroids.

The integral equation (Eq. 3–11) is solved for the strength density $\mathbf{q}$ by discretizing the surface into small elements, over each of which an approximation to $\mathbf{q}$ is made. To evaluate the overall integral for any particular choice of the position $\mathbf{x}$ located on the particle surface, the approximation is used to evaluate an integral over each element and then the integral over each element is summed. By choosing $3L$ different positions of $\mathbf{x}$, where L corresponds to the total number of terms in the approximation of $\mathbf{q}(\mathbf{x})$, a linear algebraic system of equations is produced. Solving this system of equations gives $\mathbf{q}(\mathbf{x})$, from which the velocities and rotational velocities can be evaluated.

This boundary element-collocation procedure requires gridding, or meshing, the domain of the integration (spheroidal particle surface) and then solving the integral equation by specifying an approximation for the unknown strength density, integrating, and solving the resulting linear algebraic system. The particle surface is discretized into a grid of planar triangles; examples of the mesh are shown in Fig. 3-4. Additionally, in order to compute the boundary integrals for each element, we use a standard numerical method (local approximation of the strength density over each element using linear shape functions and integration using Gaussian quadrature). Finally, a set of algebraic equations is generated using collocation, from which the strength density is determined. Each of these steps in the solution procedure is described in the following sections.

3.4.1 Integration Domain and Definition of Vectors

First, the spheroid surface, which is the domain of integration, is defined. The lengths of the semi-principal axes of the spheroid surface are a, b, c. In the Cartesian coordinate system defined by the axes $\mathbf{X}$ where the origin is the center of the particle, we align the axes so that $-a < X < a$, $-b < Y < b$, and $-c < Z < c$ as illustrated in Fig. 3-5. In all problems studied here, b and c are restricted to be equivalent; the particles can be either prolate ($a > b$) or oblate ($a < b$) (Fig. 3-4). The equation of the spheroid is

$$\frac{X^2}{a^2} + \frac{Y^2}{b^2} + \frac{Z^2}{b^2} = 1. \tag{3–14}$$

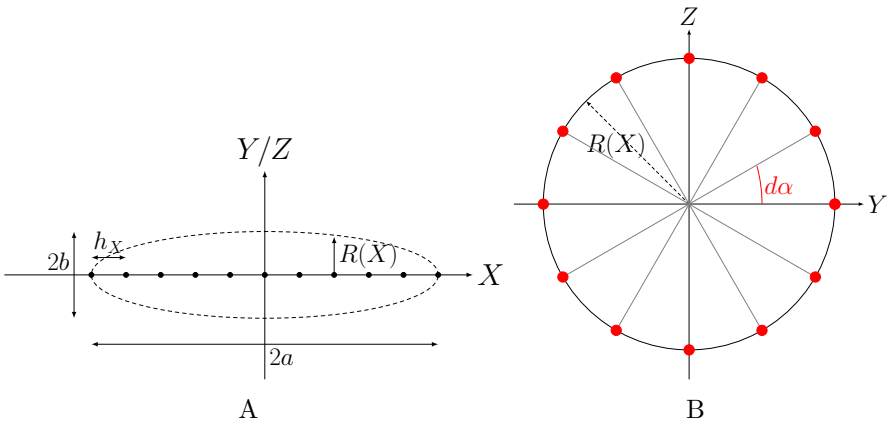

Figure 3-5. **(A)** Discretization of the X axis into a set of positions separated by h_X. **(B)** For each X position, a circle is drawn with radius $R(X)$ corresponding to the circumference of the particle at that point. Then the circumference is discretized to define the nodes (in red) separated by $d\alpha$.

Constructing a network of nodes begins by discretizing the semi-major axis X into N_1 elements. We discretize the axis in equal increments of $h_X = 2a/N_1$. The next operation traces circles in the $Y - Z$ planes, with radii that correspond to the circumference of the particle at each point X. This radius is given by

$$R(X) = b * \sqrt{1 - \left(\frac{X}{a}\right)^2}. \tag{3–15}$$

These circles are divided into N_2 elements with an angular resolution of $d\alpha = 2\pi/N_2$.

The node positions can be written as

$$X(i,k) = -a + (k-1)h_X,$$

$$Y(i,k) = R_k \cos(\alpha_i) = b\sqrt{1 - \left(\frac{X(i,k)}{a}\right)^2} \cos(i \cdot d\alpha),$$

and

$$Z(i,k) = R_k \sin(\alpha_i) = b\sqrt{1 - \left(\frac{X(i,k)}{a}\right)^2} \sin(i \cdot d\alpha),$$

where k and i are the indexes indicating the node number along the X axis and the radial direction, respectively. A vector N_o is then defined to store the positions of all the nodes, where (X_n, Y_n, Z_n) are the coordinates of node n. The length of the vector N_o is $3L$, where

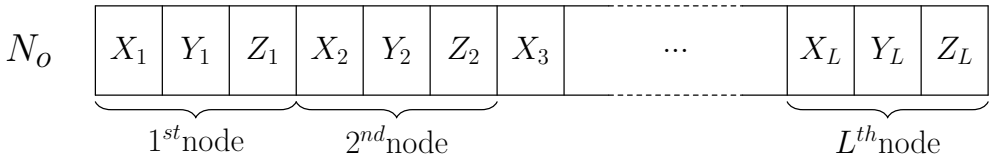

$L = N_2(N_1 - 1) + 2$ is the total number of nodes.

After specifying the nodal positions, a network of planar triangles, or elements, is created, where the vertices are three nodes (Fig. 3-6). As a result, the surface of the ellipsoid is composed of numerous triangular elements connected together by nodes on their boundaries. Numerically, a matrix Elm is created to store the connectivity of the nodes that build each element ($Elm = [1, 2, 3; 1, 3, 4; ..., L]$). The number of elements is $H = 2N_2(N_1 - 1)$.

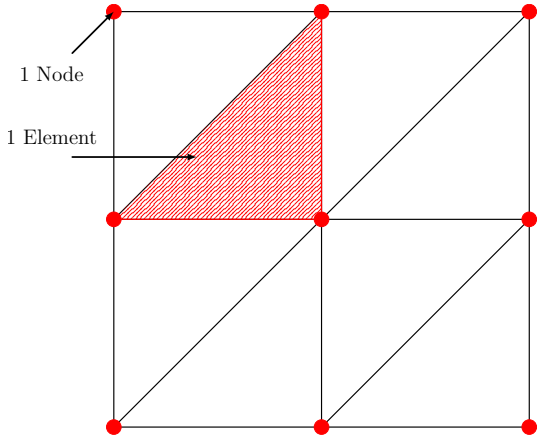

Figure 3-6. Representation in two dimensions of the surface mesh. Each element is defined by the nodes at the vertices.

Simulating the dynamics requires moving and rotating the particle within the global coordinate system. Taking any point of the particle surface, we rotate it around the z-axis by the angle θ and then around the x-axis by the angle ϕ. Once the rotation is done, the spheroid can be translated to the correct position $\mathbf{X}_c$ using a translation step. The first rotation moves a node at $\mathbf{X}$ to the new position $\mathbf{X}'$ according to $\mathbf{X}' = \mathbf{R}_1 \cdot \mathbf{X}$, where $\mathbf{R}_1$ is

the first rotation matrix,

$$\begin{vmatrix} X' \\ Y' \\ Z' \end{vmatrix} = \begin{vmatrix} \cos\theta & -\sin\theta & 0 \\ \sin\theta & \cos\theta & 0 \\ 0 & 0 & 1 \end{vmatrix} \cdot \begin{vmatrix} X \\ Y \\ Z \end{vmatrix}.$$

The second rotation by the angle ϕ is given by $\mathbf{x}' = \mathbf{R}_2 \cdot \mathbf{X}'$, where

$$\begin{vmatrix} x' \\ y' \\ z' \end{vmatrix} = \begin{vmatrix} 1 & 0 & 0 \\ 0 & \cos\phi & -\sin\phi \\ 0 & \sin\phi & \cos\phi \end{vmatrix} \cdot \begin{vmatrix} X' \\ Y' \\ Z' \end{vmatrix},$$

and the global rotation is then defined by the matrix

$$R = \begin{vmatrix} \cos\theta & -\sin\theta & 0 \\ \cos\phi.\sin\theta & \cos\phi.\cos\theta & -\sin\phi \\ \sin\phi.\sin\theta & \sin\phi.\cos\theta & \cos\phi \end{vmatrix}.$$

To complete the spheroid motion, a translation needs to be defined. Mathematically, it can be written as $\mathbf{x} = \mathbf{x}' + \mathbf{X}_c$.

To approximate the unit normal vector to the surface at each node, the particle surface is described by the parametric representation

$$\left\{ \begin{array}{rc} x = & a\sin\chi\cos\psi \\ y = & b\sin\chi\sin\psi \\ z = & c\cos\chi \end{array} \right\},$$

where $0 < \psi < 2\pi$ and $0 < \chi < \pi$. For each node position $\boldsymbol{x}_i = (x_i, y_i, z_i)$, the two corresponding angles ψ_i and χ_i can be computed from

$$\chi_i = \arccos\left(\frac{z_i}{b}\right) \qquad \text{and} \qquad \psi_i = \arctan\left(\frac{ay_i}{bx_i}\right). \tag{3–16}$$

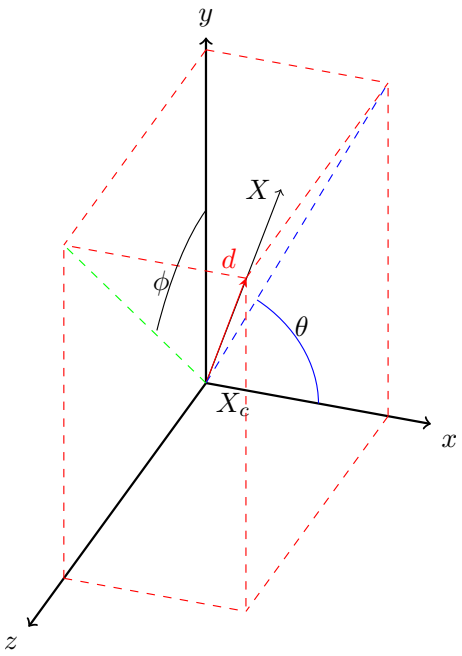

Figure 3-7. Rotation of the spheroid particle. Rotation is first performed around the z-axis by the angle θ and then around the x-axis by the angle ϕ.

Then the normal unit vector at any node can be calculated using

$$\mathbf{n}_i = \frac{1}{J} \left| \begin{array}{l} b^2 \sin^2(\chi_i) \cos(\psi_i) \\ ab \sin^2(\chi_i) \sin(\psi_i) \\ ab \sin(\chi_i) \cos(\chi_i) \end{array} \right\}, \tag{3–17}$$

where the Jacobian J is given by

$$J = \left[b^4 \sin^4(\chi_i) \cos^2(\psi_i) + a^2 b^2 \sin^4(\chi_i) \sin^2(\psi_i) + a^2 b^2 \sin^2(\chi_i) \cos^2(\chi_i) \right]^{1/2}. \tag{3–18}$$

A table "*Normal*" of the three components of the normal vector at each node is constructed,

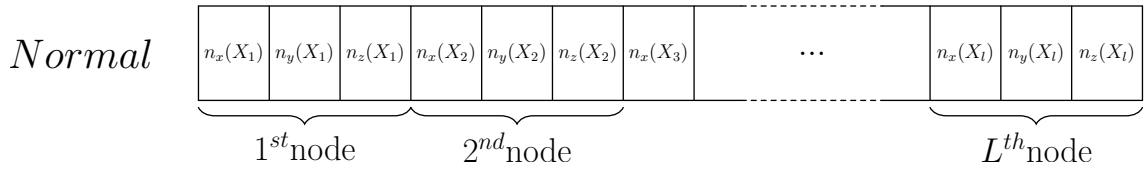

To evaluate the surface area S of the particle, as approximated by the mesh of planar triangles, the surface area of each element is summed. Since the elements are flat triangles,

the area of each element j is

$$s_j = \frac{1}{2} \left\| (\mathbf{x}_2 - \mathbf{x}_1) \wedge (\mathbf{x}_3 - \mathbf{x}_1) \right\|, \tag{3–19}$$

where $\mathbf{x}_1$, $\mathbf{x}_2$ and $\mathbf{x}_3$ are the coordinate positions of the three vertices of the element and $\|\cdot\|$ indicates the magnitude. The total numerical area is then $S = \sum_{j=1}^{H} s_j$, where H is the number of elements. The surface area of the spheroid that is modeled by the surface mesh is

$$2\pi b^2 + 2\pi ab \frac{\arcsin(\left(1 - \frac{b^2}{a^2}\right)^{1/2})}{\left(1 - \frac{b^2}{a^2}\right)^{1/2}}. \tag{3–20}$$

The numerical surface area S is used for consistency and, for all calculations reported here, the error between the area of the mesh and the theoretical area of the particle is less than 2%.

3.4.2 Solving the Integral Equation

Over each triangular element, the strength density $\mathbf{q}$ is represented by linear functions,

$$\mathbf{q}(\mathbf{y}) = \sum_{m=1}^{3} \left[\boldsymbol{\alpha}_m \eta_m(\mathbf{y}) \right] \tag{3–21}$$

where $\mathbf{y}$ is within the plane of the element and $\eta_m(\mathbf{y})$ are the three (linear) shape functions that are chosen so that the value of $\mathbf{q}$ at any of the three nodes m of the element is simply given by $\boldsymbol{\alpha}_m$. To perform an integral of the form

$$\int_h \mathbf{q}(\mathbf{y}) \cdot \mathbf{K}(\mathbf{y}) \, dS \tag{3–22}$$

over any one element h, where $\mathbf{K}$ and $\mathbf{q}$ are functions of position, a three-point Gaussian quadrature rule is utilized. Consequently, the integral is approximated by the sum

$$\sum_{n=1}^{3} \mathbf{q}(\mathbf{y}_n) \cdot \mathbf{K}(\mathbf{y}_n) \, w_n s_h \tag{3–23}$$

where $\mathbf{y}_n$ and w_n are the Gaussian quadrature points and weights. The element (h) has an area of s_h. Combining this with the linear representation of the strength density in Eq. 3–21

gives

$$\sum_{n=1}^{3}\left\{\sum_{m=1}^{3}\boldsymbol{\alpha}_m\eta_m\left(\mathbf{y}_n\right)\right\}\cdot\mathbf{K}\left(\mathbf{y}_n\right)w_n s_h \tag{3–24}$$

as an approximation to the integral over a single element. An additional sum over all of the elements, of which there are H, is required to compute the integral over the entirety of the particle surface. In these calculations, the global coordinate is mapped to a local master element over which these calculations are performed; the details of these calculations can be found in any standard text that covers the boundary element, or even finite element [76], methods.

Applying the above approximations to Eqs. 3–11 through 3.3, where the point of evaluation $\mathbf{x}_e$ corresponds to node e, gives

$$\begin{aligned}\frac{1}{4\pi}\mathbf{u}^{\infty}\left(\mathbf{x}_e\right) = &-\frac{1}{4\pi}\sum_{h=1}^{H}\left[\sum_{n=1}^{3}w_n\left(\sum_{m=1}^{3}\boldsymbol{\alpha}_m\eta_m\left(\mathbf{y}_n\right)-\boldsymbol{\alpha}_e\right)\cdot\mathbf{T}\left(\mathbf{y}_n\right)\cdot\mathbf{n}_h s_h\right]\\ &-\frac{1}{S}\sum_{h=1}^{H}\left[\sum_{n=1}^{3}w_n\left(\sum_{m=1}^{3}\boldsymbol{\alpha}_m\eta_m\left(\mathbf{y}_n\right)\right)s_h\right]\\ &-\frac{6\pi}{S^2}\sum_{h=1}^{H}\left[\sum_{n=1}^{3}w_n\left(\sum_{m=1}^{3}\left(\mathbf{y}_n-\mathbf{X}_c\right)\wedge\boldsymbol{\alpha}_m\eta_m\left(\mathbf{y}_n\right)\wedge\left(\mathbf{x}_e-\mathbf{X}_c\right)\right)s_h\right],\end{aligned} \tag{3–25}$$

where $\mathbf{n}_h$ is the outward unit normal vector for element h. There are a total of L nodes where the values of $\boldsymbol{\alpha}$ must be determined. By evaluating Eq. 3–25 L times, where the evaluation point $\mathbf{x}_e$ is chosen to be the L node position, a system of L equations with L unknowns results,

$$\mathbf{A}\cdot\mathbf{Q}=\mathbf{U},$$

which is solved to give $\mathbf{Q}$, a vector containing the $3L$ unknown values of $\boldsymbol{\alpha}$ that represent the solution for the strength density $\mathbf{q}$. Then, the translational and angular velocities ($\mathbf{V}$ and $\boldsymbol{\Omega}$) of the particle can be calculated by performing the integrations over the strength density as indicated in Eqs. 3–12 and 3–13. To resolve the trajectory of the particle, the particle position and orientation is updated using an Euler integration, where the translation and rotation relies on the methods for moving the particle as described previously.

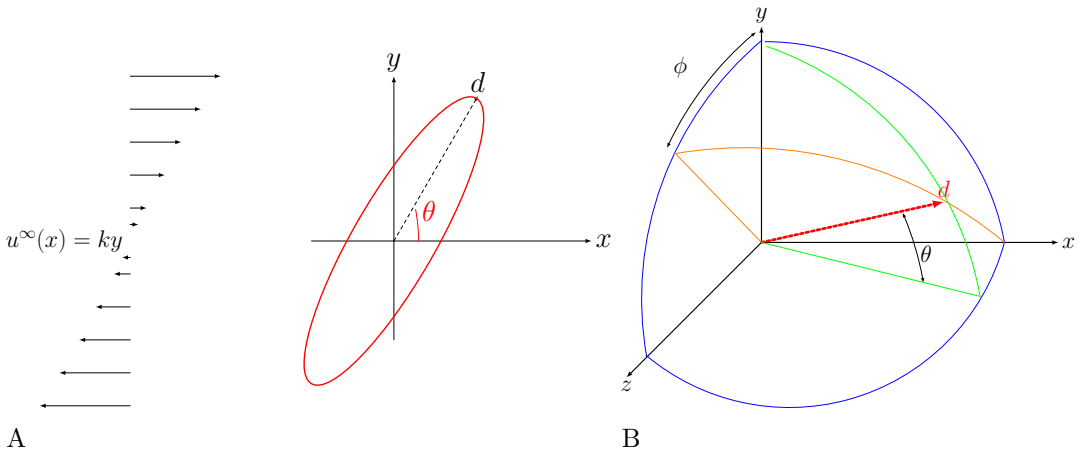

Figure 3-8. **(A)** Ellipsoid particle freely suspended in a shear flow, initially orientated in the flow-gradient plane. **(B)** Coordinate systems for describing particle rotations.

3.5 Results

3.5.1 Particle Motion in an Unbounded Shear Flow

To test the performance and accuracy of the numerical code, simulations were performed on an ellipsoid particle suspended in a simple shear flow in the absence of any boundaries. Consequently, the Green's function for unbounded flow is used when evaluating $\mathbf{T}$ (Eq. 3–5) and the undisturbed flow is taken to be $\mathbf{u}^\infty = [ky, 0, 0]$, where k is the rate of shear as illustrated in Fig. 3-8A.

The simulation outcomes are compared with the analytical solution of Jeffery [77] for the motion of a spheroidal particle in a shearing flow. Jeffery's analysis showed that a spheroid, on which no net torque is exerted, executes a periodic orbiting motion. The rotation depends on the aspect ratio, $e = a/b$, and the initial orientation of the spheroid with respect to the flow. The results of Jeffery were written in a compact form by Leal and Hinch [78],

$$\dot{\mathbf{d}} = \mathbf{w} \cdot \mathbf{d} + \frac{e^2 - 1}{e^2 + 1}(\mathbf{I} - \mathbf{dd}) \cdot \mathbf{E} \cdot \mathbf{d}, \tag{3–26}$$

where $\mathbf{d}$ represents the orientation of the particle as shown in Fig. 3-3 and $\dot{\mathbf{d}} = \partial \mathbf{d}/\partial t$. The rod rotates with the rate of rotation of the shearing flow, $\mathbf{w} = \frac{1}{2}[(\nabla \mathbf{u}^\infty) - (\nabla \mathbf{u}^\infty)^T]$, and $\mathbf{E}$ is the rate of strain tensor, $\mathbf{E} = \frac{1}{2}[(\nabla \mathbf{u}^\infty) + (\nabla \mathbf{u}^\infty)^T]$.

This prediction of Eq. 3–26 has been validated experimentally by several workers [79–81]. The first experiments were performed by Trevelyan and Mason [80] using a Couette apparatus. They checked the angular velocity of a spherical particle as well as the orbits of prolate cylinders and found excellent accord with Jeffery's theory. Most of the experiments, though, examined the motion of particles for which $\phi = 0$ (alignment of the particle in the flow-gradient plane).

3.5.1.1 Spheroid rotating in the flow-gradient plane

For the specific case of $\phi = 0$, the exact solution for the angular velocity can be reduced to

$$\Omega_z = \frac{d\theta}{dt} = -\frac{k}{2}\Big(1 - \frac{e^2-1}{e^2+1}\cos(2\theta)\Big). \tag{3–27}$$

Jeffery also showed that the time necessary for a spheroid to complete a rotation through an angle of $\theta = 2\pi$ is

$$T_p = \frac{2\pi(e + 1/e)}{k} \tag{3–28}$$

and that the evolution of the angle in time is [82]

$$\tan(\theta) = e\tan(2\pi t/T_p). \tag{3–29}$$

Figures 3-9 and 3-10 respectively show a comparison of the exact solution and numerical solutions for the angular velocity Ω_z as a function of the inclination angle θ and the change of θ in time. In the simulations, the particle was discretized into 40, 180 and 760 triangular elements and aspect ratios of $e = 5$ (prolate spheroid) and $e = 1/5$ (oblate spheroid) were both tested. If the director vector $\mathbf{d}$ of the particle is perpendicular to the flow ($\theta = \pi/2$ for $e > 1$ and $\theta = 0$ for $e < 1$), the angular velocity is at its maximum and, if the particle is parallel to the flow ($\theta = 0$ for $e > 1$ and $\theta = \pi/2$ for $e < 1$), the angular velocity is minimum. The error is small between the numerical result and exact answer, and diminishes as the number of elements increases.

For calculating the angular position as a function of time (Fig. 3-10), the particle surface was again discretized into 40, 180 and 760 triangular elements; the time step was set to

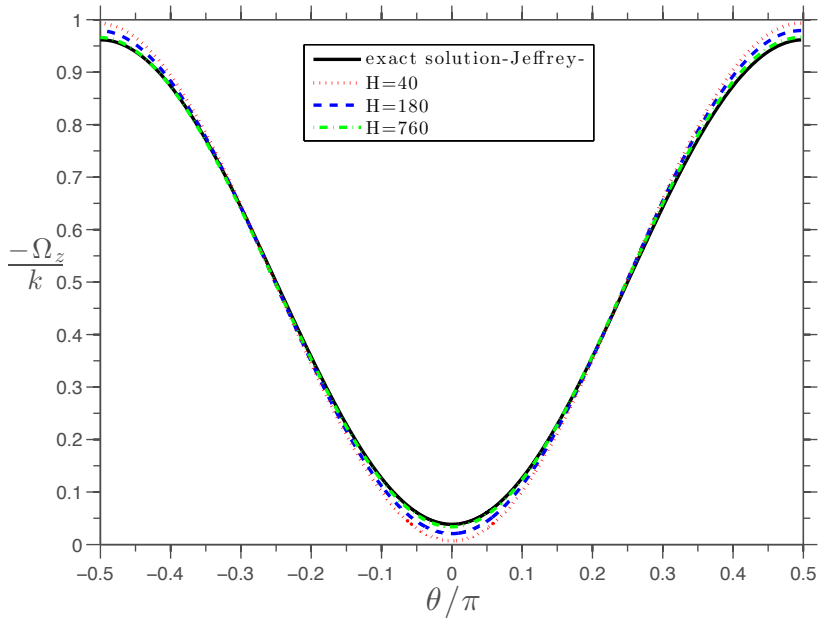

A

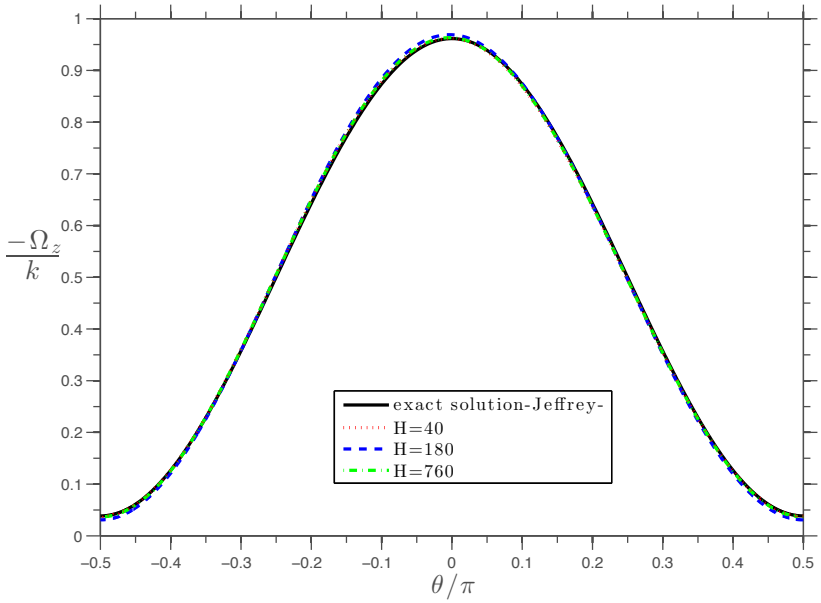

B

Figure 3-9. Angular velocity of spheroidal particles in the configuration $\phi = 0$ (aligned in the flow-gradient plane): **A)** prolate ellipsoid with aspect ratio $e = 5$ and **B)** oblate ellipsoid with aspect ratio $e = 1/5$.

$\Delta t = 0.1$ and the shear flow coefficient $k = 0.1$. While the angular velocity was approximated well by simulations using just 40 elements (see Fig. 3-9), accurately resolving the angular

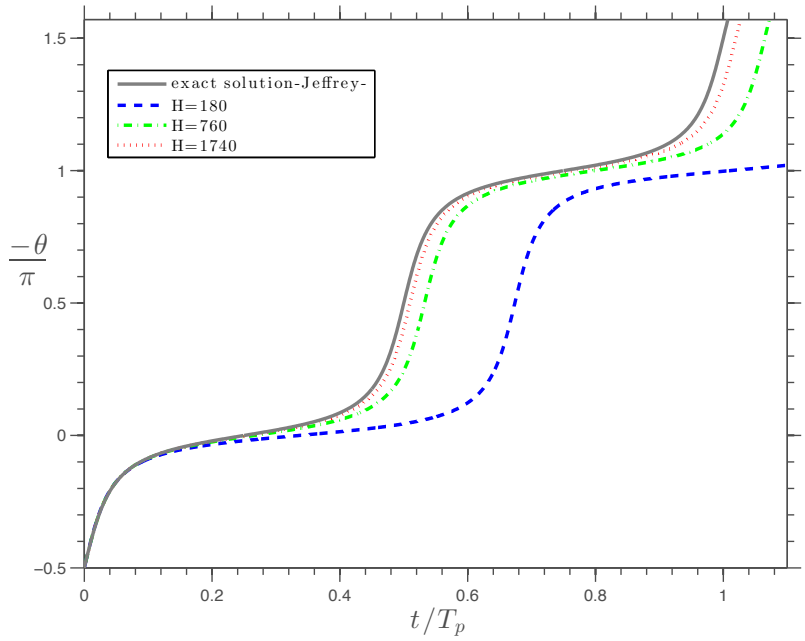

A

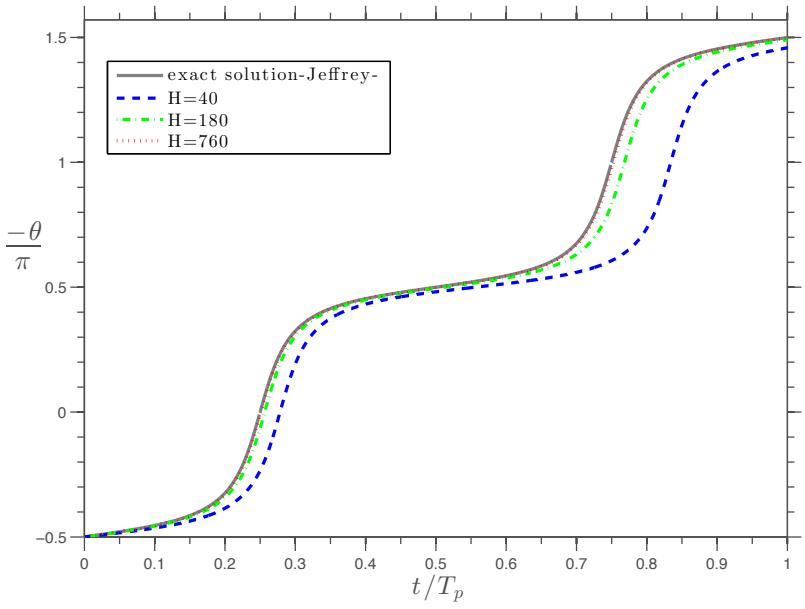

B

Figure 3-10. Rotational motion of spheroids in the symmetric configuration, $\phi = 0$: **A)** prolate ellipsoid with aspect ratio $e = 5$ and **B)** oblate ellipsoid with aspect ratio $e = 1/5$.

position in time requires many more elements. Note that the angle θ is just the integral of the angular velocity and, therefore, a small error in the angular velocity approximation can

lead to high errors in the angular position as time increases. For example, the results in Fig. 3-10 clearly show that the discrepancy between the exact and numerical solutions increases in time.

3.5.1.2 Spheroidal particle rotating in three dimensions

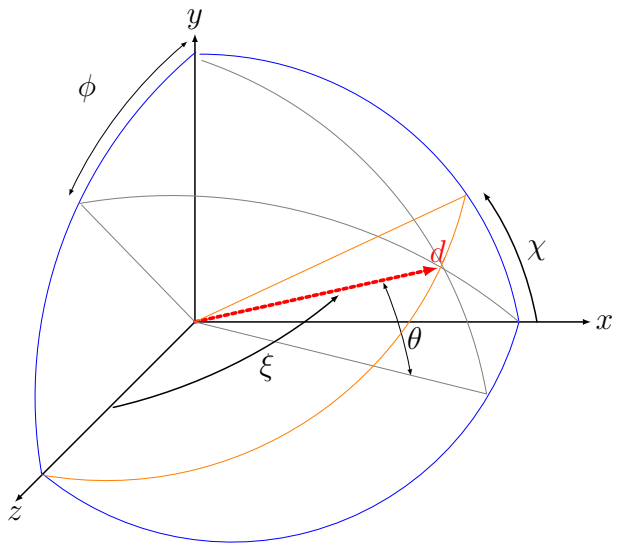

Figure 3-11. Coordinate system describing particle rotations for Jeffery's equation.

Rotation occurs out of the $x-y$ plane if the initial azimuthal angle $\phi \neq 0$. The particle still executes periodic rotations on specific orbits, which depend on the initial orientation of the spheroid. These orbits are called "Jeffery orbits" and each orbit is parameterized by a constant C ($0 \leq C \leq \infty$) that corresponds to the initial azimuthal angle. An orbit constant of $C = \infty$ represents the situation described in the last section, where the particle remains in the $x-y$ plane ($\phi = 0$); on the other hand, $C = 0$ represents the alignment of $\mathbf{d}$ with the vorticity axis (z) and the rotation of the particle occurs around $\mathbf{d}$. For a prolate particle, this latter motion is often described as "log-rolling", whereas the motion resembles a coin rolling on its edge for an oblate particle.

Jeffery orbits are described here using the coordinates χ and ξ as shown in Fig. 3-11. The coordinates are related to the orbit constant C through the equation

$$\tan(\xi) = \frac{C}{\left(e^2 \sin^2(\chi) + \cos^2(\chi)\right)^{1/2}}. \tag{3–30}$$

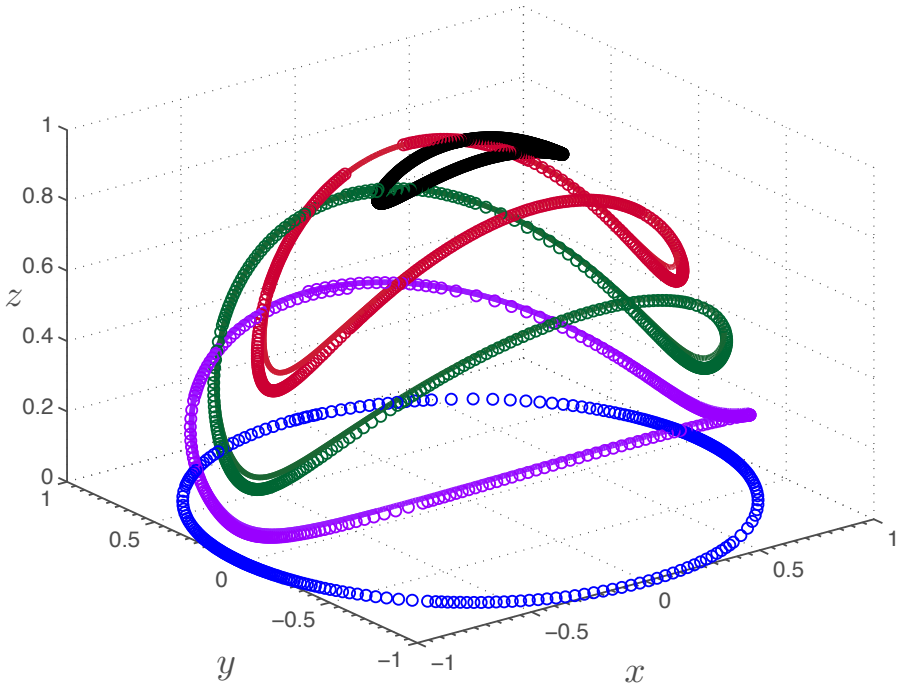

Figure 3-12. Computer simulation of the particle orbits for different initial azimuthal angles: $\phi_0 = 0$ (blue color), $\phi_0 = \pi/8$ (pink color), $\phi_0 = \pi/4$ (green color), $\phi_0 = 3\pi/8$ (red color), $\phi_0 = 3\pi/6.4$ (black color). The circular symbols represent the results of the numerical simulations, and the nearly coincident solid lines represent the Jeffrey orbits for an unbounded shear flow. The particle is a prolate ellipsoid with an aspect ratio $e = 4$ discretized into 1740 elements subject to the initial conditions $\theta = \pi/2$, $\phi = \phi_0$ and a time step $dt = 0.3$.

For example, consider the case of $\theta = \chi = \pi/2$. This situation corresponds to the particle orientation $\mathbf{d}$ lying in the $x - y$ plane and $\xi = \pi/2 - \phi$. For this configuration, Eq. 3–30 gives a Jeffery constant of

$$C = e\tan(\xi) = e\tan(\pi/2 - \phi) = e\cot\phi.$$

The Cartesian coordinates can be calculated from the coordinates ξ and χ:

$$\begin{aligned} d_x &= \sin\chi\cos\xi \\ d_y &= \sin\chi\sin\xi \\ d_z &= \cos\chi. \end{aligned}$$

Fig. 3-12 shows the motion for five different values of the initial orientation. In all cases, the orientation vector **d** describes a unique, closed orbit around the vorticity axis. Figure 3-12 shows these orbits for different azimuthal angles (ϕ) corresponding to different Jeffery constants (C). The numerical and analytical solutions are indistinguishable, demonstrating the accuracy of the method and the validity of the developed code.

3.5.2 Particle Motion Near to a Wall

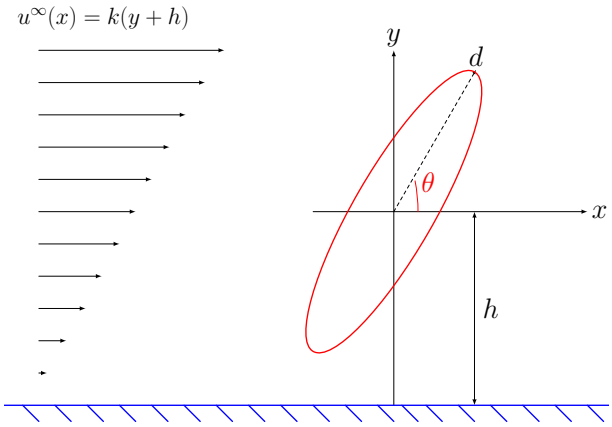

Figure 3-13. The initial position of a spheroidal particle in a shearing flow near a planar bounding wall. The initial particle distance from the wall is h, x is the flow direction, and y is the gradient direction.

A plane wall has been added at a distance h from the center of the spheroidal particle as shown in Fig. 3-13. To perform the calculations, the Green's function for unbounded flows is replaced with a Green's function that ensures that the tangential and normal components of fluid velocity vanish on the bounding wall; this function, due to Blake [70], is given in Eq. 3–6.

First, results are presented for particles that have been initially placed with an orientation **d** in the flow-gradient plane ($\phi = 0$). Figures 3-14 and 3-15 show the dependence of the motion on the spacing of the wall for a prolate ($e = 4$) and oblate $e = 1/4$ spheroid, respectively. As compared to the motion in an unbounded flow, the angular velocity and the orbit of the particle near to the wall changes little. Unlike the case of an unbounded flow however, the presence of the wall causes a periodic motion of the particle in the direction

transverse to the boundary, as seen in panel A of Figs. 3-14 and 3-15. The motion is generated by velocity disturbances that are reflected by the wall; in the absence of the wall, these disturbances decay as the distance from the particle increases. These velocities are shown for both the prolate and oblate spheroids as functions of the orientation θ and the distance h from the wall. The dependence of the transverse velocity V_{Y_c} on the angle with respect to the wall is complex, showing multiple inflection points, and hence the position also exhibits a complicated pattern. Importantly however, the motion is reversible and results in no net migration of the particle, as required by the assumptions of a purely viscous flow of a force-free particle. The figures also show that the amplitude of the center motion decreases as the distance h between the particle and wall increases. For $h \geqslant 10a$, the center of mass motion in the direction transverse to the wall disappears, in agreement with results from the calculations of the particles in the absence of a boundary.

The velocity disturbances that are reflected from the wall also alter the motion of the particle along the flow direction, as seen in Figs. 3-14C and 3-15C. The velocity is reduced, with the effect being slightly larger for the oblate spheroid than the prolate spheroid. For a spheroid far from the wall, the velocity of the center of mass returns to that of the imposed flow, as expected. Although the reduction in the rotational velocity is small due to the presence of the wall, the total time required to complete one rotation shifts substantially (up to 20%, see Figs. 3-14D and 3-15D) as compared to the expected period of rotation T_p predicted for a spheroid for from a boundary.

The velocity at which the spheroids move away or towards the wall depends upon the aspect ratio as well as the angle and distance from the wall. For spheres ($e = 1$), the transverse velocity, as seen in Fig. 3-16A and B, vanishes; while true that the shear flow acting on the sphere, like the spheroids, generates a flow disturbance, the reflected components of the disturbance cancel. Results for the transverse velocity, upon increasing e past one, demonstrate a complicated dependence on the aspect ratio. Multiple changes in the direction of migration can be observed, depending upon the angle of the particle, as the apsect ratio

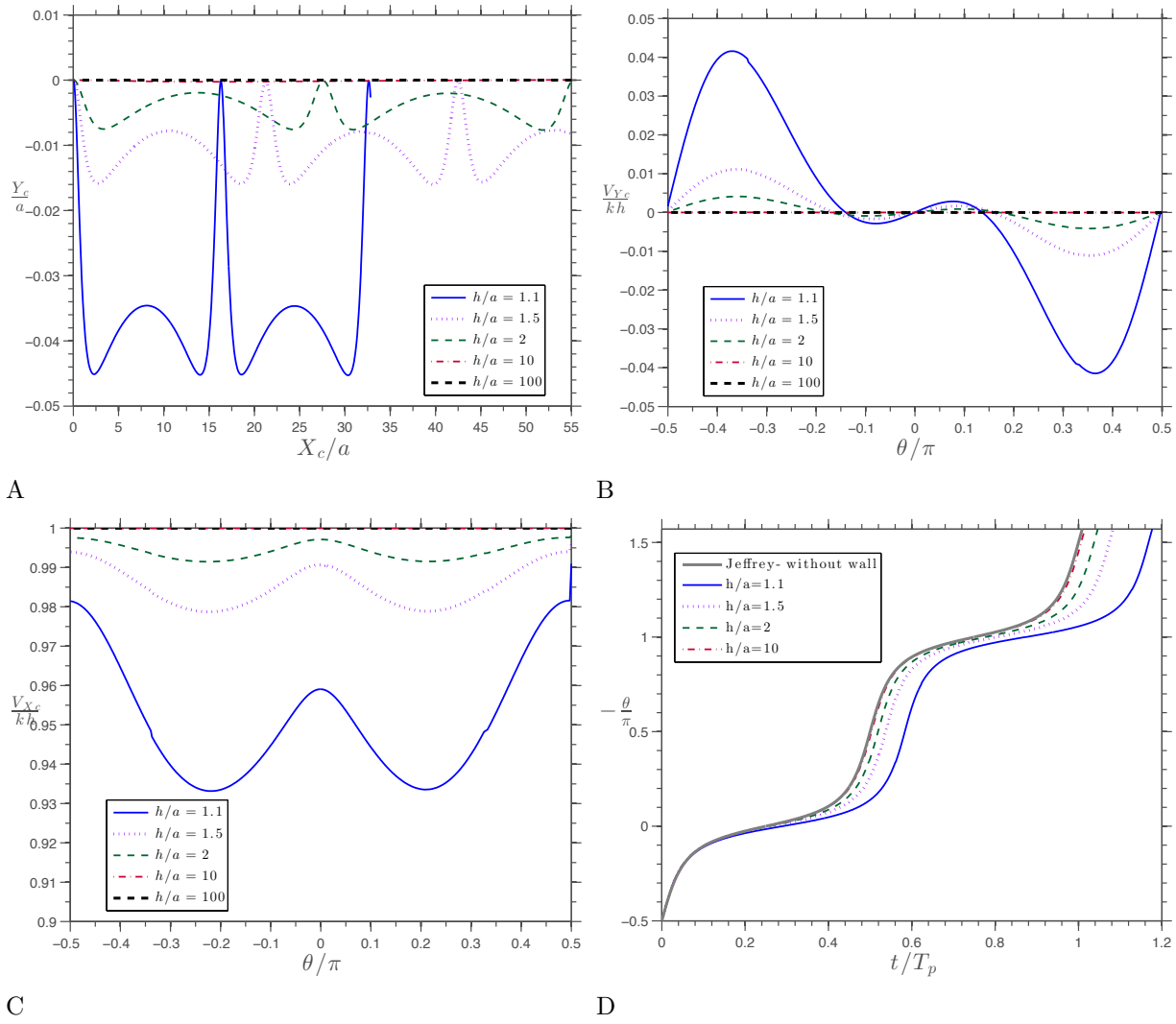

Figure 3-14. Effect of the wall distance on motion of an ellipsoid (prolate spheroid) of aspect ratio $e = 4$. In these simulations, the particle was discretized into 1740 elements and was oriented in the flow-gradient plane ($\phi = 0$). **(A)** The trajectory of the center of the particle is shown for five initial distances from the wall. The particle remains on the $x - y$ plane on which it starts. **(B)** Lift velocity with respect to the orientation angle of the ellipsoid. **(C)** Horizontal velocity with respect to the orientation angle. **(D)** Evolution of the orientation with respect to the normalized time t/T_p.

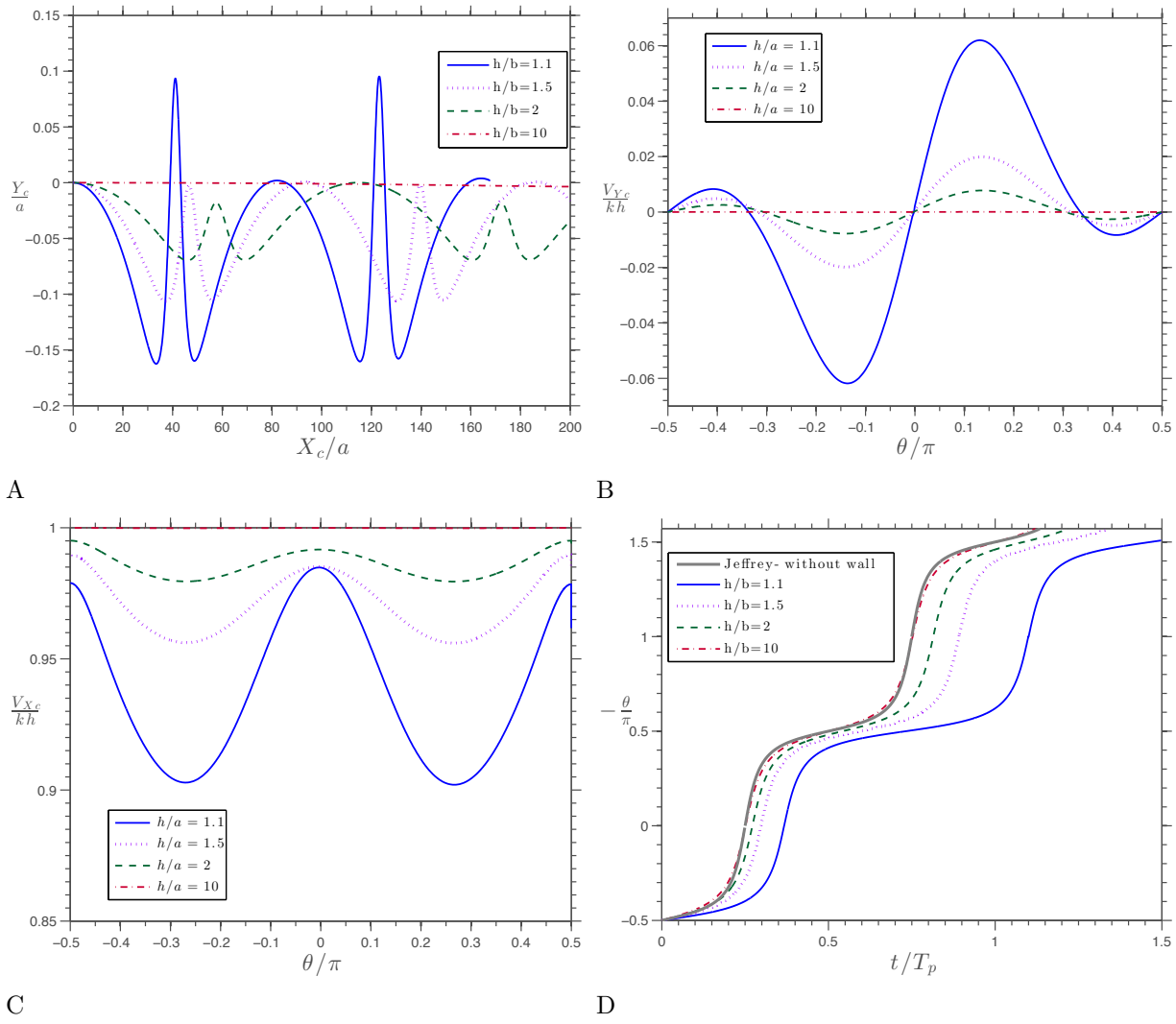

Figure 3-15. Effect of the wall distance on motion of an ellipsoid (oblate spheroid) of aspect ratio $e = 1/4$. In these simulations, the particle was discretized into 760 elements and oriented in the flow gradient plane ($\phi = 0$). **(A)** The trajectory of the center of the particle is shown for four initial distances from the wall. The particle remains on the $x - y$ plane on which it starts. **(B)** Lift velocity with respect to the orientation angle of the ellipsoid. **(C)** Horizontal velocity with respect to the orientation angle. **(D)** Evolution of the orientation with respect to the normalized time t/T_p.

changes. As stated by Gavze and Shapiro [50], the transverse velocity must return to zero as the aspect ratio goes to infinity. Work here extends the results past $e = 10$, the largest result reported by Gavze and Shapiro [50], to nearly $e = 100$. The value of V_{Y_c} approaches zero asymptotically with a scaling of $\ln(e)$, as seen by the dotted lines in Fig. 3-16A. This scaling was predicted by slender body theory [52, 53].

Figures 3-17A and B show the dependence of V_{Y_c} on aspect ratio for $e < 1$ (oblate spheroids). Similarly to the prolate spheroids, the value can be positive or negative at any particular angle θ as the aspect ratio is changed. Overall the oblate spheroid exhibits a larger maximum velocity than the prolate: the prolate spheroid attains a velocity V_{Y_c} of almost $0.05kh$ for $e \approx 2$, wheras the oblate velocity can be as high as nearly $0.015kh$ for $e \approx 3/4$. Oblate spheroids were studied for aspect ratios as low as 0.1, expanding upon those results given in previous works, such as Gavze and Shapiro [50]

The horizontal component of the velocity (V_{X_c}) is a monotonic function of the aspect ratio for both prolate and oblate spheroids, as seen in Figs. 3-16C, 3-16D, 3-17C, and 3-17D. The horizontal velocity is most influenced by the wall when the particle is spherical and is uninfluenced by the wall as the aspect ratio goes toward infinity.

To examine the results under more general conditions, the motion of a prolate spheroid with an aspect ratio of $e = 4$ was calculated for initial conditions where the initial orientation d of the particle lies outside of the flow-gradient plane (i.e. $\phi \neq 0$). Results for the center position and velocities are shown in Figs. 3-18 and 3-19, while Fig. 3-20 plots the center position in time along with the orientation to aid with visualization of the complicated motion.

Figures 3-18A and 3-18C show the motion of the particle center for $h/a = 1.25$. These results match the results of Pozrikidis [49], to which comparison are made in the figure, demonstrating again that the simulation code is valid. Similarly to the case of $\phi = 0$, note that the wall has almost no effect on the orbits shown in Fig. 3-12. The most striking difference from the previously presented results is the excursions of the particle center in the

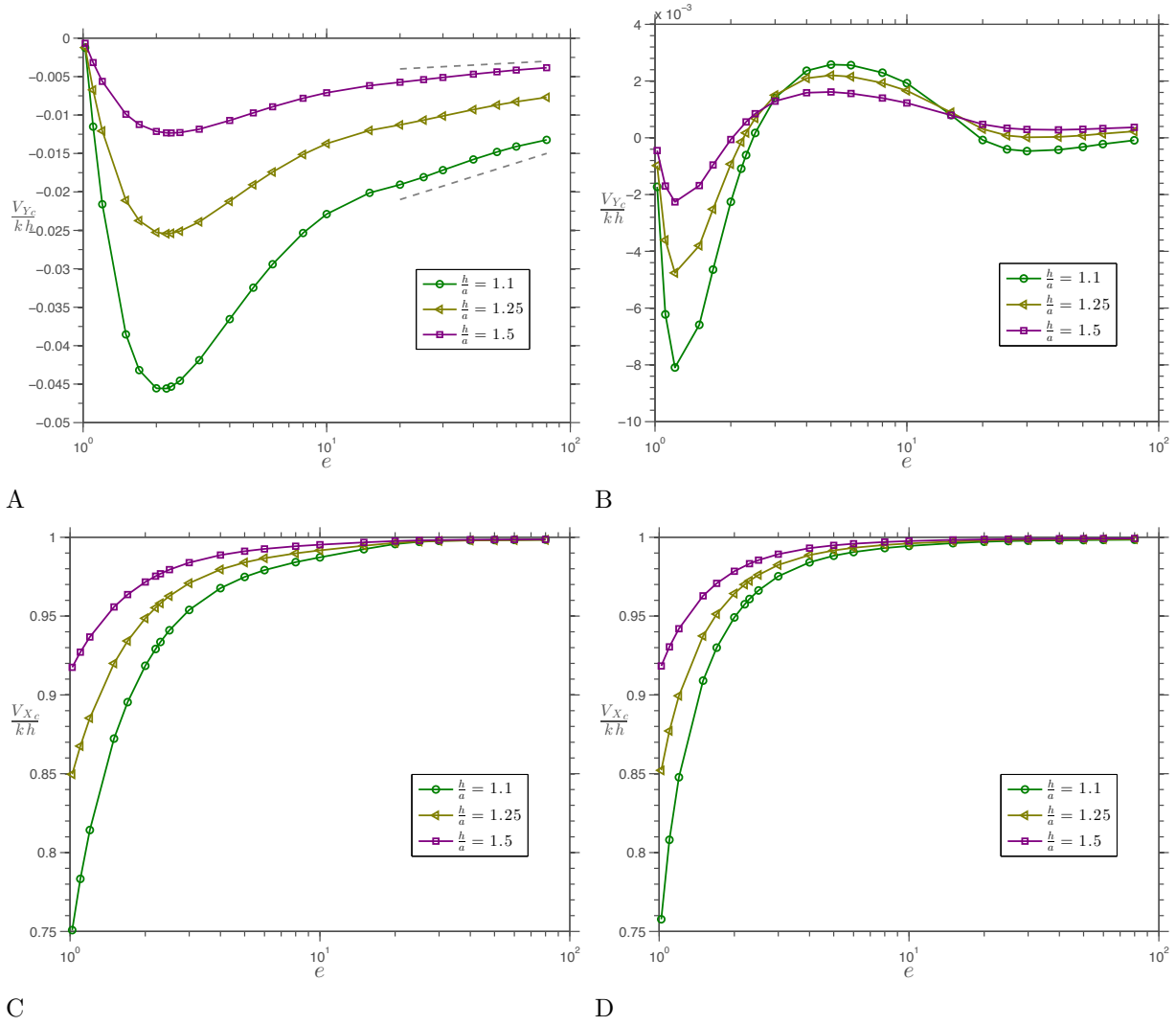

Figure 3-16. Effect of the aspect ratio on the vertical and horizontal velocities for prolate spheroids. The graphs include the lift velocity for **(A)** $\theta = \pi/3$ **(B)** $\theta = \pi/9$ as well as the horizontal component of the velocity for **(C)** $\theta = \pi/3$ and **(D)** $\theta = \pi/9$.

vorticity direction. For the $\phi = 0$ cases with the bounding wall, no such motion is predicted and, in the absence of the wall even when $\phi \neq 0$, the center of the particle does not move in the vorticity direction.

Figure 3-19 shows the corresponding velocities as a function of θ for different azimuthal angles ϕ. The maximum lift is found when the particle is in the plane perpendicular to the vorticity ($\phi = 0$) and the maximum z-component of the velocity is attained for $\theta \approx 0.35$, and $\phi \approx 0.2\pi$. Note that θ never reaches zero if the azimuthal angle is different from zero

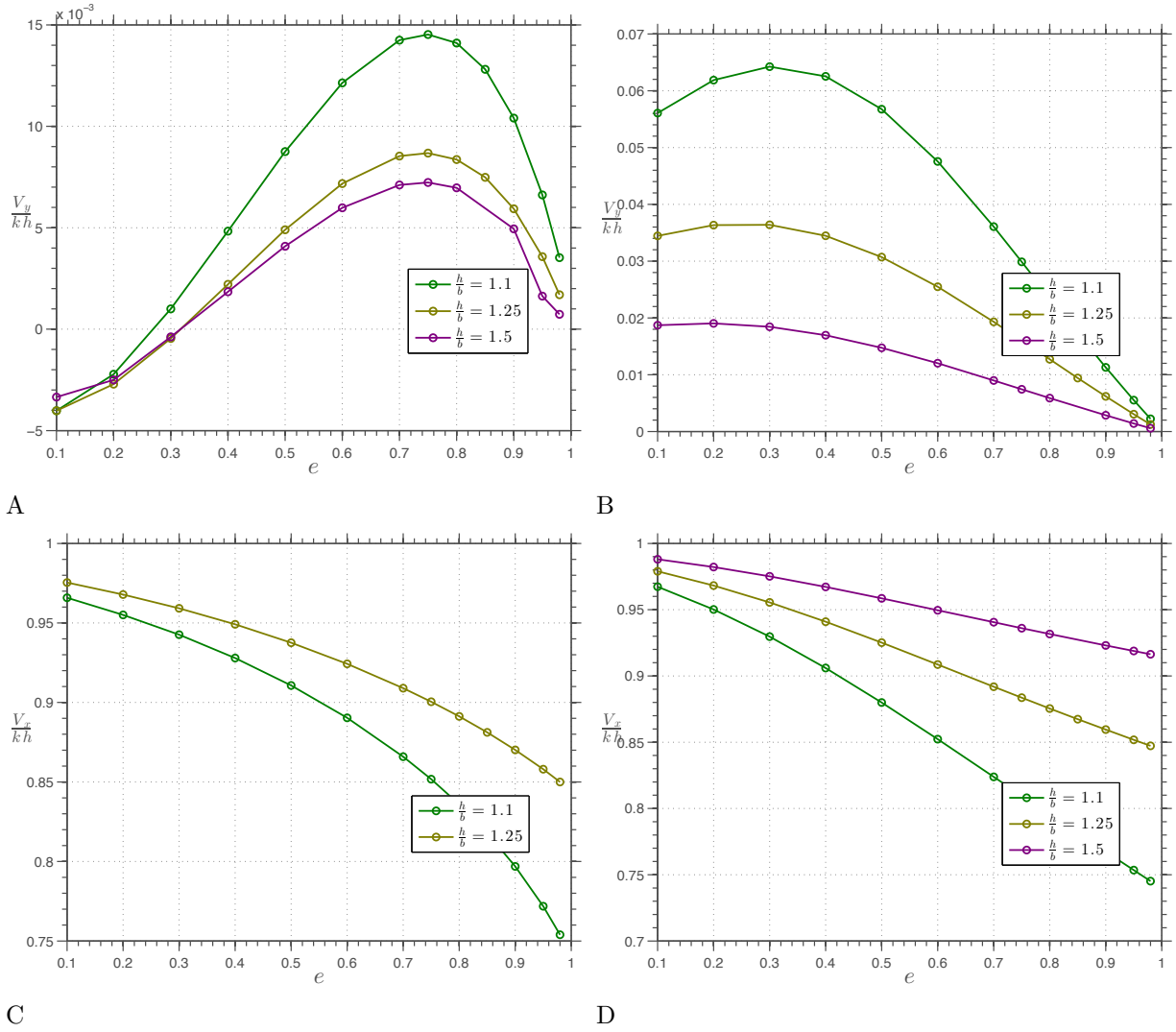

Figure 3-17. Effect of the aspect ratio on the vertical and horizontal velocities for oblate spheroids. The graphs include the lift velocity for **(A)** $\theta \approx \pi/3$ **(B)** $\theta \approx \pi/9$ as well as the horizontal component of the velocity for **(C)** $\theta \approx \pi/3$ and **(D)** $\theta \approx \pi/9$.

(see Fig. 3-19D). This is simply due to the fact that the particle never aligns with the x-axis once a non-zero azimuthal angle is given.

3.6 Summary

To conclude, the trajectories of spheroidal particles in shearing flows have been calculated. The calculations have been done for spheroids translating in an unbounded fluid and in the vicinity of a wall. This was done for a range of aspect ratios and initial positions

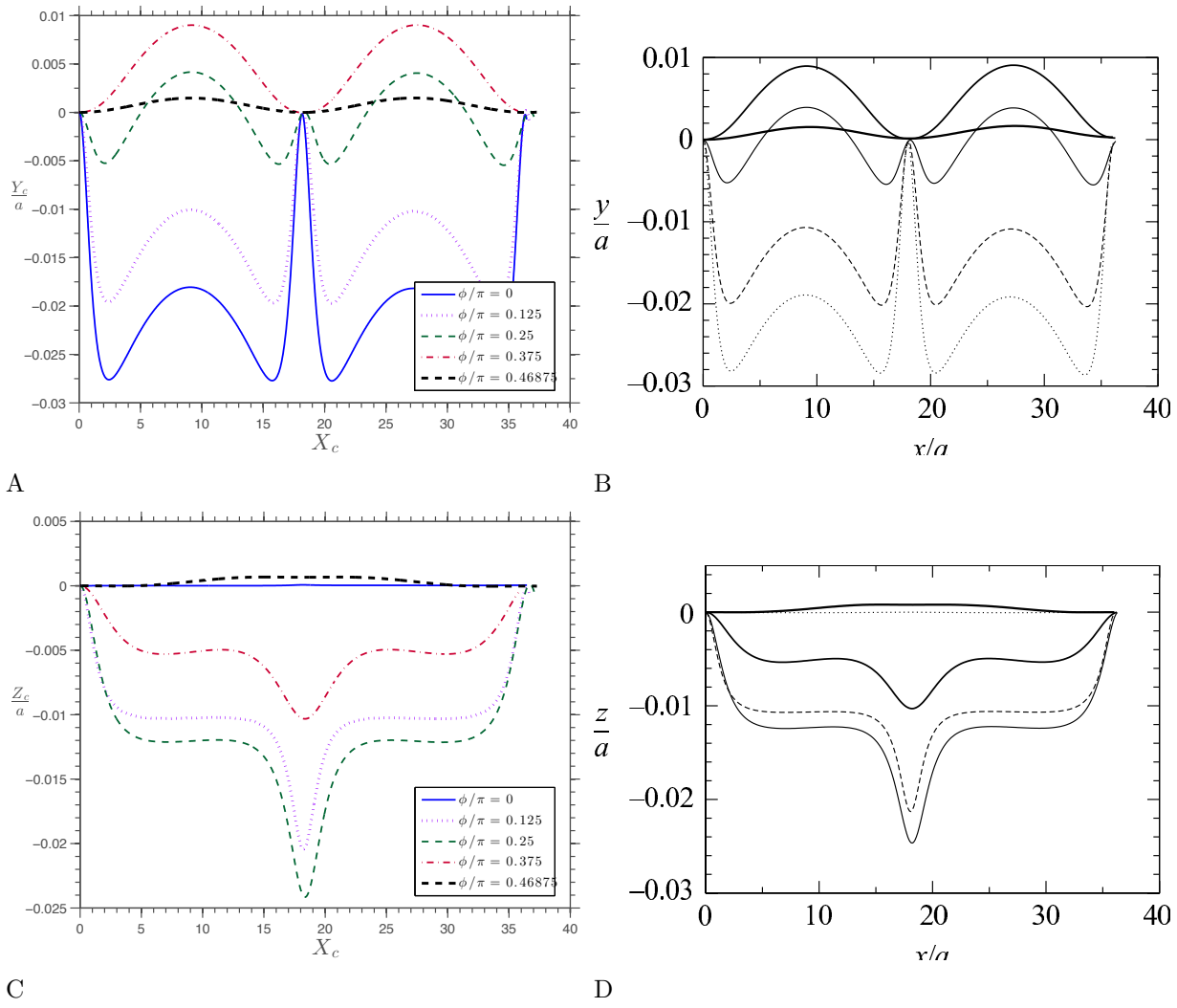

Figure 3-18. Projection of the particle center trajectories for $h/a = 1.25$ for different azimuthal angles ($\phi_0 = 0$ (blue), $\phi_0 = 0.125\pi$ (pink), $\phi_0 = 0.25\pi$ (green), $\phi_0 = 0.375\pi$ (red) and $\phi_0 = 0.46875\pi$ (black)). The particle is a prolate spheroid discretized into 760 elements with aspect ratio $e = 4$. **(A)** Projection in the $x - y$ plane. **(B)** Pozrikidis results [49] for the projection in the $x - y$ plane. **(C)** Projection in the $x - z$ plane. **(D)** Pozrikidis results [49] for the projection in the $x - z$ plane.

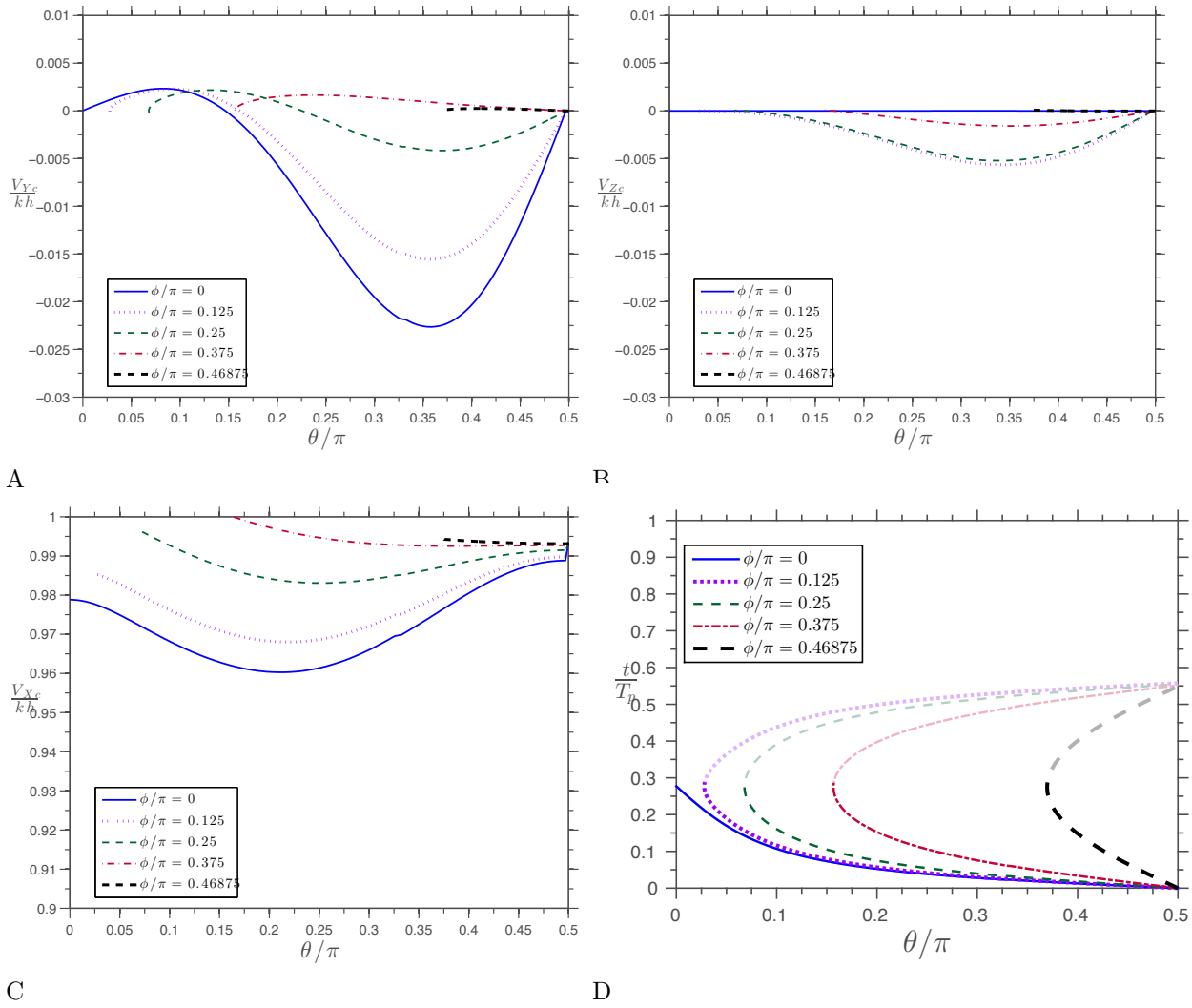

Figure 3-19. Velocity components of the particle's center for $h/a = 1.25$ and for different azimuthal angles ($\phi_0 = 0$ (blue), $\phi_0 = 0.125\pi$ (pink), $\phi_0 = 0.25\pi$ (green), $\phi_0 = 0.375\pi$ (red) and $\phi_0 = 0.46875\pi$ (black)). The particle is a prolate spheroid discretized into 760 elements with aspect ratio $e = 4$. **(A)** Lift velocity V_y along the y axis. **(B)** Velocity V_z along the z axis. **(C)** Horizontal velocity V_x along the x axis. **(D)** Evolution of the rotational orientation with respect to the normalized time t/T_p for different initial azimuthal angles.

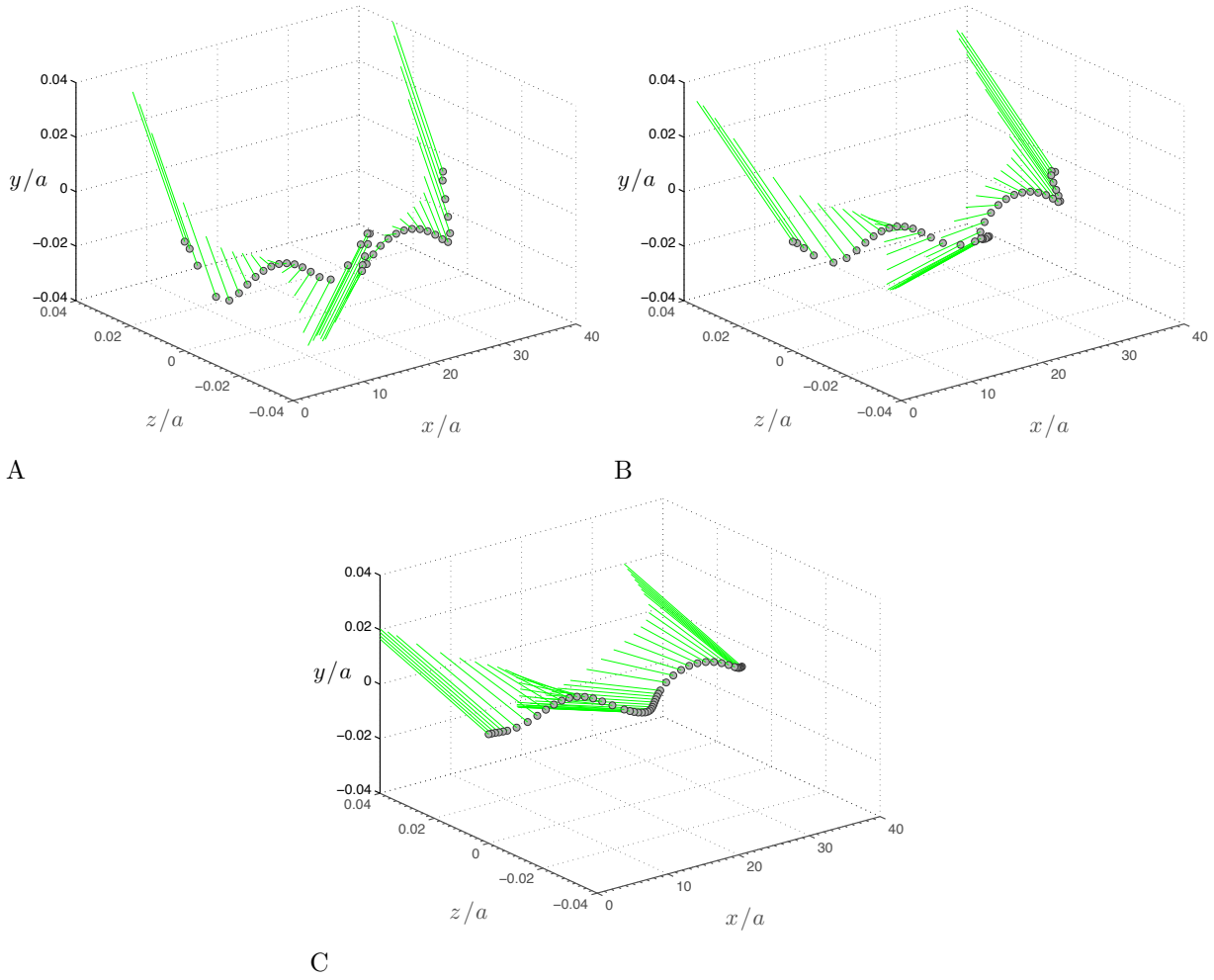

Figure 3-20. Trajectory of a prolate spheroid discretized into 760 elements with aspect ratio $e = 4$. The grey points show the motion of the particles center and the green lines indicate the orientation of the particle. **(A)** The initial azimuthal angle is $\phi_0 = 0.125\pi$. **(B)** The initial azimuthal angle is $\phi_0 = 0.250\pi$. **(C)** The initial azimuthal angle is $\phi_0 = 0.375\pi$.

and orientations with respect to the planar bounding wall and flow direction. It was shown, consistent with previous works, that the addition of the bounding wall can generate components of velocity that are perpendicular to the flow, whereas no such motion exists for the flow of spheroids that are far from any boundaries.

Beyond confirming previous calculations, the work presented here has extended the results to a much wider range of conditions than previously published. By performing results for aspect ratios up to $e = 100$ and comparing with analytical theories, the prediction of a

logarithmic approach of the lift velocity to zero with increasing aspect ratio was confirmed. Also, it was found that the maximum possible lift velocity exists for particles that are oblate, with an aspect ratio of approximately 3/4. This latter result is potentially useful in not only interpreting measurements of particle flow, but also designing particle shapes that will either minimize or maximize particle-surface collisions. The long-term goal, yet to be realized, of these calculations is to couple them with models of fluid flow in the presence of interfacial phenomena to examine the effectiveness of novel methods for cleaning surface.

CHAPTER 4
EFFECT OF THE DRYING CONDITIONS ON THE MICROORGANISMS DETACHMENT

In the Chapter 2, we investigated the detachment of powder microparticles. However, in various environments, including that of food processing, adherent microorganisms are initially on a liquid phase then they are subjected to drying conditions. In this Chapter[1] , we investigated the consequences of a drying step on the further ability of adherent bacterial spores to resist detachment. An initial series of experiment was set up with latex microspheres as a model. A microsphere suspension was deposited on a glass slide and incubated at 25, 35 and 50°C for times ranging from 1 h to 48 h. By subjecting the dried slides to increasing water flow rates, we showed that both time and temperature affected the ease of microsphere detachment. Similar observations were made for three Bacillus spores despite differences in their surface properties, especially regarding their surface physicochemistry. The differences in ease of adherent spore detachment could not be clearly linked to the minor changes in spore morphology, observed after drying in various environmental conditions. In order to explain the increased interaction between spheres or spores and glass slides, several assumptions regarding the possible underlying mechanisms were made: the shape of the liquid bridge between the sphere and the substratum, which is greatly influenced by the hydrophilic/hydrophobic characters of both surfaces; the accumulation of soil at the liquid/air interface; the presence of trapped nano-bubbles around and/or under the sphere.

4.1 Biological Background

Pathogenic bacteria are commonly found to be associated with equipment surfaces in various industrial environments, including the agro-food sector where they are considered a major source of food contaminants, entailing both economic and health consequences.

[1] Reprinted with permission from C. Faille, I.Bihi, A. Ronse, M. Baudoin, and F. Zoueshtiagh, Increased resistance to detachment of adherent microspheres and Bacillus spores subjected to a drying step, Colloids and Surfaces B: Biointerfaces **143**, 293-300 (2016)

According to Haeghebaert et al. [3], equipment contamination would have been behind around 40% of food poisoning in France between 1996 and 1998. More recently, according to the French Institute for Public Health Surveillance, 62% of food infections in collective catering are induced by contamination of equipment surfaces. Similar observations have been made in homes, where kitchen surfaces are frequently contaminated [84–86]. Indeed, despite cleaning and disinfection procedures, some bacteria are still commonly found on the surfaces of food processing lines, mostly in the form of adherent spores, e.g. Bacillus spores in closed equipment [87, 88] or in the form of biofilms, e.g. those partially composed of Pseudomonas spp. [89, 90].

It has been shown that bacterial resistance to detachment is strongly affected by the surface properties of bacteria. In the case of *Bacillus cereus* spores for example, various works have described the role played by their hydrophobic nature [91–93], the presence of appendages [94] and the spore size [95]. The role of substratum properties has also been extensively investigated [96, 97]. Conversely, the influence of conditions encountered by adherent bacteria between the contamination phase and the hygiene procedure, during which surface drying could occur, has been poorly investigated. However, many bacteria are able to withstand periods of desiccation, whether in the form of biofilms [98], or that of adherent cells [85] and spores [99]. Moreover, given the great variability of food contact surfaces, including utensils, cutting boards or closed equipment, adherent bacteria face a wide variety of environments and temperatures. One may rightfully wonder whether this drying phase might significantly influence the further resistance of bacteria to detachment. The few works relating to the drying of adherent micro-organisms for extensive periods have mainly focused on cross-contamination between foods and surfaces [85, 100, 101].

Bacillus spores are of concern to the food industry as they are readily isolated from foods [102, 103], highly resistant to heat treatment and disinfection procedures [104], and often associated with food-borne diseases [105]. Moreover, Bacillus spores, particularly spores from strains belonging to the *B. cereus* group, firmly adhere to a wide variety of inert surfaces,

such as those found on food processing premises [92, 106]. Their resistance to cleaning procedures has been also reported [95, 107]. The ability of Bacillus spores to adhere and to resist cleaning procedures is affected by both surface morphology and physico-chemistry, such as spore hydrophobicity [91, 93], the presence of appendages or the size of the spores [93].

This study was designed to evaluate the influence of conditions encountered before the detachment of adherent spores (time and temperature of the drying phase) on their further ease of removal from the contaminated surfaces. As the spore surface properties are possibly affected by the conditions encountered during the drying step, which in turn might lead to changes in the interaction forces between spores and substrata, both Bacillus spores and latex microspheres were used as models. In order to investigate the underlying mechanisms, some additional experiments were performed to monitor the dynamics during drying of the liquid bridge at the interface between a sphere and the substratum, on which the sphere was placed.

4.2 Material and Methods

4.2.1 Bacillus Spores and Microspheres

B. cereus 98/4 (highly hydrophobic, medium-sized spores), *Bacillus subtilis* 98/7 (hydrophilic, medium-sized spores), and *Bacillus pumilus* 98/6 (hydrophobic, small spores) were used in this study. Spores were produced at 30 °C on Spo8-agar consisting of 8 g liter^{-1} nutrient broth (Biokar Diagnostics, Beauvais, France), 0.51 g liter^{-1} $MgSO_4.7H_2O$, 0.97 g liter^{-1} KCl, 0.2 g liter^{-1} $CaCl_2.2H_2O$, 3×10^{-3} g liter^{-1} $MnCl_2.4H_2O$, 0.55×10^{-3} g liter^{-1} $FeSO_4.7H_2O$, and 1.5% agar. When over 95% of spores were obtained, they were harvested by scraping the surface, washed five times in chilled sterile water (by centrifugation at 1500 g for 15 min except for *B. subtilis* spores centrifuged at 3500 g for 15 min), and stored in sterile water at 4 °C until use [6]. Before each experiment, two further washes were performed and spores were subjected to a 2.5-min ultrasonication step in an ultrasonic cleaner (Bransonic 2510E-MT, 42 kHz, 100 W, Branson Ultrasonics Corpo- ration, USA) to

limit the presence of aggregates. Other experiments were performed with fluorescent latex microspheres, moderately hydrophobic, of 0.2μm, 0.5 μm, 1 μm and 6 μm in diameter, which were washed twice in sterile water (Polybeads Dyed Yellow Microspheres, Polysciences Inc.).

4.2.2 Influence of Drying Conditions on Spore/Microsphere Size and Morphology

Spores and microspheres deposited on glass slides were observed by scanning electron microscopy (SEM) after 2 h at 25° C and after 48h at 50°C, after coating with goldpalladium for 1.5 min. Sample observations were performed through a Hitachi S3000 N SEM (Hitachi, Tokyo, Japan) operating at 15 kV. The spore length and width were measured on at least 70 individual spores and the microsphere diameter obtained by measuring over 40 individual beads.

4.2.3 Spores and Microspheres Adhesion and Detachment

Hydrophilic (water contact angle, $\theta = 11°$) glass coupons (Superfrost , ThermoScientific, 70 mm x 65 mm) were used in this study. These coupons were fouled by 150 μL of a spore or micro- sphere suspension. The suspension volume was spread onto the coupon surface so that it covered the area analysed during the detachment step. The coupons were then dried at 25°C, 35°C or 50°C for between 1h and 24h (Bacillus spores) or 48h (micro- spheres). The concentration of the spore/microsphere suspension was chosen to allow the adhesion of several hundred spores per microscope field.

In order to monitor adherent spores/microspheres resistance to detachment, the contaminated coupons were inserted into a parallel-plate flow chamber with a rectangular flow channel (60 mm length by 4 mm width and 0.5 mm height), specially designed to withstand very high flow rates (see Fig. 4-1) [6]. The flow channel was covered with a glass coverslip to allow the direct observation of spore/microsphere detachment under an optical microscope (Axioscop 2 plus, Zeiss). Observations were performed at a magnification of 400. Images were recorded by camera (Olympus, DP21).

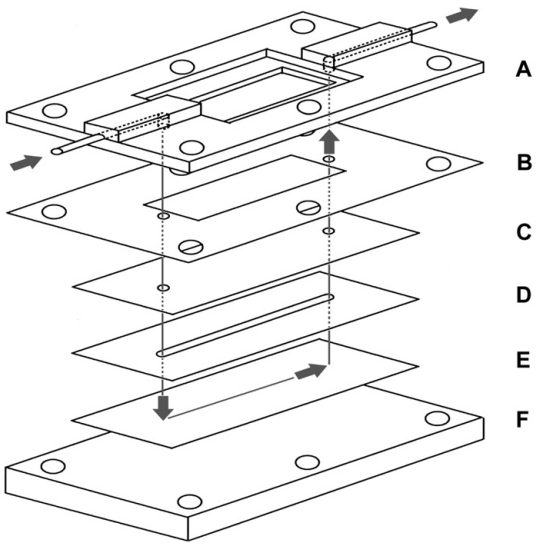

Figure 4-1. Shematic of the flow cell. A: upper part with the inlet and outlet for fluids, B: nitrile gasket, C: glass coverslip, D: flow chennel in a nitrile gasket, E: test material, F: basis of the flow cell. Arrows indicate the direction of flow.

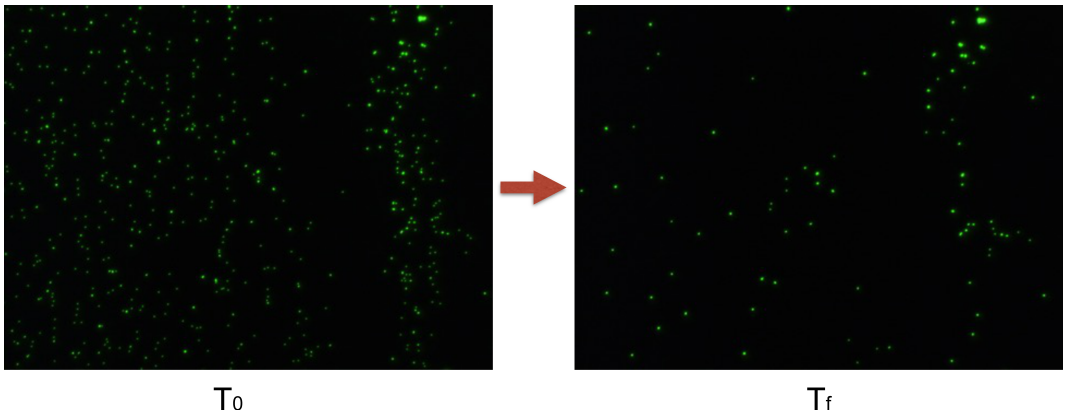

Figure 4-2. Detachment of deposited microparticles using a shear flow. Dark field is the substrate covered with latex microparticles (green). The left image shows a surface before the microparticles detachment (T_0). The right image shows the same surface after the microparticles detachment(T_f).

The contaminated coupons were subjected to 30-second steps of increasing flow rates of deionised water at room temperature. Images were acquired at T_0 and at the end of each detachment step T_f (see Fig. 4-2). The number of adherent spores before and after the rinsing step was measured, and the percentage of residual spores after rinsing was calculated (at least four replicates).

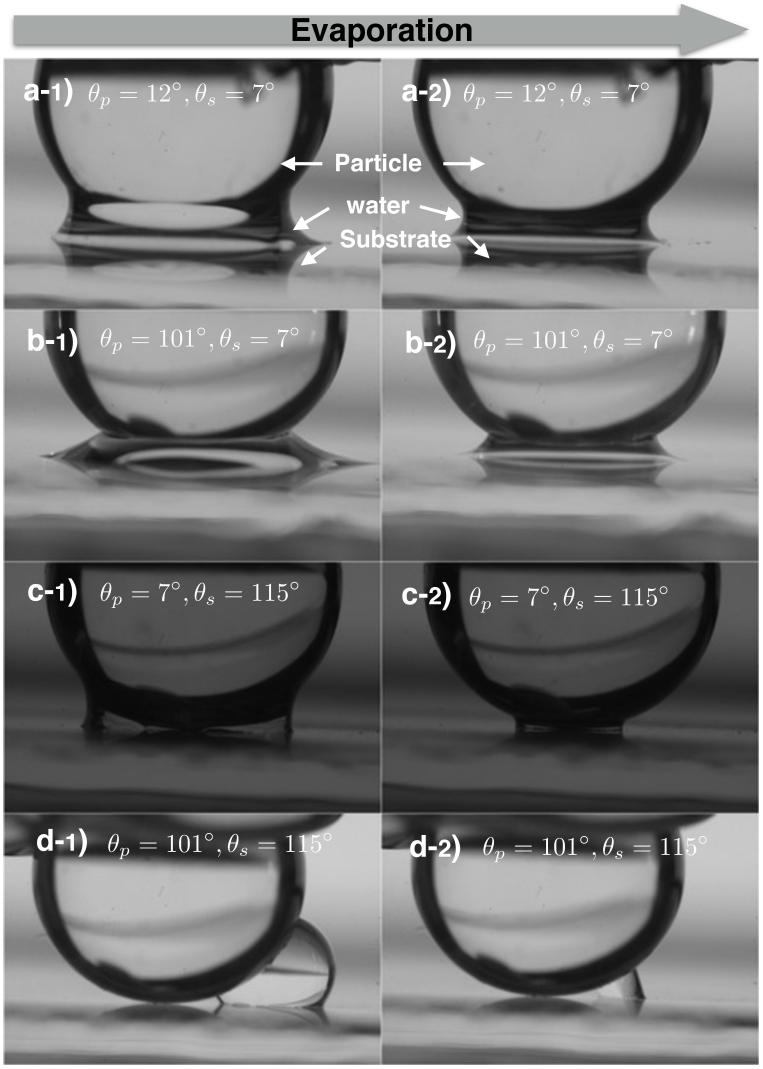

Figure 4-3. Shape of a liquid bridge between a 6 mm-sphere and a substratum with different wetting properties.θ_p is the water-particle contact angle. θ_s is the water-substratum contact angle

4.2.4 Influence of Hydrophobic/philic Properties on the Liquid Interface Around a Particle

In order to show the role played by the hydrophilic/hydrophobic property of surfaces in contact, on the liquid organisation, a sphere was positioned on a water droplet, deposited on a microscope slide and the shape of the liquid bridge made recorded with a CMOS- EOS 40D Canon camera (Fig. 4-3). Both sphere and slide surfaces were chemically-treated to be either hydrophilic ($\theta = 10°$) or hydrophobic ($\theta > 100°$).

Table 4-1. Influence of drying conditions on the size of the adherent Bacillus spores and microspheres

		Spore length (μm)		Spore width or microsphere diameter (μm)	
		2h-25°C	48h-50°C	2h-25°C	48h-50°C
B. cereus 98/4	Average value	1.64	1.74	0.80	0.82
	(Standard deviation)	(0.24)	(0.19)	(0.24)	(0.04)
B. subtilis 98/7	Average value	1.49	1.55	0.75	0.75
	(Standard deviation)	(0.12)	(0.09)	(0.05)	(0.05)
B. pumilus 98/6	Average value	1.12	1.14	0.62	0.60
	(Standard deviation)	(0.08)	(0.10)	(0.03)	(0.03)
Microspheres 6μm	Average value	-	-	6.26	6.37
	(Standard deviation)	-	-	(0.03)	(0.04)

4.2.5 Analysis of Data and Statistical Analysis

Data were analysed by general linear model procedures using SAS V8.0 software (SAS Institute, Gary, NC, USA). Variance analysis was performed first to determine the role of temperature and time on the ease of removal 1) of adherent latex microspheres, 2) of adherent Bacillus spores. These analyses were followed by multiple comparison procedures using Tukeys test (Alpha level = 0.05).

4.3 Results

4.3.1 Spore/Microsphere Size and Morphology

We first investigated whether the drying conditions would affect spore/microsphere size and morphology. For this purpose, spores and microspheres were rapidly observed under scanning electron microscopy without any dehydration steps in order to limit further changes in size (Fig. 4-4, middle and right-hand columns). As shown in Table 4-1, the length and width of the Bacillus spores were hardly affected by the drying conditions: the observed differences between drying conditions generally being below 2%. The length of *B. cereus* 98/4 spores was the only parameter which seemed to be affected by the temperature and/or time of the drying step, but astonishingly, spores were somewhat longer (about 7%) but not wider at high drying temperature. Concerning the microspheres (average values and standard deviations obtained from ±40 microspheres), similar diameter values were obtained after both drying procedures.

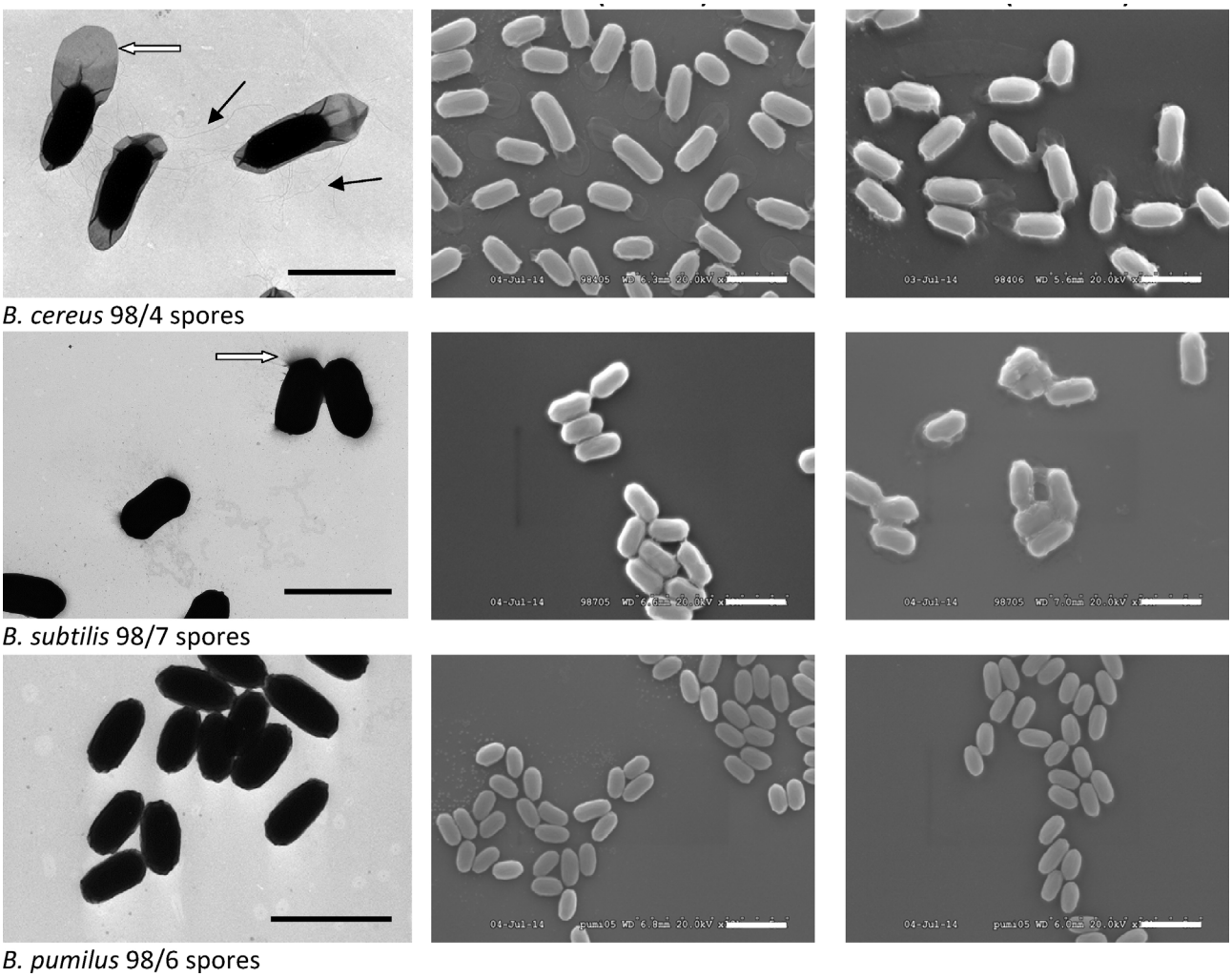

Figure 4-4. Left column: transmission electron microscopy of Bacillus spores after negative staining. B. cereus 98/4 are surrounded by an exosporium (white arrow) and with appendages (black arrows), B. subtilis 98/7 spores are surrounded with a mucous layer (white arrow), and the surface of B. pumilus 98/6 spores are devoid of any additional layer/material. Middle and right-hand columns: scanning electron microscopy of the same spores (Scale bars = 2 μm)

We also investigated whether spore surface could be affected by the different drying conditions. As observed through transmission electron microscopy (TEM, Fig. 4-4, left column), *B. cereus* 98/4 spores are surrounded by an outermost membrane called exosporium (white arrow) and with numerous appendages of 10 nm in width (black arrows). After drying (Fig. 4-4, middle and right-hand columns), *B. cereus* 98/4 spores exhibited an intact exosporium even after 48 h at 50°C. *B. subtilis* 98/7 spores, which are surrounded by a more

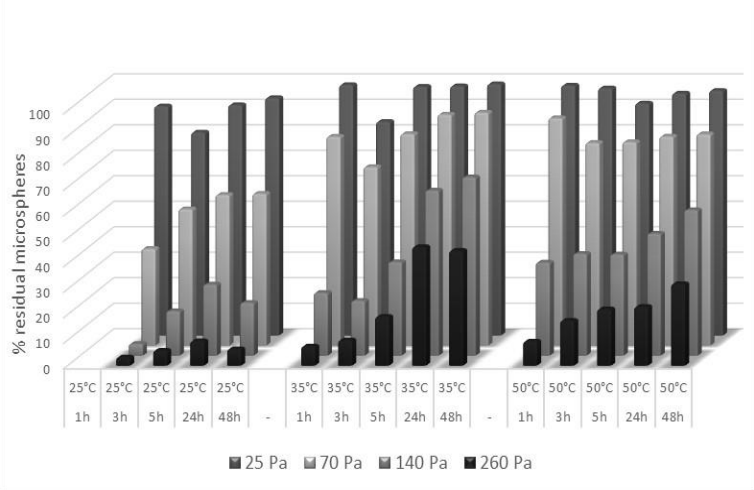

Figure 4-5. Residual ratio of 6 μm microspheres after detachment under a range of shear stresses and subjected to various drying conditions

or less regular mucous layer (left column, white arrow), also seemed only slightly affected by the drying conditions, the surface being less regular at 50°C than at 25°C. Lastly, the surface of *B. pumilus* 98/6 spores, which are devoid of any additional layer/material, as well as the 6 μm microspheres (data not shown) seemed relatively unaffected by the environmental conditions during the drying step.

4.3.2 Microsphere Resistance to Detachment

Experiments in the parallel-plate flow chamber were performed at mean wall shear stresses of 25 Pa, 70 Pa, 140 Pa, and 260 Pa. As shown in Figure 4-5, a very limited microspheres detachment occurred at 25 Pa, even when contaminated coupons were kept at $25°C$. At higher shear stresses, the detachment increased and the resistance of the 6 μm microspheres was deeply affected by the environmental conditions. When the microspheres were maintained at 25°C, over 90% were detached at a shear stress of 260 Pa. At higher temperatures, the number of residual microspheres increased.

Variance analyses were performed to investigate the role of drying time and temperature on the microsphere detachment at 20 Pa (data not shown) and 260 Pa. As expected, temperature and time significantly affected the resistance of microsphere to high wall shear stresses (p value< 0.0001) but not to lower hear stress (p value$= 0.1877$). For example, the

Table 4-2. Influence of drying conditions (temperature and time) on the percentage of residual adherent microspheres (mean value) after detachment at a shear stress of 260Pa.

Temperature	Percentage of residual adherent microspheres	Tukey Grouping	Time	Percentage of residual adherent microspheres	Tukey Grouping
25°C	6.4	B	1h	9.7	C
35°C	25.3	A	3h	10.8	B C
50°C	21.0	A	5h	16.8	A B C
-	-		24h	25.7	A B
-	-		48h	27.6	A

parameters jointly accounted for 67% of the whole variability observed at 260 Pa. Tukeys grouping (Table 4-2) showed that the percentages of residual microspheres after the rinsing step at 260 Pa, was lower when soiled coupons were kept at 25 °C (Group B) than at 35°C or 50°C (Group A). Concerning the duration of the drying period, detachment of adherent microspheres was the easiest after only 1 h (Group C) and the most difficult after 48 h (Group A).

In order to investigate any impact of the size of the objects on the ease of removal, further experiments were performed with microspheres of different diameters (0.2 μm, 0.5 μm, 1 μm, 3 μm, 6 μm) dried for 1 h at 35°C. The following wall shear stresses used for this set of experiments were 17Pa, 60Pa, 130Pa, 191Pa and 360 Pa. The diameter of the adherent microspheres were found to strongly impact their resistance to flow (Fig. 4-6). Whatever the shear stress, less than 5% detachment was observed for the smallest microspheres (0.2 μm and 0.5 μm diameter). Conversely, the largest microspheres could be removed from the glass coupons and the level of residual spheres decreased with the diameter. For example, after 30 s at 191 Pa, only 10% of the 6 μm microspheres were still counted on the surface, compared to 47% of the 1 μm microspheres.

4.3.3 Spore Resistance to Detachment

Further experiments were performed with Bacillus spores at mean wall shear stresses of 25 Pa to 447 Pa (Table 4-3). Whatever the strain in use, spore resistance to flow was significantly higher than that of microspheres. Indeed, at the highest flow velocity used in these experiments (447 Pa vs 260 Pa for the microspheres), over 40% of the adherent spores

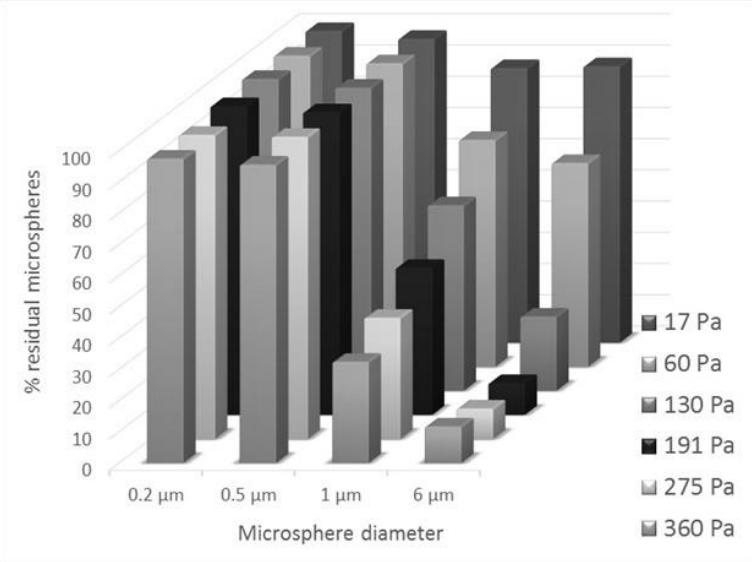

Figure 4-6. Residual ratio of different size microspheres after detachment under a range of shear stresses

resisted detachment when drying occurred at 35°C or 50°C. Even in the mildest conditions (3 h at 25°C), between 14 and 61% of the spores were still counted after the detachment step. Furthermore, differences were observed between strains, primarily at 25°C but also to a lesser extent in the other drying conditions. When dried at 25°C, *B. cereus* 98/4 spores were the most resistant to detachment, while *B. pumilus* were the most resistant after 1 h and 3 h at 35°C and 50°C. Conversely, *B. subtilis* 98/7 spores were relatively easily removed from the surface whatever the drying conditions. Taking into account the data obtained at 447 Pa for the three strains, the three parameters: strain, time and temperature of drying significantly affected the resistance of spores to detachment (p-values < 0.0001), while the trial did not. Tukeys grouping (Table 4-4) confirmed that: firstly, the three strains had different adhesive behaviors (or responses to drying); secondly, incubation at 35°C and 50°C resulted in a stronger interaction between spores and substratum than observed at 25°C; thirdly, longer incubation resulted in stronger interaction forces.

4.4 Discussion

In previous studies on Bacillus spore detachment during cleaning-in-place (CIP) procedures, the data analysis sometimes revealed a wide variability of the percentage of spores resistant

Table 4-3. Percentage of residual adherent *Bacillus* spores subjected to various drying conditions (time and temperature). Detachment was performed under a range of shear stresses ranging from 25 to 447 Pa

	Drying conditions		Shear stress (Pa)				
	Time	T°	25	70	140	260	447
*B. cereus*98/4	3h	25°C	99	94	86	76	61
	5h		98	95	90	81	71
	24h		100	100	99	97	95
	1h	35°C	100	96	82	61	46
	3h		99	96	90	80	62
	5h		100	99	96	92	87
	24h		100	100	100	99	99
	1h	50°C	99	98	94	87	79
	3h		100	99	97	94	88
	5h		100	99	99	98	96
	24h		100	99	99	98	96
B.subtilis 98/7	3h	25°C	78	67	58	48	32
	5h		51	46	43	38	33
	24h		80	77	74	68	59
	1h	35°C	95	90	87	74	56
	3h		94	91	87	82	73
	5h		98	94	91	86	79
	24h		88	77	72	68	62
	1h	50°C	86	72	68	64	58
	3h		95	88	85	79	73
	5h		97	93	90	88	83
	24h		94	89	87	84	82
B.pumilus 98/6	3h	25°C	86	69	46	26	14
	5h		95	90	86	76	70
	24h		86	72	64	56	52
	1h	35°C	97	93	91	89	86
	3h		97	95	91	87	82
	5h		96	91	85	81	78
	24h		100	99	99	98	97
	1h	50°C	98	95	93	90	86
	3h		98	97	94	90	88
	5h		99	98	95	93	91
	24h		100	99	98	96	91

Table 4-4. Influence of drying conditions (temperature and time) and bacterial strain on the percentage of residual adherent spores after a detachment step at 447 Pa

Strain	% of residual spores	Tukey Grouping	Temperature	% of residual spores	Tukey Grouping	Time	% of residual spores	Tukey Grouping
*B.cereus*98/4	84.9	A	25°C	56.7	B	1h	71.8	AB
*B.pumilus*98/6	74.5	B	35°C	78.8	A	3h	61.6	B
*B.subtilis*98/7	61.1	C	50°C	84.1	A	5h	75.0	A
-	-		-	-		24h	80.7	A
-	-		-	-		48h	78.8	A

to a CIP or a rinsing procedure [6]. Beside the various factors known to play a role on spore detachment (spore morphology, material and spore surface physicochemistry), we hypothesized that the time between the contamination step and the detachment procedure could play a significant role on the ease to remove adherent spores from contaminated surfaces. If that is the case, this parameter could play a key role in the efficacy of the hygiene procedures in real environments, e.g. in the food industry, where very different environmental conditions could be found. For example, bacteria are repeatedly isolated from many surfaces, such as closed (inner surfaces of pipes, valves, pumps) or open surfaces (cutting board, conveyor belts, floors, walls), in more or less humid environments and at various temperatures (cold rooms, cheese ripening facilities, processing lines). Consequently, the soil properties would differently change over time depending on the contaminated area: for example, adherent bacteria on splashing areas will be subjected to a rapid desiccation phenomenon contrarily to bacteria located on the low points of pipes or pieces of equipment. However, this drying step have been the subject of only very few studies except on its consequence on the bacteria transfer from contaminated surfaces to food in contact. For example, Rodriguez and his colleagues showed on L. monocytogenes biofilms that the transfer rate from contaminated surfaces to food decreased with drying [108, 109]. They have postulate that the cell-surface adhesion was weakened during drying. But it can be also assumed that cell-cell interactions, rather than cell-substratum interactions, were changed following drying. Other reported experiments were performed on bacterial cells directly deposited on surfaces. The same authors [108] failed to produce any evidence of the influence of a 1 h-drying step at $37°C$ on the transfer rate of L. monocytogenes cells from stainless steel to foods. Conflicting results have been reported with Salmonella and Escherichia coli cells, which transfer rates from different materials to vegetables were often lowered following drying [18]. An important point to note here is that, along with the presence of a residual film of water on surfaces, desiccation could also deeply affect bacterial metabolism and surface properties that, in turn, alter the interaction between bacteria and materials [110].

Therefore, in order to limit the possible influence of cell modifications on the interactions between cells and materials, we decided to set up a series of experiments with latex microspheres, shown to be poorly affected by the various drying conditions. Microspheres were simply spread onto the glass surfaces and dried without any washing step, which would have removed loosely bound elements. This approach would mimic what happens on splashing areas, where bacteria are forced to adhere, water being removed by evaporation. As suggested by Rodriguez and McLandsborough [108], this procedure would favor hydrophobic interaction between bacteria and the bacterial and the solid surfaces. The first set experiments was performed with microspheres of 6 μm diameter, which were subjected to a range of temperature for different times and analysed for their ease of removal from glass coupons (shear stresses ranging from 25 Pa to 260 Pa). The microspheres first exhibited a relatively high flow resistance. Indeed, at the lowest shear stress almost no detachment occurred and remaining microspheres were still observed after 30 s at 260 Pa. High resistance of adherent objects to water rinsing has been previously reported in the literature. For example, the percentage of Saccharomyces yeasts removed from stainless steel was negligible under the threshold value of 15 Pa above which the yeast detachment increased with the wall shear stress to reach 80% at 100 Pa [111]. According to other authors, the resistance to mechanical detachment was even more strikingly low with only 10 of yeasts detached at 80 Pa [112]. Concerning the influence of the time and temperature of drying, both parameters clearly affected the subsequent ease of removal of adherent microspheres. In general, percentage of residual microspheres after rinsing increased with the drying time. The temperature also affected interactions between microspheres and glass, but the observed differences were only significant between $25°C$ and $35°C$.

Microsphere properties being relatively impervious to the drying conditions used in this study, it can be assumed that interactions between microspheres and surfaces would be influenced by the amount of surrounding water, which decreases through evaporation. Along with the amount of residual liquid at the interface, the hydrophobicity of both particle and

substratum surfaces may further affect interaction forces. Indeed, the shape taken by a liquid bridge between a sphere and a substrate differs greatly with the surface properties (Fig. 4-3).

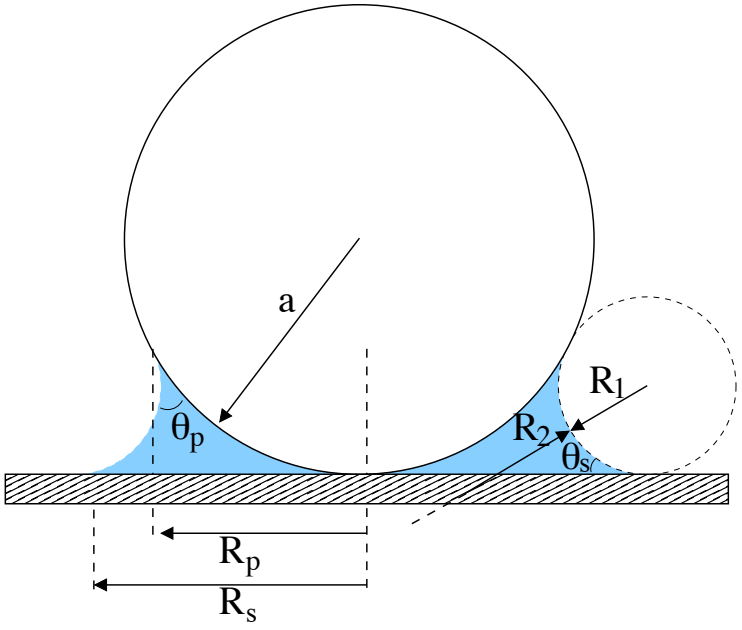

Figure 4-7. Notation of a liquid bridge between a sphere and a substrate.

As a consequence the pressure inside the bridge can highly vary leading to either attraction or repulsion between the solid bodies. Depending on the interface curvature, the difference of pressure between inside and outside the liquid bridge is evaluated using the Young-Laplace equation

$$P_{inside} - P_{outside} = \Delta P = \gamma(\frac{1}{R_1} + \frac{1}{R_2}) \tag{4–1}$$

where γ is the liquid's surface tension, R_1 and R_2 are the principal radii of the liquid interface curvature (Fig. 4-7). This difference of pressure is therefore affecting the type of force felt by the particle (attraction or repulsion to the substrate). The vertical capillary force is the sum of two terms: the axial component of surface tension force at the solid-liquid-gas interface (wetting force), and the force due to the hydrostatic pressure in the bridge itself (Laplace force). The total force over the sphere particle can be approximately calculated by:

$$F_{sph} = -2\pi R_p \gamma \sin(\theta_p) - \pi R_p^2 \Delta P \tag{4–2}$$

where θ_p is the particle contact angle and R_p the radius of the pendular ring over the sphere. For the capillary force acting on the substrate:

$$F_{sub} = 2\pi R_p \gamma \sin(\theta_s) - \pi R_p^2 \Delta P \tag{4–3}$$

The evaporation of the bridge changes the bridge radii and the reduced hydrostatic pressure leading to different force intensity on time.

Another phenomenon suspected of influencing interactions during the drying process, is that the triple contact line that determines the frontier between gas, solid and liquid may accumulate soils or submicron particles (e.g. food residues) on wetting surfaces. This may give rise to the formation of commonly called coffee stains [113]. Indeed, depending on the evaporation rate, nanoparticles can accumulate on liquid-drying areas [114]. The accumulation of these submicron particles near and around a spore can greatly contribute to changes in the interaction force. Fig. 4-8 highlights this effect at the contact point between a 6 mm-diameter sphere and a microscope slide. After the evaporation of a deionized-water bridge, the accumulation of soil trapped by the liquid bridge is clearly observed. The position of these accumulated submicron particles would also strongly depend on the wetting characteristics of both the particle and the substratum.

Lastly, we believe that, as observed on hydrophobic surfaces [115], nano or micro bubbles may form around (or under) dried hydrophobic spheres or spores when they are wetted. The presence of such trapped bubbles may greatly increase the required detachment force, since the spore contact point with the substrate may then consist of multiple liquid bridges. The effect of the surrounding environment on the adhesion force is currently being investigated.

We then investigated the behaviour of Bacillus spores, which are very stable in response to various environments. Previous works have shown that drying could result in significant changes in the Bacillus spore morphology. The dimension of the Bacillus athrophaeus spores, for example, significantly decreased with air-drying (by around 12%) and concomitant modifications of the spore coat morphology were clearly observed by atomic force microscopy

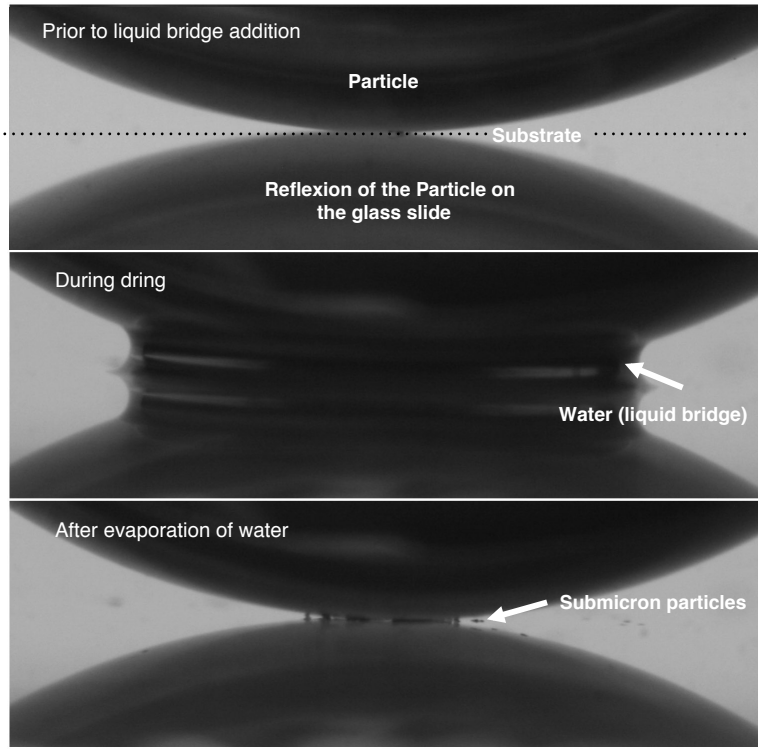

Figure 4-8. Photos of the contact point between a 6 mm-diameter sphere and a glass slide, **(A)**before adding a liquid bridge, **(B)** in the presence of a liquid bridge, **(C)** after the evaporation of the liquid bridge.

(AFM) [116]. Other observations indicated that spores of *Bacillus thuringiensis* would swell or shrink in response to a change in relative humidity [117]. In this study, we noted only minor changes in the spore size following the various drying procedures. It is unlikely that these changes would account for the significant changes observed in the spore resistance to detachment. We also examined whether the spore surface features were affected by the drying step. Indeed, spores from strains belonging to various Bacillus species are surrounded by different external layers and sometimes by appendages. *B. subtilis* spores, surrounded by a mucous layer and *B. pumilus* spores, devoid of any surface features [93] were only slightly if not at all affected, by the drying conditions. *B. cereus* 98/4 spores are surrounded by a balloon-like layer called an exosporium, which is loosely bound to the underlying spore. In liquid environments, fluid is adsorbed through the exosporium, which becomes swollen as shown on spore sections of fully-hydrated spores observed by TEM [93, 118]. Conversely, the

exosporia of air-dried spores collapse (Fig. 4-4), thereby increasing the exchange surface area between spores and substratum. However, this collapse was observed whatever the drying condition (data not shown) and therefore could not be connected to changes in interface phenomena.

These spores were then subjected to increasing shear stresses in the parallel-plate flow chamber. The phenomena observed were similar to those of microspheres in that their resistance to detachment increased with temperature and drying time, although spores proved significantly more resistant to removal. Almost no detachment occurred at higher temperatures and longer times, yet clear differences exist between strains. Indeed, *B. subtilis* spores are much less resistant to removal than the other two strains. Such differences could be accounted for by the different hydrophilic/hydrophobic character of the three spores. To characterize the hydrophobic properties of the different micro-organisms, the partitioning method was used [6, 93, 119]. This method is based on the affinity of the microspheres/spores to an appolar solvent, hexadecane (Sigma). Thus, it has been shown that *B. cereus* 98/4 spores were highly hydrophobic, *B. subtilis* spores highly hydrophilic and *B. pumilus* spores having intermediate properties. However, the 6 μm-microspheres are moderately hydrophobic and their ease of removal was even more marked than that of *B. subtilis* spores. This would imply that another parameter (or other parameters) play a major role in their resistance to shear. Among the properties known to affect the resistance of adherent objects to shear, the objects size plays a major role under dynamic conditions [120]. The 6 μm-microspheres used in this study are around ten times larger than spores. Consequently, it is likely that these spheres reach the external region of the boundary layer [6] and are subjected to the effect of large-scale motion, which might explain their poor resistance to detachment. This hypothesis is confirmed by the very high resistance to shear observed with the smallest microspheres (0.5 μm and 0.2 μm).

Irrespective of the spores properties, the same trends applied to their resistance to detachment i.e. an increase in time and/or temperature of drying clearly resulted in a

decrease in spore detachment by shear. This cannot be attributed to the presence of an exosporium, appendages or a mucous layer around the spores. This observation suggests once again the key role played by the liquid film in interface phenomena, as suggested by previous results, which showed that partial drying increased the resistance to shear of Bacillus spores [121]. However, the increase in the resistance to detachment was somewhat more pronounced in the case of *B. cereus* spores (e.g. when drying occurred at 35°C). These spores being hydrophobic, one can reasonably suspect the presence of a residual liquid film (or of air bubbles) between the exosporium and the substratum, which may affect the hydrophobic interaction between spores and substratum.

4.5 Summary

As a closing remark, it is important to point out that, in most environments, many bacterial soils undergo a drying step. This is particularly true in the food industry, on open contaminated surfaces, such as conveyor belts or walls, but also at the air-liquid interface on surfaces of partly-filled equipment, including tanks, pumps, valves, or piping systems, whether during the production phase or after a hygiene procedure. According to our results, these drying conditions would result in increased resistance of adherent bacteria to detachment, which, at least in the case of bacterial spores is much higher than could have been reasonably expected. Therefore, the presence of dried bacterial soils should be a concern in the food industry.

CHAPTER 5
CONCLUSION

We have demonstrated that the presence of partially wettable particles on the walls can dramatically affect the dynamics of a liquid interface that is injected into a Hele-Shaw cell filled with air. The development of fingering patterns was demonstrated despite the fact that the displacement of less by a more viscous fluid is generally admitted as stable and would then constitute an inverse saffman-taylor instability. The patterning would occur in certain wetting conditions which lead to particles collection by the interface. The destabilization arises when the available surface of the meniscus is insufficient to accommodate new particles. As a consequence, the critical radius at which the instability occurs and the width of the fingers can be calculated by simply balancing the space available on the meniscus with the area needed to accommodate additional particles encountered by the liquid-air interface during its motion.

In parallel, a numerical model was developed to investigate the motion of an ellipsoid particle near a wall in a shearing flow at low Reynolds number. This was done for various aspect ratios, flow fields and particle position with respect to the wall. The effect of a plane wall on the ellipsoid Jeffrey orbits and the particles center was described. It was shown that the particle can be lifted or attracted to the wall depending on its aspect ratio, orientation and position. It was found that for a prolate particle (mimicking spore's shape) the maximum lift is reached for an ellipsoid of aspect ratio of 2.2 ± 0.2.

Finally, understanding the attachment of the micro-organisms on a surface is the key to remove them efficiently. Examination of industrial environment shows that many bacterial soils undergo a drying step. This is particularly true in the food industry, on open contaminated surfaces, such as conveyor belts or walls, but also at the air-liquid interface on surfaces of equipment, including tanks, pumps, valves, or piping systems, whether during the production phase or after a hygiene procedure. Our results show that the spores resistance to the flow was significantly higher than that of the latex microspheres. Furthermore differences were

observed between the spores strains. For instance, B. Pumilus were more resistant when dried at 35°C and 50°C while B. Cereus spores are resistant to detachment when dried at 25°C and unlike to B. Subtilis that are relatively easy to remove independently to drying conditions. Therefore, the presence of dried bacterial soils should be a concern in the food industry.

APPENDIX A
PRELIMINARY WORK

A.1 Background

Particle removal is studied in the presence of a two-phase flow, specifically that of an air-water system. Figure A-1 illustrates the example of an air bubble moving in a capillary tube at two different flow rates. In this configuration, a thin film of fluid is formed between the wall and the bubble. Bretherton's law [122] estimates the liquid film thickness H as $H/D = 0.64C_a^{2/3}$, where D is the tube diameter, C_a is the capillary number defined as $C_a = \mu U/\gamma$, μ is the dynamic viscosity, U is the velocity of the bubble, and γ is the surface tension. That means that as the velocity of the bubble increases, the thickness of the liquid film increases as well. Note that this reasoning can be applied only in the regime where $C_a \ll 1$.

Now consider the case of particles attached to the inner walls of a capillary tube. A driving force is required to remove these particles from the wall. In the case of a two-phase flow, two possibilities can be distinguished: the air-water interface intersects the particle (Figure A-1-A) and the air-water interface passes over the particles (Figure A-1-B). In the first case, the detachment is aided directly by the capillary force. In the second case, the particles can detach due to the hydrodynamic forces of the flow.

A.2 Experiments

A preliminary study was performed on the device shown in (Figure A-2). We deposited hydrophilic micro-spheres onto a glass channel and then exposed the deposited particles to successive air-water interface passages to remove the micro-particles from the wall. All experiments were conducted in a micro-channel of 1 mm radius and with micro-spheres of 10 μm diameter. The interfaces were generated by injecting air bubbles into the channel. A volumetric flow rate is applied to the water, which in turn moves the bubble.

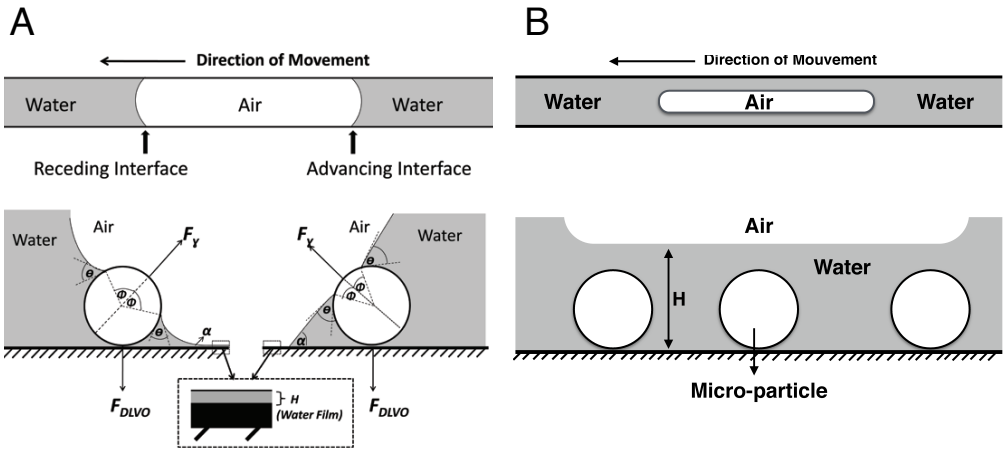

Figure A-1. Two-phase flow: motion of a bubble through a tube in the presence of microparticles. **(A)** At very low flow rates, the surface tension force acts directly on a particle [8]. **(B)** At high flow rates, the bubble elongates at the center of the tube and the particles do not intersect the air-water interface. Thus, the forces acting to remove the particles are purely hydrodynamic.

Figure A-2-B shows that the microparticles are removed from the wall. Some particles are collected by the interfaces and others are moving in the flow in front of the bubble. The rate of particle removal changes depending on the volumetric flow rate applied. The observations show that lower bubble velocities result in the removal of more particles (Figure A-3). Two phenomena are responsible for this removal depending on the flow rate applied. As the velocity decreases, the water film thickness separating the air bubble from the tube wall decreases and two cases can be distinguished:

(i) At low velocity, the film thickness is smaller than the particle diameter. This suggests that an air-water-particle interface is formed. The particle attaches to the interface due to the strong capillary forces and is transported away from the surface.

(ii) At high velocity, the film thickness is larger than the particle diameter. This suggests that there will be no air-water-particle interaction and, consequently, removal of particles from surface depends on hydrodynamic forces alone.

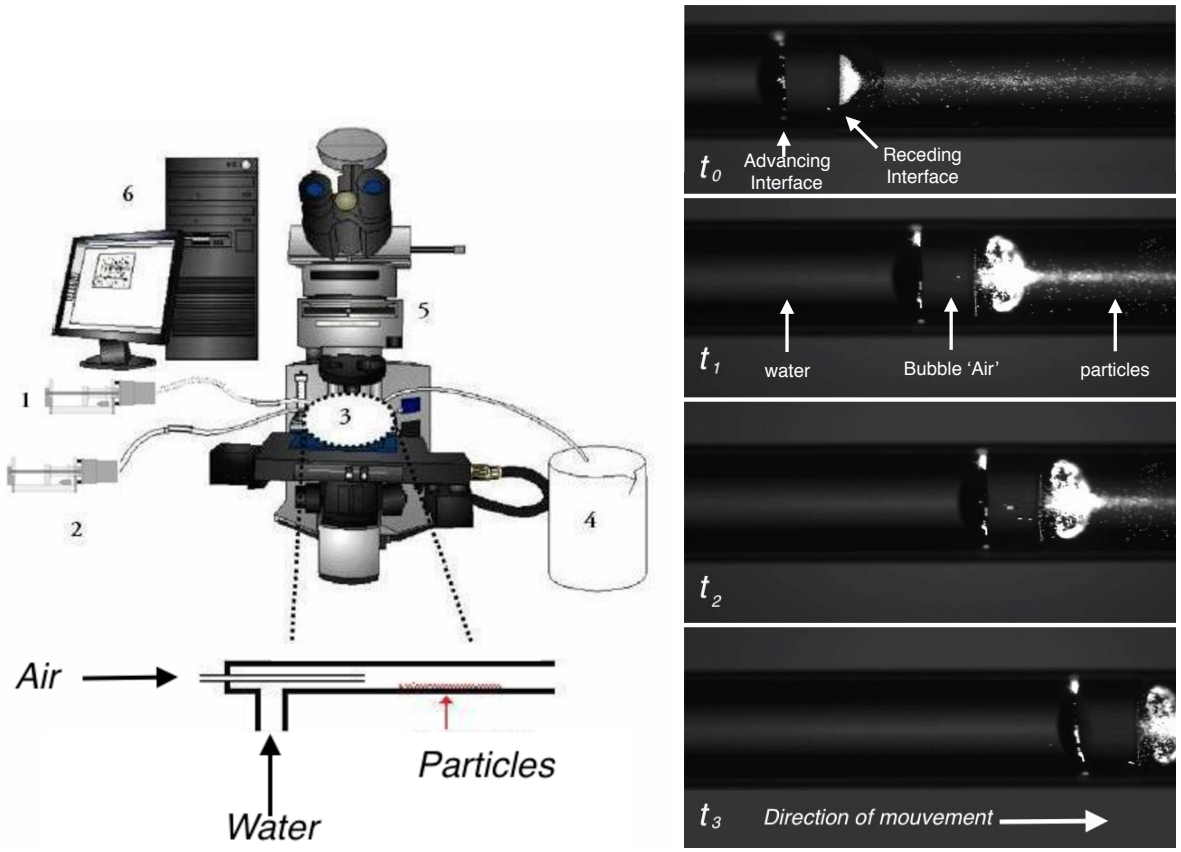

A B

Figure A-2. **(A)** Experimental setup for studying particle removal in a capillary tube: 1-syringe pump (air), 2-syringe pump (water), 3-capillary tubes (setup), 4-outlet of fluid, 5-microscope, and 6-computer. The capillary tube is initially filled with water and the micro-particles are on the surface. Air is injected into the tube until a bubble is formed and then a volumetric flow rate is applied on the water to push the bubble. **(B)** Time sequence of a bubble passing through the capillary at a flow rate of 2 ml/h displaces and removes the micro-particles

Note that in the first case, capillary and hydrodynamic forces act simultaneously, even if the capillary force is dominant. However one goal of our work is to isolate the effect of the capillary force on the particles. Additionally, counting the concentration of particles in the cylindrical tube made the quantification of results difficult.

A second set of experiments has been performed in a radial Hele-Shaw cell (Chapter 2) in an effort to overcome experimental difficulties that were observed in the capillary experiments.

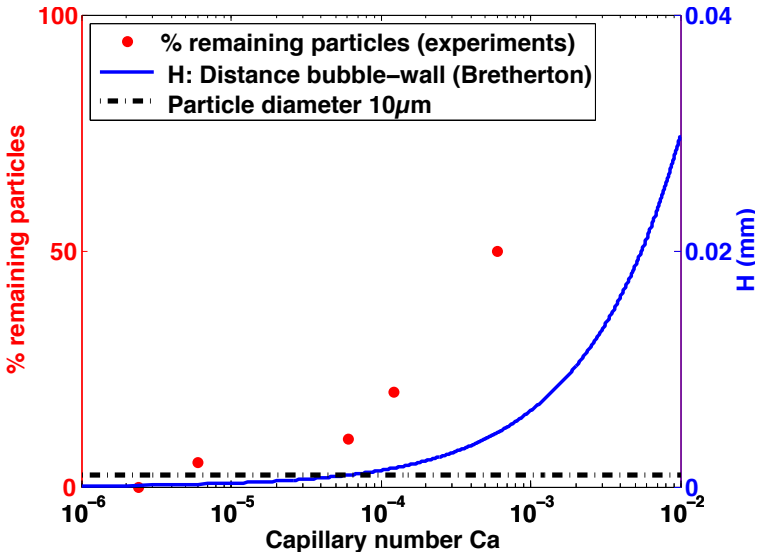

Figure A-3. Percentage of the remaining particles after the passage of the bubble subjected to various capillary numbers.

APPENDIX B
SUPPLEMENTARY INFORMATION

B.1 Evaluation of the critical radius

B.1.1 Introduction

When liquid is pushed inside an axisymmetric Hele-Shaw cell covered with hydrophilic particles, the water-air interface expands radially and collects particles. These particles form a monolayer of particles at the surface of the meniscus. Our hypothesis is that the interfacial instability occurs when the interface becomes entirely covered with a monolayer of packed particles. Indeed, as long as it is energetically favorable for the particles to be captured by an extended interface (rather than entering the liquid or staying in the gas phase), the interface needs to grow in a different way to increase the surface/volume ratio, explaining the appearance of the fingers. To verify this hypothesis, we estimate the critical radius r_c when the interface becomes entirely covered with particles from simple geometrical considerations. First, we must determine the shape of the liquid/air meniscus of the capillary bridge. In the static case (or quasi-static) and at low Bond number (where the effect of gravity can be neglected), the shape is the result of the minimization of the global surface energy (gas/wall, liquid/wall, gas/liquid) at fixed liquid volume. The global constraint of minimum interfacial energy leads to the two following conditions:

1. The triple line on the walls satisfies the Young-Dupré's equation: $\cos\alpha_E = \frac{\gamma_{GW}-\gamma_{LW}}{\gamma_{GL}}$, with α_E the contact angle with the walls and γ_{GW}, γ_{LW} and γ_{GL} the gas-wall, liquid-wall and gas-liquid surface energy.

2. The liquid/air interface (meniscus) adopts the minimum surface configuration at fixed liquid volume.

B.1.2 Approximation of the meniscus shape

This problem is, in general, a rather complex optimization problem. If we introduce a function $\varphi(\vec{x})$ in the three dimensional Euclidian space, equal to zero on the liquid-air interface, with $\mathcal{A}(\varphi(\vec{x}))$, $\mathcal{V}(\varphi(\vec{x}))$ the area and volume of this interface respectively, the minimization of the liquid-air interface can be obtained by the method of Lagrange multipliers,

with the action defined as:

$$\mathcal{L} = \mathcal{A}(\varphi) + \lambda(\mathcal{V}(\varphi) - \mathcal{V}_0),$$

where $\mathcal{V}_0$ is the volume of the liquid bridge between the walls. This formula reflects that fact that we are minimizing the surface area, while constraining the volume of fluid, where λ is the Lagrange multiplier. Of course, the solution of the problem must also satisfy the boundary conditions on the walls. Following Yao [123], it can be shown that the solution of this minimization problem is a constant mean curvature surface (CMC) which satisfies the Young Dupré's condition on the walls. For an axisymmetric configuration, if $r(z)$ denotes the radius of the meniscus at a given height z, the equation of the liquid/gaz surface of the liquid bridge is

$$C_m = \frac{1}{R_1} + \frac{1}{R_2} = \frac{-r''}{1+r'^2}^{3/2} + \frac{1}{r\sqrt{1+r'^2}} = \text{constant}, \tag{B–1}$$

where R_1 and R_2 are the two principal radii of curvature and $-H/2 < z < H/2$, with H the distance between the walls (see Fig. B-1). The first and second derivative of the radius r with respect top z are denoted r' and r''. Integration of this equation leads to

$$\frac{r}{\sqrt{1+r'^2}} = \frac{C_m}{2}r^2 + D,$$

for which the general solution can be written as a sum of elliptic functions (D being a constant). Analytical solution for a given set of boundary conditions (for the triple line) cannot be obtained analytically.

We will now prove that the problem can be drastically simplified when the radius $R_o = r(z{=}0)$ is much larger than the height H between the walls. We will show that in this case, the meniscus shape can be approximated by a toroidal shape, that is to say a surface of revolution generated by revolving a portion of a circle (which intersects the walls with the appropriate contact angle α_E) around the z-axis (see Fig. B-1).

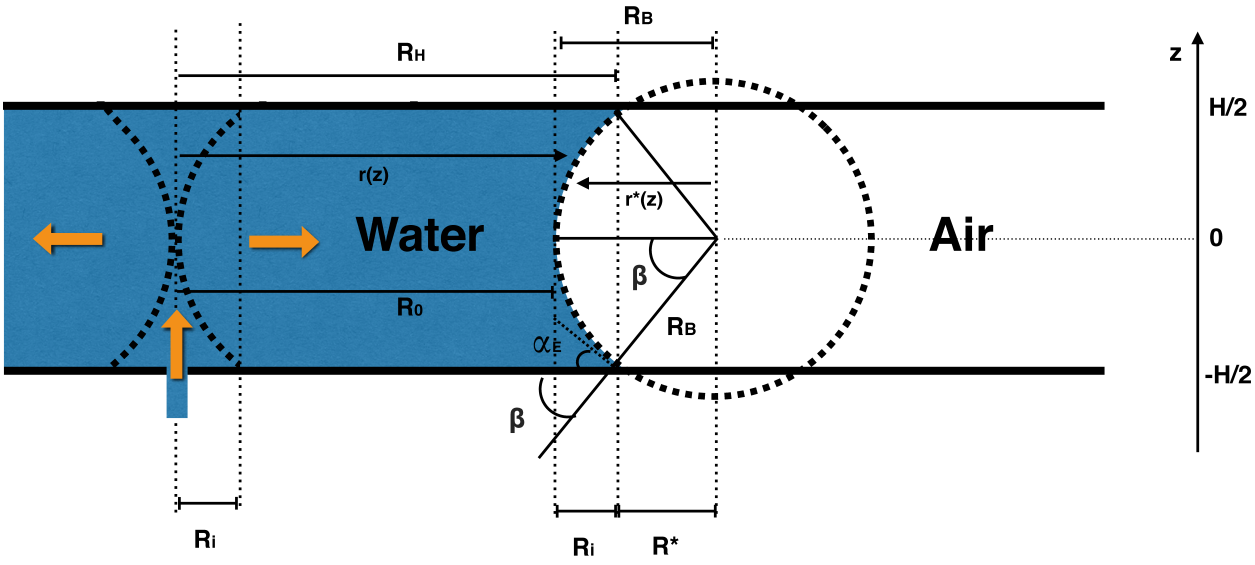

Figure B-1. Schematic of the meniscus in the toroidal approximation.

Indeed, this torroidal shape satisfies the boundary condition on the walls. Moreover, we can prove that if $H/R_o \ll 1$, this toroidal meniscus is a CMC surface at leading order. Indeed, using, the notation introduced on Fig. B-1, we have

$$r(z) = R_o + R_B - r^*(z),$$

with $R_o = r(z{=}0)$ and $R_B = H/(2\cos(\alpha_E))$ the bend radius of the meniscus. Using the Pythagorean theorem, we have $r^*(z) = \sqrt{R_B^2 - z^2}$ and thus

$$r(z) = R_o + R_B\left(1 - \sqrt{1 - \frac{z^2}{R_B^2}}\right). \tag{B–2}$$

If we use equation (B–2) in (B–1), we obtain

$$C_m(z) = -\frac{1}{R_B} + \frac{\sqrt{1 - \frac{z^2}{R_B^2}}}{R_o + R_B\left(1 - \sqrt{1 - \frac{z^2}{R_B^2}}\right)}$$

For perfectly wetting walls ($\alpha_E = 0$, $R_B = H/2$) and considering $H/R_o \ll 1$, we have at first order

$$C_m \approx \frac{-1}{R_B}.$$

For $\alpha_E = \pi/2$ ($R_B \to \infty$), the "cylindrical" meniscus is the exact solution of the problem:

$$C_m = \frac{1}{R_o}$$

In the intermediate configurations ($0 < \alpha_E < \pi/2$), we can estimate the mean curvature variation along the z-axis $\Delta C_m = |C_m(z{=}H/2) - C_m(z=0)|$ normalized by the maximum principal curvature $C_{max} = max\left(|1/R_1|, |1/R_2|\right)$ (to avoid normalizing problems when $C_m = 0$). This variation is represented on Fig. B-2. The graph shows that the variation of the mean curvature is less than 1% for $H/R_o = 0.01$, less than 10% for $H/R_o = 0.1$ and reaches a maximum of 25% for the worst configuration ($H/R_o = 0.5$). Thus the approximation of the liquid/air interface by a toroidal shape is a good qualitative approximation for the estimation of the critical radius in our experiments.

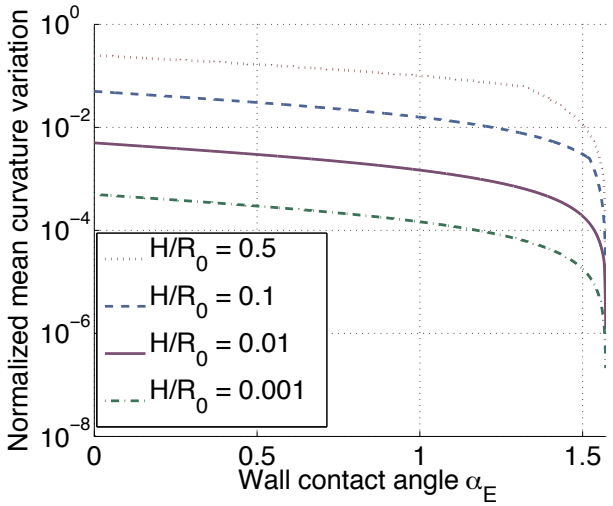

Figure B-2. Normalized mean curvature variation along z-axis $\Delta C_m/C_{max}$ as a function of different wall contact angles α_E for different aspect ratios H/R_o

B.1.3 Evaluation of the critical radius r_c in the toroidal approximation

In this section, we compute the critical radius r_c at which the liquid-gas interface becomes fully covered with particles. We assume that every particle, initially lying on the plates of the Hele-Shaw cell, is removed from the plate and enters the meniscus upon contact with

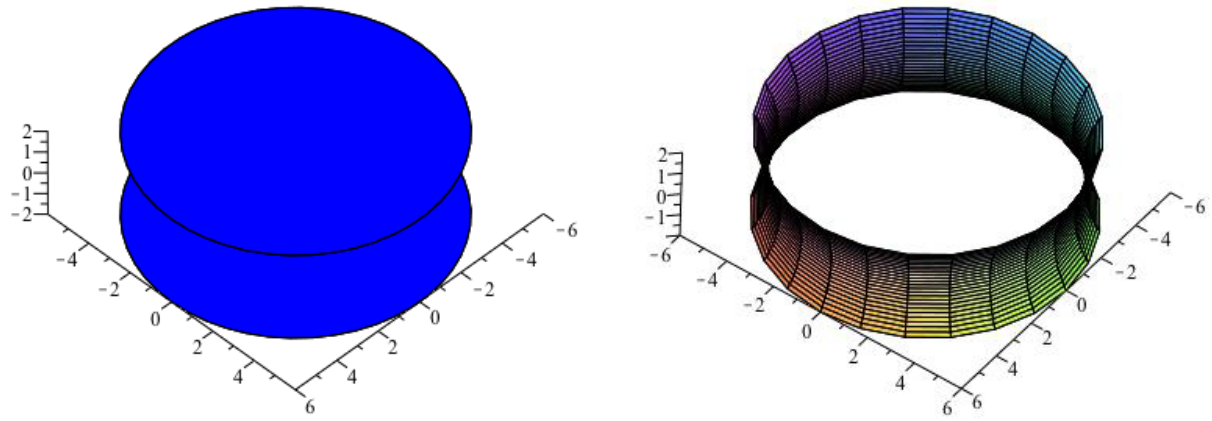

A B

Figure B-3. Schematic of **(A)** the surface area S_1 covered by water on the plates and **(B)** the interface S_2 between the air and water.

the liquid. Consequently, the critical radius is set by the balance

$$CS_1 = \phi S_2, \tag{B–3}$$

where S_2 is the area of the meniscus (see Fig.B-3) and ϕ is the packing on the interface at which the instability (fingering) initiates. The concentration, or areal fraction, of particles on the plates C is a constant, known value for any one experiment and the coverage of liquid on the plates is given by $S_1 = 2\pi R_H^2$, where R_H is defined in Fig. B-1. When the above balance is satisfied, R_H is equated with r_c.

The particles can cover a maximum fraction ϕ of the air-liquid interface, which depends on the shape and arrangement of the particles. The left picture in Fig. B-4 shows the most condensed organization that spherical particles can take (hexagonal packing arrangement), leading to $\phi = \pi/2\sqrt{3} = 0.9069$. Nevertheless, there is no reason for the particles to be organized into a crystalline structure, so we equate ϕ with maximum random packing of a two-dimensional surface. For a random organization of perfect spheres, analytical

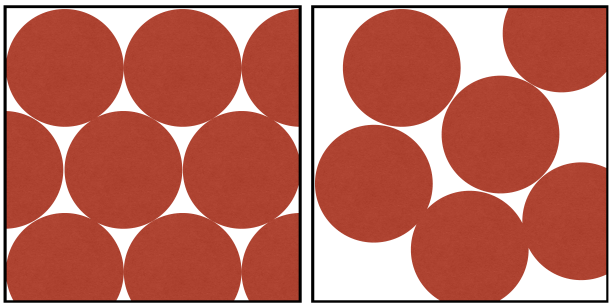

Figure B-4. Different organizations of the particles over a surface. For an organized structure (left), the maximum areal fraction is $\phi = 0.9069$; for a random organization of the particles on the two-dimensional interface, the value is lower. The picture (right) of one realization of a random packing arrangement gives $\phi = 0.69$.

calculations by Torquato et al [42] gives $\phi \simeq 0.8$. In the calculations, values of $\phi = 0.8$ and 0.7 are used to demonstrate the range of possible solutions given variations in this parameter.

To complete the calculation of r_c, we need to compute the lateral surface S_2 of the liquid/air interface as a function of the expanding radius R_H. It is obtained by rotating the circular portion $r(z)$ from $z = -H/2$ to $z = H/2$ around the z-axis:

$$\begin{aligned} \mathrm{d}S_2 &= 2\pi r(z)\mathrm{d}s = 2\pi r(z)\sqrt{1+\left(\frac{\partial r}{\partial z}\right)^2}\mathrm{d}z \\ S_2 &= 2\pi \int_{-H/2}^{H/2} r(z)\sqrt{1+\left(\frac{\partial r}{\partial z}\right)^2}\mathrm{d}z, \end{aligned} \tag{B–4}$$

where $r(z)$ is the expression for the dependence of the radius of the interface on z,

$$\begin{aligned} r(z) &= R_H + R^* - r^*(z) \\ &= R_H + R_B\sin(\alpha_E) - \sqrt{R_B^2 - z^2}. \end{aligned} \tag{B–5}$$

Substituting equation (B–5) in (B–4) gives

$$S_2 = 2\pi \int_{-H/2}^{H/2} \left(R_H + R_B \sin(\alpha_E) - \sqrt{R_B^2 - z^2} \right) \sqrt{1 + \left(\frac{\partial (R_H + R_B \sin(\alpha_E) - \sqrt{R_B^2 - z^2})}{\partial z} \right)^2} \, \mathrm{d}z$$

$$S_2 = 2\pi \int_{-H/2}^{H/2} \left(R_H + R_B \sin(\alpha_E) - \sqrt{R_B^2 - z^2} \right) \sqrt{1 + \left(\frac{z}{\sqrt{R_B^2 - z^2}} \right)^2} \, \mathrm{d}z$$

$$S_2 = 2\pi \int_{-H/2}^{H/2} \left(R_H + R_B \sin(\alpha_E) - \sqrt{R_B^2 - z^2} \right) \left(\frac{R_B}{\sqrt{R_B^2 - z^2}} \right) \mathrm{d}z$$

$$S_2 = 2\pi \int_{-H/2}^{H/2} \left(\frac{R_H R_B + R_B^2 \sin(\alpha_E)}{\sqrt{R_B^2 - z^2}} - R_B \right) \mathrm{d}z.$$

Noting that $R_B \geqslant H/2$, the integral can be evaluated as

$$\int_{-H/2}^{H/2} \frac{1}{\sqrt{R_B^2 - z^2}} \mathrm{d}z = \left[\arcsin\left(\frac{z}{R_B} \right) \right]_{-H/2}^{H/2}$$

$$\int_{-H/2}^{H/2} \frac{1}{\sqrt{R_B^2 - z^2}} \mathrm{d}z = 2 \arcsin\left(\frac{H}{2R_B} \right)$$

$$\int_{-H/2}^{H/2} \frac{1}{\sqrt{R_B^2 - z^2}} \mathrm{d}z = 2 \arcsin\left(\cos(\alpha_E) \right).$$

The evaluation of S_2 then becomes

$$S_2 = 2\pi((R_H R_B + R_B^2 \sin(\alpha_E))(2 \arcsin(\cos(\alpha_E))) - R_B H)$$

$$S_2 = 2\pi((R_H \frac{H}{2\cos(\alpha_E)} + \left(\frac{H}{2\cos(\alpha_E)} \right)^2 \sin(\alpha_E))(2 \arcsin(\cos(\alpha_E))) - \frac{H^2}{2\cos(\alpha_E)})$$

$$S_2 = \frac{2\pi H R_H \arcsin(\cos(\alpha_E))}{\cos(\alpha_E)} + \frac{\pi H^2 \sin(\alpha_E) \arcsin(\cos(\alpha_E))}{\cos(\alpha_E)^2} - \frac{\pi H^2}{\cos(\alpha_E)}$$

$$S_2 = \frac{2\pi H R_H (\pi/2 - \arccos(\cos(\alpha_E)))}{\cos(\alpha_E)} + \frac{\pi H^2 \sin(\alpha_E)(\pi/2 - \arccos(\cos(\alpha_E)))}{\cos(\alpha_E)^2} - \frac{\pi H^2}{\cos(\alpha_E)}.$$

With some final simplifications, the surface S_2 can be written as

$$S_2 = \frac{\pi H}{\cos \alpha_E} \left[2R_H \left(\frac{\pi}{2} - \alpha_E \right) + H \left(\left(\frac{\pi}{2} - \alpha_E \right) \tan \alpha_E - 1 \right) \right]. \tag{B–6}$$

Using equation (B–6) in (B–3) gives a quadratic expression for r_c, where $r_c = R_H$ at the point at which the instability begins. The predicted value of r_c must be positive and non-zero for every possible combination of C and α_E. Hence, the general formula for any

contact angle α_E is

$$\frac{r_c}{H} = \frac{\phi}{4C\cos\alpha_E}\left[2\left(\frac{\pi}{2}-\alpha_E\right)+\sqrt{4\left(\frac{\pi}{2}-\alpha_E\right)^2+\frac{8C}{\phi}\left(\left(\frac{\pi}{2}-\alpha_E\right)\sin\alpha_E-\cos\alpha_E\right)}\right]. \tag{B–7}$$

Evaluating the limits of this last expression gives

$$\frac{r_c}{H} = \frac{\phi\left(\pi+\sqrt{\pi^2-\frac{8C}{\phi}}\right)}{4C}$$

for $\alpha_E \to 0$ and

$$\frac{r_c}{H} = \frac{\phi}{C}$$

for $\alpha_E \to \pi/2$.

B.2 Calculations in the rectangular tube

B.2.1 Critical length

The fingering instability starts when there is no more space available on the meniscus to collect the particles. In the radial configuration, the critical radius after which the instability begins was detailed in the previous section. The same reasoning, applied to the simpler case of rectangular tube, gives the critical length l_c at which the instability begins as

$$l_c = \frac{\phi HW}{2C(H+W)}, \tag{B–8}$$

where H and W are the height and the width of the tube respectively (see Fig.B-5). This estimation compares well, qualitatively, with the measured destabilization length. Nevertheless, the length is small and difficult to measure with any precision, leading to large error bars. Consequently, we have not presented these results.

B.2.2 Finger width

Once the interface is completely filled with particles, the shape of the advancing interface will be modified. This modification, or instability of the interface, results from the increase of the volume/surface ratio and creation of enough surface to integrate the particles encountered

by the meniscus. In the rectangular configuration, the instability is a finger with a fixed width L_D as depicted in the right sketch of the B-5.

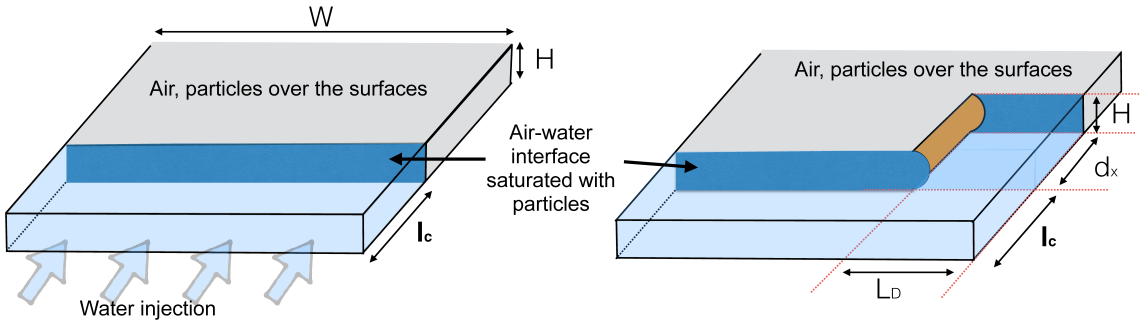

Figure B-5. Schematic of the finger instability created in a rectangular tube.

In order to calculate the finger width L_D, a method similar to the one used for the critical radius calculation (section 1) is used. The method is based on the comparison between the surface available on the interface to integrate particles (ϕS_2) for a given finger width L_D and the surface required to integrate all the particles met by the meniscus, CS_1. Assuming the finger width is quasi constant, the surface area S_1 wet by the liquid is a sum of three surfaces (upper, bottom and lateral walls):

$$S_1 = 2L_D d_x + H d_x.$$

The surface area S_2 depends on the contact angle. For $\alpha_E = \pi/2$ the surface is a rectangle,

$$S_2 = H d_x,$$

for $\alpha_E = 0$ the surface is a half-cylinder of bend radius $R_B = H/2$,

$$S_2 = \pi d_x \frac{H}{2}.$$

The finger width is then simply obtained from the balance $CS_1 = \phi S_2$. Resolution of this simple equation leads to

$$\underbrace{L_D = \frac{\phi H}{2C} - \frac{H}{2}}_{\text{for } \alpha_E=\pi/2} \quad and \quad \underbrace{L_D = \frac{\phi \pi H}{4C} - \frac{H}{2}}_{\text{for } \alpha_E=0} \tag{B–9}$$

APPENDIX C
BOUNDARY INTEGRAL EQUATIONS (BIE)

An Integral equation is a reformulation of a differential equation as a convolution of a kernel, so called Green's function or fundamental solution, with a force density of equal magnitude as the forcing term of the underlying differential equation [124, 125]. The introduction of the integral equations was done by Abel [126] in 1823. The mathematical physics field started studying these equations in the begining of the 20 century by the emergence of a valuable branch: the potential theory [127, 128].

C.1 Potential theory

Originally and before this theory, the potential notion was related to the forces in the gravitation law called "Newton's potential". Introduced by P. Laplace, J. Lagrange and L. Euler at the end of 18th century this field became of major importance [129]. In 1828 G. Green called a function that Lagrange established for a field of gravitational forces as *potential function*. Later, G. Gauss discovered that the potentials method can be used to solve a wide range of mathematical physics problems and not only gravitation theory. He considered then the potential as a function whose gradient is a vector field.

For example, let one consider a vector field $\mathbf{f} = \sum_{i=1}^{3} f_i \mathbf{e_i}$ where $f_i = f_i(x, y, z)$ are the component of the vector $\mathbf{f}$ applied at the point $\mathbf{x} = (x, y, z)$, and $\mathbf{e_i}$ are the basic vectors of orthogonal coordinate system. The potential of the vector $\mathbf{f}$ is then the scalar function $u(x, y, z)$ such as $\nabla u = (\partial u/\partial x, \partial u/\partial y, \partial u/\partial z) = \mathbf{f}$.

As it was mentioned, the origins of the potential was linked to the gravitation attraction rule. From this law, the force $\mathbf{K}$ acting between two mass points m_1 and m_2 separated by a distance r can be expressed as:

$$\mathbf{K} = -\frac{Gm_1m_2\mathbf{r}}{r^3}$$

where $G = 6.674 \cdot 10^{-11} m^3/(kg \cdot s^2)$ is the gravitational constant and $\mathbf{r}$ is the distance vector between the two particles. Since $\mathbf{curl}\ \mathbf{K} = \nabla \times \mathbf{K} = \mathbf{0}$, there is a scalar function Q, called *potential*, such that $\nabla Q = \mathbf{K}$. Therefore, the potential also called Newton's potential can be

written as

$$Q = Gm_1m_2\frac{1}{r}$$

The function Q defines the work which has to be done to move one of the mass points to infinity if the other one is fixed [130, 131].

C.2 Potential theory in fluid dynamics

Going back to the fluid dynamics, the equations governing any flow are obtained by considering two equations, conservation of mass and momentum:

$$\frac{\partial \rho}{\partial t} + \nabla \cdot (\rho \mathbf{u}) = 0 \tag{C–1}$$

$$\rho \frac{D\mathbf{u}}{Dt} = \nabla \cdot \sigma + \rho \mathbf{f} \tag{C–2}$$

Here, ρ is the density, $\mathbf{u}$ is the velocity, σ the stress tensor and $\mathbf{f}$ the external body force per unit mass. Depending on the problem that we have, different simplifications could be done. If the fluid used is **Newtonian**, the stress tensor can be written as

$$\sigma = -p\mathbf{I} + 2\mu\mathbf{E} \tag{C–3}$$

where $\mathbf{E} = \frac{1}{2}[(\nabla \mathbf{u}) + (\nabla \mathbf{u})^T] - \frac{1}{3}(\nabla \cdot \mathbf{u})\mathbf{I}$ is the rate of strain tensor and p is simply the pressure. For **incompressible** fluids, the density ρ is constant. Therefore $\partial\rho/\partial t = 0$. Combining all the above equations leads to the Navier-Stockes equations for incompressible Newtonian fluid:

$$\rho\left(\frac{\partial \mathbf{u}}{\partial t} + (\mathbf{u} \cdot \nabla)\mathbf{u}\right) = \nabla p + \mu \nabla^2 \mathbf{u} + \rho \mathbf{f} \tag{C–4}$$

$$\nabla \cdot \mathbf{u} = 0 \tag{C–5}$$

Now, in order to introduce the potential theory in hydrodynamics, let's consider a steady potential flow characterized by being **inviscid** and **irrotational**. Since $\nabla \times \mathbf{u} = \mathbf{0}$, we can define a scalar potential function, ϕ, such that $\nabla\phi = \mathbf{u}$. Notice that ϕ, called also the velocity potential, has no direct physical meaning, it's just a mathematical conceptual construction.

Substituting in C–5, we find Laplace's equation

$$\nabla \cdot \nabla\phi = \nabla^2\phi = 0 \tag{C–6}$$

This equation is one of the most widely used partial differential equation in mathematical physics problems. Solutions of Laplace's equation C–6 in a domain Ω are called harmonic in Ω. As with any PDE, Laplace equation needs to satisfy additional conditions. The boundary conditions are the additional equations specific to each problem such as:

–The Dirichlet problem specifying the values that the solution needs to take on along the boundary of the domain Γ,

$$\phi = f(x);\ x\ \in\ \Gamma \tag{C–7}$$

where f(x) is a given and continuous function on Γ.

–The Neumann problem specifying the values that the derivative of the solution needs to take on the boundary of the domain Γ,

$$\partial\phi/\partial n = g(x);\ x\ \in\ \Gamma \tag{C–8}$$

where n is the outward normal of Γ,

C.3 Integral representations

George Green [61, 125] in his famous essay on 1828 [132] attempted to construct a solution of $\nabla^2\mathbf{u} = -\mathbf{f}$ within a volume V by investigating the partial differential equation:

$$\nabla^2 G(\mathbf{r}, \mathbf{r_0}) = -4\pi\delta(\mathbf{r} - \mathbf{r_0}) \tag{C–9}$$

with the assumption that for a given closed region Ω, there exists a harmonic function U that satisfies the boundary condition

$$U = -\frac{1}{R}\ on\ \Gamma \tag{C–10}$$

where, $R = |\mathbf{r} - \mathbf{r_0}|$. One can then define a function

$$G = \frac{1}{R} + U \tag{C–11}$$

It is clear that G satisfy the Laplace equation everywhere except at the pole, where it is singular. Green overcame the singular nature of G by introducing a small sphere around the singularity at $\mathbf{r_0}$ to exclude it from the volume V. Furthermore, G takes the null value at the boundary Γ. G is known as the Green's function. Green went on to prove that for a harmonic function ϕ, whose boundary value is given by a continuous function $\phi(\mathbf{x})$, $\mathbf{x} \in \Gamma$, its solution is represented by the boundary integral equation

$$\phi(\mathbf{x}) = -\frac{1}{4\pi} \iint_{\Gamma} \phi \frac{\partial G}{\partial n} dS; \quad \mathbf{x} \in \Omega \tag{C–12}$$

This solved the boundary value of u on the boundary Γ. Note that the equation C–12 is a solution of a Dirichlet boundary problem. Thus, depending on the integration domain and the boundary conditions different types of potentials can be distinguished: volume potentials, simple layer potentials or double layer potentials. Solutions of Poisson equation $\Delta u + f = 0$, for example, is a combination of *potentials* created in the space by a distributed sources over a volume V or a surface S such as:

Newtonien potential

$$u(\mathbf{x}) = \frac{1}{4\pi} \int_{V} f(\mathbf{y}) \frac{dV_y}{|y - x|} \tag{C–13}$$

Simple layer potential

$$u(\mathbf{x}) = \frac{1}{4\pi} \int_{S} \phi(\mathbf{y}) \frac{dS_y}{|y - x|} \tag{C–14}$$

Double layer potential

$$u(\mathbf{x}) = \frac{1}{4\pi} \int_{S} \psi(\mathbf{y}) \frac{\partial}{\partial n} \frac{dS_y}{|y - x|} \tag{C–15}$$

Obviously, solving Poisson's equation is reduced to an integral equation over the boundary S with the unknown ϕ or ψ [133]. Note that the potentiels are expressed in terms of singular integrals when x laid on the boundaries. In fact, the initial boundary integral equation is

written as a combination of the different potentials "*direct boundary integral representation*". Neverthelesss, Obqvist in 1930 [134] noted that the solution of stokes flow, for example, can be found with just one of these potentials independently. Thus, a new class of boundary integral methods is born, "*indirect or generalized boundary integral method*". This method is based on expressing the flow with just one type of potential. Automatically, the question of which potential can be used for a specific problem, is of great importance. The preferred choice of a potential is that which yields to the simplest integral equation [129]. Thus, usually the double layer potential is used for Dirichlet problems and the simple layer potential is used for Neumann problems.

Therefore, the solution of the initial equation is then a resolution of an integral equation over the problem boundaries. Thus, the Boundary Integral Method has a great advantage compared to other methods since the equations are formulated on the surface of the particle in our problem. That means that we reduce the dimension of the problem by 1 (from 3D to 2D).

REFERENCES

[1] C. Lelièvre, P. Legentilhomme, C. Gaucher, J. Legrand, C. Faille, and T. Bénézech, Cleaning in place: effect of local wall shear stress variation on bacterial removal from stainless steel equipment, Chemical Engineering Science **57**(8), 1287–1297 (2002).

[2] Y. Lequette, G. Boels, M. Clarisse, and C. Faille, Using enzymes to remove biofilms of bacterial isolates sampled in the food-industry, Biofouling **26**(4), 421–431 (2010).

[3] S. Haeghebaert, F. Le Querrec, A. Gallay, P. Bouvet, M. Gomez, and V. Vaillant, Les toxi-infections alimentaires collectives en France, en 1999 et 2000, Bull Epidemiol Hebdo **23**, 105–109 (2002).

[4] I. French Institute for Public Health Surveillance, Surveillance des toxi infections alimentaires collectives, http://www.invs.sante.fr/content/download/36247/175238/version/2/file/tiac_donnees_2010.pdf, 2010, Donnes de la déclaration obligatoire.

[5] S. Perni, T. G. Aldsworth, S. J. Jordan, I. Fernandes, M. Barbosa, M. Sol, R. P. Tenreiro, L. Chambel, I. Zilhão, B. Barata, et al., The resistance to detachment of dairy strains of Listeria monocytogenes from stainless steel by shear stress is related to the fluid dynamic characteristics of the location of isolation, International journal of food microbiology **116**(3), 384–390 (2007).

[6] C. Faille, T. Bénézech, W. Blel, A. Ronse, G. Ronse, M. Clarisse, and C. Slomianny, Role of mechanical vs. chemical action in the removal of adherent Bacillus spores during CIP procedures, Food microbiology **33**(2), 149–157 (2013).

[7] N. I. Abu-Lail and T. A. Camesano, Specific and nonspecific interaction forces between Escherichia coli and silicon nitride, determined by Poisson statistical analysis, Langmuir **22**(17), 7296–7301 (2006).

[8] S. Aramrak, M. Flury, and J. B. Harsh, Detachment of deposited colloids by advancing and receding air–water interfaces, Langmuir **27**(16), 9985–9993 (2011).

[9] C. Huh and S. Mason, The flotation of axisymmetric particles at horizontal liquid interfaces, Journal of Colloid and Interface Science **47**(2), 271–289 (1974).

[10] J. Shang, M. Flury, and Y. Deng, Force measurements between particles and the air-water interface: Implications for particle mobilization in unsaturated porous media, Water Resources Research **45**(6) (2009).

[11] F. Zoueshtiagh, M. Baudoin, and D. Guerrin, Capillary tube wetting induced by particles: towards armoured bubbles tailoring, Soft matter **10**(47), 9403–9412 (2014).

[12] J. Zhang, X. Sheng, and L. Jiang, The dewetting properties of lotus leaves, Langmuir **25**(3), 1371–1376 (2008).

[13] W. Barthlott and C. Neinhuis, Purity of the sacred lotus, or escape from contamination in biological surfaces, Planta **202**(1), 1–8 (1997).

[14] O. Pitois and X. Chateau, Small particle at a fluid interface: Effect of contact angle hysteresis on force and work of detachment, Langmuir **18**(25), 9751–9756 (2002).

[15] P. Sharma, M. Flury, and J. Zhou, Detachment of colloids from a solid surface by a moving air–water interface, Journal of Colloid and Interface Science **326**(1), 143–150 (2008).

[16] A. Scheludko, B. Toshev, and D. Bojadjiev, Attachment of particles to a liquid surface (capillary theory of flotation), Journal of the Chemical Society, Faraday Transactions 1: Physical Chemistry in Condensed Phases **72**, 2815–2828 (1976).

[17] M. Preuss and H.-J. Butt, Direct measurement of particle-bubble interactions in aqueous electrolyte: Dependence on surfactant, Langmuir **14**(12), 3164–3174 (1998).

[18] A. Leenaars and S. O?Brien, Particle removal from silicon substrates using surface tension forces, Philips J. Res **44**, 183–209 (1989).

[19] C. G. Suárez, J. Noordmans, H. C. van der Mei, and H. J. Busscher, Detachment of colloidal particles from collector surfaces with different electrostatic charge and hydrophobicity by attachment to air bubbles in a parallel plate flow chamber, Physical Chemistry Chemical Physics **1**(18), 4423–4427 (1999).

[20] C. Gómez Suárez, J. Noordmans, H. Van der Mei, and H. Busscher, Removal of colloidal particles from quartz collector surfaces as stimulated by the passage of liquid-air interfaces, Langmuir **15**(15), 5123–5127 (1999).

[21] I. Bihi, M. Baudoin, J. E. Butler, C. Faille, and F. Zoueshtiagh, Inverse Saffman-Taylor Experiments with Particles Lead to Capillarity Driven Fingering Instabilities, Phys. Rev. Lett. **117**, 034501 (Jul 2016).

[22] I. Bischofberger, R. Ramachandran, and S. R. Nagel, Fingering versus stability in the limit of zero interfacial tension, Nature communications **5** (2014).

[23] P. G. Saffman and G. Taylor, The penetration of a fluid into a porous medium or Hele-Shaw cell containing a more viscous liquid, in *Proceedings of the Royal Society of London A: Mathematical, Physical and Engineering Sciences*, volume 245, pages 312–329, The Royal Society, 1958.

[24] E. Álvarez-Lacalle, J. Ortín, and J. Casademunt, Nonlinear saffman-taylor instability, Physical review letters **92**(5), 054501 (2004).

[25] B. Levaché and D. Bartolo, Revisiting the Saffman-Taylor experiment: imbibition patterns and liquid-entrainment transitions, Physical review letters **113**(4), 044501 (2014).

[26] H. S. Hele-Shaw, Flow of water, Nature **58**, 34 (1898).

[27] B. Sandnes, H. Knudsen, K. Måløy, and E. Flekkøy, Labyrinth patterns in confined granular-fluid systems, Physical review letters **99**(3), 038001 (2007).

[28] B. Sandnes, E. Flekkøy, H. Knudsen, K. Måløy, and H. See, Patterns and flow in frictional fluid dynamics, Nature communications **2**, 288 (2011).

[29] Ø. Johnsen, R. Toussaint, K. J. Måløy, and E. G. Flekkøy, Pattern formation during air injection into granular materials confined in a circular Hele-Shaw cell, Physical Review E **74**(1), 011301 (2006).

[30] G. Markstein, Non-steady flame Propagation, McMillan Publication, New York (1964).

[31] P. Pelcé and A. Libchaber, *Dynamics of curved fronts*, Elsevier, 2012.

[32] E. Ben-Jacob, O. Schochet, A. Tenenbaum, I. Cohen, A. Czirok, T. Vicsek, et al., Generic modelling of cooperative growth patterns in bacterial colonies, Nature **368**(6466), 46–49 (1994).

[33] C. Chan and N. Liang, Observations of surfactant driven instability in a Hele-Shaw cell, Physical review letters **79**(22), 4381 (1997).

[34] J. Fernandez, R. Krechetnikov, and G. Homsy, Experimental study of a surfactant-driven fingering phenomenon in a Hele-Shaw cell, Journal of Fluid Mechanics **527**, 197–216 (2005).

[35] C. Neinhuis and W. Barthlott, Characterization and distribution of water-repellent, self-cleaning plant surfaces, Annals of botany **79**(6), 667–677 (1997).

[36] Q. Min, Y.-Y. Duan, X.-F. Peng, A. S. Mujumdar, C. Hsu, and D.-J. Lee, Froth flotation of mineral particles: Mechanism, Drying Technology **26**(8), 985–995 (2008).

[37] B. P. Binks, Particles as surfactants?similarities and differences, Current Opinion in Colloid & Interface Science **7**(1), 21–41 (2002).

[38] W. Ramsden, Separation of Solids in the Surface-Layers of Solutions and'Suspensions'(Observations on Surface-Membranes, Bubbles, Emulsions, and Mechanical Coagulation).–Preliminary Account, Proceedings of the royal Society of London **72**, 156–164 (1903).

[39] B. P. Binks and T. S. Horozov, Aqueous foams stabilized solely by silica nanoparticles, Angewandte Chemie **117**(24), 3788–3791 (2005).

[40] T. S. Horozov and B. P. Binks, Particle-Stabilized Emulsions: A Bilayer or a Bridging Monolayer?, Angewandte Chemie International Edition **45**(5), 773–776 (2006).

[41] B. P. Binks and T. S. Horozov, *Colloidal particles at liquid interfaces*, Cambridge University Press, 2006.

[42] S. Torquato, Nearest-neighbor statistics for packings of hard spheres and disks, Physical Review E **51**(4), 3170 (1995).

[43] J. G. Berryman, Random close packing of hard spheres and disks, Physical Review A **27**(2), 1053 (1983).

[44] R. G. Larson, *The Structure and Rheology of Complex Fluids*, Oxford University Press, New York, 1999.

[45] S. Yang and L. Leal, Particle motion in Stokes flow near a plane fluid-fluid interface. Part 2. Linear shear and axisymmetric straining flows, J. Fluid Mech. **149**, 275 (1984).

[46] R. Hsu and P. Ganatos, The motion of a rigid body in visous fluid bounded by a plane wall, J. Fluid Mech. **207**, 29–72 (1989).

[47] W. Russel, E. Hinch, L. Leal, and G. Tieffenbruck, Rods falling near a vertical wall, J. Fluid Mech. **83**, 273 (1977).

[48] M. Ingber and L. Mondy, A numerical study of three-dimensional Jeffery orbits in shear flow, J. Rheol. **38**, 1829–1843 (1994).

[49] C. Pozrikidis, Orbiting motion of a freely suspended spheroid near a plane wall, J. Fluid Mech. **541**, 105–114 (2005).

[50] E. Gavze and M. Shapiro, Particles in a shear flow near a solid wall: Effect of nonsphericity on forces and velocities, Int. J. Multiphase Flow **23**, 155–182 (1997).

[51] E. Gavze and M. Shapiro, Motion of inertial spheroidal particles in a shear flow near a solid wall with special application to aerosol transport in microgravity, J. Fluid Mech. **371**, 59–79 (1998).

[52] J. Park and J. E. Butler, Inhomogeneous distribution of a rigid fibre undergoing rectilinear flow between parallel walls at high Peclet numbers, Journal of Fluid Mechanics **630**, 267–298 (2009).

[53] J. Park, J. M. Bricker, and J. E. Butler, Cross-stream migration in dilute solutions of rigid polymers undergoing rectilinear flow near a wall, Physical Review E **76**(4), 040801 (2007).

[54] D. Saintillan, E. S. Shaqfeh, and E. Darve, Effect of flexibility on the shear-induced migration of short-chain polymers in parabolic channel flow, Journal of Fluid Mechanics **557**, 297–306 (2006).

[55] C. Pozrikidis, Flipping of an adherent blood platelet over a substrate, J. Fluid Mech. **568**, 161–172 (2006).

[56] N. Mody and M. King, Three-dimensional simulations of a platelet-shaped spheroid near a wall in shear flow, Phys. Fluids **17**, 113302 (2005).

[57] R. Holm and D. Söderberg, Shear influence on fibre orientation, Rheologica Acta **46**(5), 721–729 (2007).

[58] J. E. Castillo, *Mathematical aspects of numerical grid generation*, volume 8, SIAM: Society for Industrial and applied Mathematics, 1991.

[59] C. S. Peskin, The immersed boundary method, Acta numerica **11**, 1–39 (2002).

[60] S. Osher and R. Fedkiw, *Level set methods and dynamic implicit surfaces*, volume 153, Springer, 2002.

[61] A. H.-D. Cheng and D. T. Cheng, Heritage and early history of the boundary element method, Engineering Analysis with Boundary Elements **29**(3), 268–302 (2005).

[62] P. Banerjee, *Developments in Boundary Element Methods*, Applied Science Publishers, London, 1979.

[63] C. Brebbia, *Boundary Element Techniques in Computer-Aided Engineering*, Martinus Nijhoff Publishers, Dordrecht, 1984.

[64] C. Brebbia, *Progress in Boundary Element Methods*, Springer-Verlag, Berlin, 1981.

[65] C. Brebbia, J. Telles, and L. Wrobel, *Boundary Element Techniques*, Springer-Verlag, Berlin, 1984.

[66] W. Wendland, *Boundary element methods and their asymptotic convergence*, Springer-Verlag, Wien, New York, 1983.

[67] J. Whiteman, *Mathematics of Finite Elements and Applications V*, Academic Press, London, 1985.

[68] C. Pozrikidis, *Boundary integral and singularity methods for linearized viscous flow*, Cambridge Texts In Applied Mathematics, 1992.

[69] S. Kim and S. Karrila, *Microhydrodynamics*, Dover Books of Engineering, 2005.

[70] J. Blake, A note on the image system for a Stokeslet in a no-slip boundary, Proc. Camb. Phil. Soc. **70**, 303–310 (1971).

[71] M. Ingber and A. Mammoli, A Comparison of integral formulations for the analysis of low Reynolds number flows, Eng. Anal. Bound. Elem. **23**, 307–315 (1999).

[72] S. Jung, S. Spagnolie, K. Parikh, M. Shelley, and A.-K. Tornberg, Periodic sedimentation in a Stokesian fluid, Phys. Rev. E **74**, 035302 (2006).

[73] N. Phan-Thien and D. Tullock, Completed double layer boundary element method in elasticity, J. Mech. Phys. Sol. **41**, 1067–1086 (1993).

[74] H. Power and G. Miranda, Second kind integral equation formulation of Stokes flow past a particle of arbitrary shape, SIAM J Appl. Math **47**, 689–698 (1987).

[75] F. Hebeker, Efficient boundary element methods for three dimensional exterior viscous flow, Num. Meth. PDE **2**, 273–297 (1986).

[76] E. Becker, G. Carey, and J. Oden, *Finite Elements An Introductions*, volume 1, Prentice-Hall, Inc., Englewood Cliffs, New Jersey, 1981.

[77] G. B. Jeffery, The motion of ellipsoidal particles immersed in a viscous fluid, in *Proceedings of the Royal Society of London A: Mathematical, Physical and Engineering Sciences*, volume 102, pages 161–179, The Royal Society, 1922.

[78] L. Leal and E. Hinch, The rheology of a suspension of nearly spherical particles subject to Brownian rotation, J. Fluid Mech. **55**, 745 (1972).

[79] I. Zia, R. Cox, and S. Mason, Ordered aggregates of particles in shear flow, Proc. R. Soc. London, Ser. A **300**, 421441 (1967).

[80] B. Trevelyan and S. Mason, Particle motions in sheared suspensions I. Rotations, J. Colloid Sci. **5**, 345367 (1952).

[81] H. Goldsmith and S. Mason, Particle motions in sheared suspensions XIII. The spin and rotation of disks, J. Fluid Mech. **12**, 88 (1962).

[82] H. Goldsmith, S. Mason, and F. Eirich, *Rheology: Theory and applications*, Academic Press, New York, 1967.

[83] C. Faille, I. Bihi, A. Ronse, G. Ronse, M. Baudoin, and F. Zoueshtiagh, Increased resistance to detachment of adherent microspheres and Bacillus spores subjected to a drying step, Colloids and Surfaces B: Biointerfaces **143**, 293–300 (2016).

[84] R. Gorman, S. Bloomfield, and C. C. Adley, A study of cross-contamination of food-borne pathogens in the domestic kitchen in the Republic of Ireland, International Journal of Food Microbiology **76**(12), 143 – 150 (2002).

[85] H. Kusumaningrum, G. Riboldi, W. Hazeleger, and R. Beumer, Survival of foodborne pathogens on stainless steel surfaces and cross-contamination to foods, International Journal of Food Microbiology **85**(3), 227 – 236 (2003).

[86] J. Rayner, R. Veeh, and J. Flood, Prevalence of microbial biofilms on selected fresh produce and household surfaces, International Journal of Food Microbiology **95**(1), 29 – 39 (2004).

[87] E. Mettler and B. Carpentier, Localisation, dénombrement et identification de la contamination microbienne après nettoyage de joints en EPDM d'un circuit de pasteurisation de l'industrie laitière, Le Lait **77**(4), 489–503 (1997).

[88] J.-S. Peng, W.-C. Tsai, and C.-C. Chou, Inactivation and removal of Bacillus cereus by sanitizer and detergent, International journal of food microbiology **77**(1), 11–18 (2002).

[89] A. Ternström, A.-M. Lindberg, and G. Molin, Classification of the spoilage flora of raw and pasteurized bovine milk, with special reference to Pseudomonas and Bacillus, Journal of Applied Bacteriology **75**(1), 25–34 (1993).

[90] B. Dogan and K. J. Boor, Genetic diversity and spoilage potentials among Pseudomonas spp. isolated from fluid milk products and dairy processing plants, Applied and environmental microbiology **69**(1), 130–138 (2003).

[91] U. Rönner, U. Husmark, and A. Henriksson, Adhesion of Bacillus spores in relation to hydrophobicity, Journal of applied bacteriology **69**(4), 550–556 (1990).

[92] C. Faille, C. Jullien, F. Fontaine, M.-N. Bellon-Fontaine, C. Slomianny, and T. Benezech, Adhesion of Bacillus spores and Escherichia coli cells to inert surfaces: role of surface hydrophobicity, Canadian Journal of Microbiology **48**(8), 728–738 (2002).

[93] C. Faille, Y. Lequette, A. Ronse, C. Slomianny, E. Garénaux, and Y. Guerardel, Morphology and physico-chemical properties of Bacillus spores surrounded or not with an exosporium: consequences on their ability to adhere to stainless steel, International journal of food microbiology **143**(3), 125–135 (2010).

[94] A. Klavenes, T. Stalheim, O. Sjøvold, K. Josefsen, and P. Granum, Attachment of Bacillus cereus spores with and without appendages to stainless steel surfaces, Food and bioproducts processing **80**(4), 312–318 (2002).

[95] G. Tauveron, C. Slomianny, C. Henry, and C. Faille, Variability among Bacillus cereus strains in spore surface properties and influence on their ability to contaminate food surface equipment, International journal of food microbiology **110**(3), 254–262 (2006).

[96] C. G. Kumar and S. Anand, Significance of microbial biofilms in food industry: a review, International journal of food microbiology **42**(1), 9–27 (1998).

[97] J. W. Costerton, Z. Lewandowski, D. E. Caldwell, D. R. Korber, and H. M. Lappin-Scott, Microbial biofilms, Annual Reviews in Microbiology **49**(1), 711–745 (1995).

[98] H. E. Daneshvar Alavi and L. Truelstrup Hansen, Kinetics of biofilm formation and desiccation survival of Listeria monocytogenes in single and dual species biofilms with Pseudomonas fluorescens, Serratia proteamaculans or Shewanella baltica on food-grade stainless steel surfaces, Biofouling **29**(10), 1253–1268 (2013).

[99] P. Setlow, Spores of Bacillus subtilis: their resistance to and killing by radiation, heat and chemicals, Journal of applied microbiology **101**(3), 514–525 (2006).

[100] D. A. Jensen, L. M. Friedrich, L. J. Harris, M. D. Danyluk, and D. W. Schaffner, Quantifying transfer rates of Salmonella and Escherichia coli O157: H7 between fresh-cut produce and common kitchen surfaces, Journal of Food Protection® **76**(9), 1530–1538 (2013).

[101] L. A. Keskinen, E. C. Todd, and E. T. Ryser, Impact of bacterial stress and biofilm-forming ability on transfer of surface-dried Listeria monocytogenes during slicing of delicatessen meats, International journal of food microbiology **127**(3), 298–304 (2008).

[102] M. Banerjee and P. K. Sarkar, Antibiotic resistance and susceptibility to some food preservative measures of spoilage and pathogenic micro-organisms from spices, Food microbiology **21**(3), 335–342 (2004).

[103] S. A. Burgess, D. Lindsay, and S. H. Flint, Thermophilic bacilli and their importance in dairy processing, International journal of food microbiology **144**(2), 215–225 (2010).

[104] J. Dufrenne, P. Soentoro, S. Tatini, T. Day, and S. Notermans, Characteristics of Bacillus cereus related to safe food production, International Journal of Food Microbiology **23**(1), 99–109 (1994).

[105] K. Brown, Control of bacterial spores, British Medical Bulletin **56**(1), 158–171 (2000).

[106] U. Husmark and U. Rönner, The influence of hydrophobic, electrostatic and morphologic properties on the adhesion of Bacillus spores, Biofouling **5**(4), 335–344 (1992).

[107] G. Wirtanen and T. Mattila-Sandholm, Effect of the growth phase of foodborne biofilms on their resistance to a chlorine sanitizer. II, Lebensmittel-Wissenschaft+ Technologie **25**(1), 50–54 (1992).

[108] A. Rodriguez and L. A. McLandsborough, Evaluation of the transfer of Listeria monocytogenes from stainless steel and high-density polyethylene to Bologna and American cheese, Journal of Food Protection® **70**(3), 600–606 (2007).

[109] A. Rodriguez, W. R. Autio, and L. A. McLandsborough, Effect of biofilm dryness on the transfer of Listeria monocytogenes biofilms grown on stainless steel to bologna and hard salami, Journal of Food Protection® **70**(11), 2480–2484 (2007).

[110] L. T. Hansen and B. F. Vogel, Desiccation of adhering and biofilm Listeria monocytogenes on stainless steel: Survival and transfer to salmon products, International journal of food microbiology **146**(1), 88–93 (2011).

[111] M. Demilly, Y. Bréchet, F. Bruckert, and L. Boulangé, Kinetics of yeast detachment from controlled stainless steel surfaces, Colloids and Surfaces B: Biointerfaces **51**(1), 71–79 (2006).

[112] G. Guillemot, G. Vaca-Medina, H. Martin-Yken, A. Vernhet, P. Schmitz, and M. Mercier-Bonin, Shear-flow induced detachment of Saccharomyces cerevisiae from stainless steel: influence of yeast and solid surface properties, Colloids and Surfaces B: Biointerfaces **49**(2), 126–135 (2006).

[113] R. D. Deegan, O. Bakajin, T. F. Dupont, G. Huber, S. R. Nagel, and T. A. Witten, Capillary flow as the cause of ring stains from dried liquid drops, Nature **389**(6653), 827–829 (1997).

[114] C. Bernard, J.-P. Aimé, S. Marsaudon, R. Levy, A. M. Bonnot, C. Nguyen, D. Mariolle, F. Bertin, and A. Chabli, Drying nano particles solution on an oscillating tip at an air liquid interface: what we can learn, what we can do, Nanoscale Research Letters **2**(7), 309–318 (2007).

[115] N. Ishida and K. Higashitani, Interaction forces between chemically modified hydrophobic surfaces evaluated by AFM?The role of nanoscopic bubbles in the interactions, Minerals engineering **19**(6), 719–725 (2006).

[116] M. Plomp, T. J. Leighton, K. E. Wheeler, and A. J. Malkin, The high-resolution architecture and structural dynamics of Bacillus spores, Biophysical journal **88**(1), 603–608 (2005).

[117] A. J. Westphal, P. B. Price, T. J. Leighton, and K. E. Wheeler, Kinetics of size changes of individual Bacillus thuringiensis spores in response to changes in relative humidity, Proceedings of the National Academy of Sciences **100**(6), 3461–3466 (2003).

[118] C. Faille, Y. Sylla, C. Le Gentil, T. Bénézech, C. Slomianny, and Y. Lequette, Viability and surface properties of spores subjected to a cleaning-in-place procedure: consequences on their ability to contaminate surfaces of equipment, Food microbiology **27**(6), 769–776 (2010).

[119] Y. Lequette, E. Garénaux, T. Combrouse, T. D. Lima Dias, A. Ronse, C. Slomianny, X. Trivelli, Y. Guerardel, and C. Faille, Domains of BclA, the major surface glycoprotein of the B. cereus exosporium: glycosylation patterns and role in spore surface properties, Biofouling **27**(7), 751–761 (2011).

[120] G. Ziskind, M. Fichman, and C. Gutfinger, Particle behavior on surfaces subjected to external excitations, Journal of aerosol science **31**(6), 703–719 (2000).

[121] Y. Nanasaki, T. Hagiwara, H. Watanabe, and T. Sakiyama, Removability of bacterial spores made adherent to solid surfaces from suspension with and without drying, Food control **21**(11), 1472–1477 (2010).

[122] F. Bretherton, The motion of long bubbles in tubes, J. Fluid Mech **10**(2), 166–188 (1961).

[123] Z. Yao, *Geometries in Soft Matter*, PhD thesis, Syracuse University, 2012.

[124] O. Marin, *Boundary integral methods for Stokes flow: Quadrature techniques and fast Ewald methods*, PhD Dissertation, KTH Royal Institute of Technology, 2012.

[125] D. Duffy, *Green's functions with Applications*, Chapman & Hall/CRC Press, 2001.

[126] N. H. Abel, Solution de quelques problèmes à l'aide d'intégrales définies, Mag. Naturvidenskaberne **2**, 63–68 (1823).

[127] O. D. Kellogg, *Foundations of potential theory*, volume 31, Springer Science & Business Media, 2012.

[128] N. Günther, *La Theorie du Potentiel*, Gauthier-Villars, 1934.

[129] V. Agoshkov and P. Dubovski, Methods of potential theory, Computational Methods and Algorithms (2006).

[130] E. Miersemann, Linear Elliptic Equations of second Order, Lecture Notes - Department of Mathematics, Leipzig University , 7–43 (2012).

[131] I. Markina, Potential theory: the origin and applications.

[132] G. Green, *An essay on the application of mathematical analysis to the theories of electricity and magnetism*, author, 1828.

[133] M. Bonnet, Equations intégrales et éléments de frontiere, CNRS Editions/Eyrolles (1995).

[134] F. Obqvist, Uber die Randwertaufgaben der Hydrodynamik zaher Flussigkeiten, Math. Z **32**, 329–375 (1930).

BIOGRAPHICAL SKETCH

Ilyesse Bihi, was born in Rabat, the capital of Morocco. He was very fortunate to have an educated and caring family. His mother was an accountant for the Moroccan national railways company and his father was a bookseller.

He studied in the science faculty of Rabat were he learned the basics of physics and mathematics. Creating robots was one of his favorite hobbies. He even won the second prize in a robotic competition. To quench his thirst for discovery and knowledge, he decided to travel and study in France. Ilyesse attended Lille University, majoring fluid mechanics were he graduate valedictorian of his class.

Upon graduation, Ilyesse continued his education at Lille University in Micro-nanotechnology and University of Florida in chemical engineering. He was coadvised by Prof. Farzam Zoueshtiagh at Lille University and Prof. Jason E. Butler at University of Florida. He carried out numerical and experimental work in Microfluidics. For the biological applications, he also collaborated with Dr. Christine Faille from the National Institute for Agricultural Research. He received a dual PhD in these disciplines in 2016.

Décrochage de microparticules d'une surface grâce aux contraintes de cisaillement et aux forces interfaciales dans un écoulement diphasique.

RÉSUMÉ

Le décrochage de microparticules adhérant à une surface grâce aux écoulements se rencontre dans de multiples situations où le nettoyage minutieux ou sélectif de parois est crucial. Par exemple, l'industrie agroalimentaire rencontre des problèmes récurrents d'accrochage robuste de bactéries (microparticules) aux parois des lignes de production d'aliments comme le lait ou la viande. Dans cette thèse, l'utilisation d'un écoulement diphasique avec une interface fluide-fluide en complément d'un écoulement monophasique cisaillé a été considérée. L'interaction entre une interface liquide et une particule dépend principalement de l'énergie de surface totale. Elle correspond aux paramètres de mouillage et introduit une force supplémentaire qui peut contribuer à la force totale nécessaire pour le décrochement. Dans le cas d'un décrochement des microparticules et leur collecte par interface fluide-fluide, la stabilité de cette dernière se voit alors changer si sa surface n'est plus apte à acceuillir davantage de particules. D'autre part, la dynamique d'une particule ellipsoide, similaire à une spore, a été étudiée numériquement dans la seconde partie de cette thèse. L'étude a eu comme but de déterminer les conditions pour lesquelles une particule près d'une paroi peut s'y approcher ou s'en éloigner. Dans la dernière partie nous avons étudié l'influence des conditions initiales et en particulier le séchage sur les forces necéssaires pour le décrochement des spores.

Removal of microparticles from a surface due to interfacial and shear forces in two-phase flows

ABSTRACT

Food contamination due to pathogens and spoilage bacteria on surfaces of industrial equipment is a major issue that has not yet found a proper solution. Indeed, despite the set-up of cleaning and disinfection procedures, some bacteria (microparticles) are still commonly found on the surfaces of food processing lines. Traditionally, industrial cleaning procedures involve viscous stresses in a single-phase flow to remove spores from a surface. The present study investigates the use of two-phase flows for improving cleaning procedures. Such system has the advantage of involving interfacial forces that can aid in the removal of microparticles as long as certain wetting conditions are met. This would imply the detachment and collection of the microparticles by the fluid-fluid interface. This collection will in turn affect the dynamics of the interface if its surface is insufficient to accommodate all particles. With respect to viscous stresses in removing particles, a numerical code is developed to study the dynamics of ellipsoids near a solid surface in a shearing flow. The shape of the microparticles in the simulations is set to mimic the spores morphology. Finally, the study examines the effect of the initial environment on the ease of spores removal. In particular, the study investigates the drying conditions that spores undergo in an industrial environment before the cleaning procedures start.